Monte Carlo Calculation of the Pinch and Bootstrap Neoclassical Transport Coefficients

J.W. Johnson, L.M. Lidsky, K. Molvig and K. Hizanidis

MIT Plasma Fusion Center, Cambridge MA 02139

December 7, 1983

MONTE CARLO CALCULATION OF THE PINCH AND BOOTSTRAP
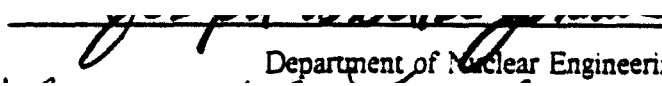## NEOCLASSICAL TRANSPORT COEFFICIENTS
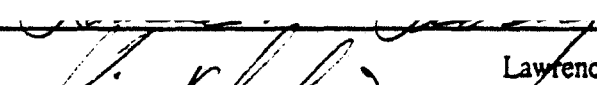
by

Joseph William Johnson

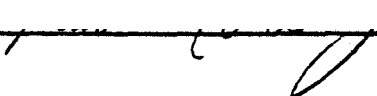B.S., University of Wisconsin–Madison
(May, 1979)

S.M., Massachusetts Institute of Technology
(June, 1981)

Submitted in Partial Fulfillment
of the Requirements for the Degree of
Doctor of Philosophy

at the

Massachusetts Institute of Technology
December, 1983

© Massachusetts Institute of Technology 1983

Signature of Author _____
Department of Nuclear Engineering, December 7, 1983

Certified by _____
Lawrence M. Lidsky, Thesis Supervisor

Certified by _____
Kim Molvig, Thesis Supervisor

Accepted by _____
A. F. Henry, Chairman, Departmental Committee on Graduate Students

Monte Carlo Calculation of the Pinch and Bootstrap
Neoclassical Transport Coefficients
by
Joseph William Johnson

Abstract

The properties of the pinch and bootstrap transport coefficients in axisymmetric systems are investigated using a computer code which integrates the particle guiding center equations. Simple models are developed for the magnetic field and electric field. Two dimensional cubic B-spline interpolation is used to compute the magnetic flux coordinate. Collisions are modeled by a Monte Carlo pitch angle scattering operator.

Comparisons to the Lagrangian formulation of neoclassical transport theory are made for both the explicit and the implicit transport coefficients. In the ideal banana regime theory, the explicit and implicit transport coefficients satisfy independent Onsager symmetry relationships. As the scattering frequency is increased, it is predicted that the explicit symmetry relationship should be broken, leaving the trapped particle pinch effect dominant. Also, the implicit processes, which are dominant in the ideal banana limit, should be largely destroyed as the collision frequency is increased.

For the trapped particle explicit pinch, it is found that the numerical results are in good agreement with the ideal theory. The predicted outward flow of the circulating particles does occur, however the circulating particle contribution does not cancel the trapped particle contribution to the predicted degree. This difference can be shown to be due to particles in a narrow region of phase space near the trapped–circulating boundary, which make the dominant contribution to the circulating particle pinch coefficient. These particles do not make the expected contribution to the circulating particle explicit pinch coefficient because of particular kinematic effects not included in the ideal theory.

The explicit pinch coefficient calculations were repeated for several collision frequencies. As predicted, the trapped particle pinch is found to be unaffected by a low level of collisions, while the circulating pinch coefficient is reduced because of the scattering effects on the particles near the boundary. The net result is an enhancement of the inward particle flux, which is the predicted result of the breaking of the Onsager symmetry relationship for the explicit processes.

Both the circulating and trapped particle explicit current coefficients were studied. The explicit currents are diamagnetic in nature. These transport coefficients were found to be in good agreement with the predictions of the ideal theory, and to be unaffected by low scattering levels.

The implicit processes were studied by computing the Fokker–Planck coefficient $\langle \frac{\Delta \mu \Delta \psi}{\Delta r} \rangle$ for several scattering frequencies. At the smallest frequency studied, $\langle \frac{\Delta \mu \Delta \psi}{\Delta r} \rangle$ is dominated by the marginally circulating particles, as predicted by the finite collisionality theory. As the collision frequency is increased, the marginally circulating particle contribution to $\langle \frac{\Delta \mu \Delta \psi}{\Delta r} \rangle$ decreases, leading to a decrease in both the implicit pinch and bootstrap transport coefficients.

Acknowledgements

"At first I resolved not to disturb you with such a useless piece of information," said he. "However, our impulses are too strong for our judgment sometimes."

— Thomas Hardy, *Tess of the d'Urbervilles*

"... I honestly think you ought to sit down calmly, take a stress pill and think things over... I've still got the greatest confidence in the mission..."

— Arthur C. Clarke, *2001: A Space Odyssey*

"We dwarfs and fools have no business dancing on concrete made for giants. If only we had stayed under the rostrums where no one suspected our presence!"

-- Gunter Grass, *The Tin Drum*

God moves in a mysterious way, and I just wish He wouldn't insist on carting me along with Him.

— Sir Harry Flashman

I would like to thank several people not only for making this thesis possible, but more importantly, for teaching me more than I ever expected to learn and making it more enjoyable than it needed to be.

Thanks to Prof. Lidsky for providing support and encouragement during this thesis. Thanks to Kyr Hizanidis for helping me with the theoretical calculations which appear in Chapter 3. Thanks also to Prof. Molvig for the many helpful suggestions.

Thanks to John Aspinall for teaching me about B-splines and helping me understand the mysteries of MacLisp. Thanks to Pete Roemer for instructing me in the joys of system software hacking. Thanks to Mark Tillack for our frequent discussions and for allowing me to snarf the first paragraph from *his* acknowledgements. A special thanks to John, Pete and Mark for being part of the FEMBOT project.

Finally, thanks to MIT, particularly the computations group at the Plasma Fusion Center, for encouraging self-reliance.

Contents

List of Figures

List of Tables

Introduction

One of the important concerns in magnetic confinement fusion devices is the transport of particles, energy and charge. In this work we shall consider the conjugate processes of the pinch effect and the bootstrap current. Neoclassical transport theory has predicted[1] the existence of the bootstrap current, driven by a radial density gradient and the pinch effect driven by the toroidal electric field. Both of the these processes are of substantial practical interest. Experimentally, the pinch effect has been observed[2,3], but there is strong evidence that the bootstrap current does not exist[4,5]. This is surprising because the two processes are Onsager conjugates.

Recently, a Lagrangian formulation of neoclassical transport theory has been developed[6—8]. In the Lagrangian formulation, the transport coefficients can be expressed as the sum of two types of processes, termed explicit and implicit. The explicit processes are fluxes which do not involve deviations of the particle distribution function from a local Maxwellian. An example of an explicit kinematic process is the trapped particle pinch effect, as described by Ware[9]. Examples of explicit scattering processes are the Fokker–Planck coefficients $\langle\frac{\Delta\mu\Delta\mu}{\Delta r}\rangle$ and $\frac{\Delta\psi\Delta\psi}{\Delta r}$. Implicit processes involve the perturbed distribution function and are inherently collisional in nature. The predicted bootstrap current is an implicit process. In the conventional, Eulerian formulation of neoclassical transport theory, no distinction is made between the explicit and implicit processes. The pinch effect is identified with the Ware effect, but the question of why a kinematic flow of trapped particles should be Onsager symmetric to a collisional flux of the circulating particles has never been adequately explained.

In the Lagrangian formulation, the explicit and implicit transport coefficients have separate Onsager symmetry theorems. The conjugate process to the implicit bootstrap current is an implicit pinch effect. The conjugate process to the explicit pinch effect is an explicit current. This current, which is essentially diamagnetic in nature, can be shown to be of $O(\epsilon^{\frac{3}{2}})$. The pinch transport coefficient must also be of $O(\epsilon^{\frac{3}{2}})$ if the explicit transport matrix is to be Onsager symmetric. The Ware effect leads to a transport coefficient of $O(\epsilon^{\frac{1}{2}})$, but the ideal theory in the banana regime

predicts that an outward flow of the circulating particles will cancel the inward directed Ware effect to leading order.

The nonobservance of the bootstrap current can be explained using the Lagrangian formulation. The dominant contribution to the implicit processes comes from a narrow region in phase space near the trapped–circulating boundary. This same portion of phase space, henceforth called the boundary layer, also provides the dominant contribution to the explicit circulating particle pinch and bootstrap coefficients. Low scattering levels will have a large effect on the kinematics of the boundary layer particles, yet will leave the trapped particle orbits relatively intact. Thus the implicit pinch effect and the implicit bootstrap current, which depend strongly on the boundary layer particles, will be destroyed. The explicit circulating particle pinch coefficient will also be reduced because the boundary layer particles make the largest contribution to this coefficient. The explicit trapped particle pinch and current coefficients will be unaffected by the low collisionality. Thus the net effect of the collisions is to destroy the bootstrap current and reduce the circulating particle explicit pinch coefficient, leaving the Ware effect as the dominant contribution to the pinch effect. Thus the symmetry relationship for the explicit pinch and explicit bootstrap current will be broken.

We will be studying both the ideal banana theory and the finite collisionality theory, which are derived from the Lagrangian formulation of neoclassical transport theory. In the ideal banana regime theory, limit of zero collisionality, $\nu_* \rightarrow 0$ is taken, although the collision frequency, ν, may be finite. In the finite collisionality theory ν_* is not restricted to zero.

In this thesis, the pinch and bootstrap transport coefficients, both explicit and implicit, will be investigated by numerical simulation of the the particle orbits. Scattering will be simulated by a Monte Carlo scattering operator. In the next chapter, issues pertinent to the methodology used in the numerical simulation, e.g. how the statistical averaging is done for the Monte Carlo calculations and the initial particle distribution, will be examined. In Chapter 3, the predictions of the Lagrangian formulation for the Lorentz model will be discussed. Both the ideal banana theory ($\nu_* \rightarrow 0$) and the finite collisionality theory will be examined. A physical picture of the processes involved will be presented, and expressions which can be evaluated for comparison to the data obtained from the simulation will be derived. Details of the models used for the magnetic field, density and scattering, as well as the method used to calculate the toroidal flux coordinate and other components of the numerical simulation are presented in Chapter 4. The results from the simulation are given in Chapter 5, and comparisons to the expressions derived from the theories presented in Chapter 3 are made. A summary of the results and conclusions are given in Chapter 6.

Methodology

Given the problem of computing transport coefficients by numerical simulation of particle orbits, many issues remain which are not specified completely by the desire to compare the numerical results to those predicted by theory. For example, the Lagrangian formulation (see Chapter 3) demands little about the structure of the magnetic field except that it be axisymmetric. The choice of a magnetic field model, or any of the physical processes which will be a part of the simulation, will depend on many factors, including compatibility with theory, ease of numerical evaluation and numerical accuracy. In this chapter, we will present a discussion of the methodology used in the transport coefficient calculation.

Section 2.1 is devoted to notational issues. Here many variables and parameters which will be used in succeeding chapters will be defined. The next two sections deal with the choice of magnetic field, electric field and scattering models. In Section 2.4, the method of calculating the transport coefficients is outlined. The final two sections deal with the questions of the initial distribution of the particles and the averaging method used with the scattering model. Discussion of specific computational details of the models which were chosen will be delayed until Chapter 4.

2.1. Nomenclature

$\underline{B}$ magnetic field. The magnitude of the magnetic field is expressed as $|\underline{B}|$ or sometimes B. The toroidal field value at the major axis (R_0) is denoted B_0.

$\underline{E}$ electric field. The only non-zero component of $\underline{E}$ in this work is E_ϕ.

ϵ inverse aspect ratio.

$\underline{v}$ particle velocity. The magnitude of $\underline{v}$ is expressed as v.

H particle energy. $H = \frac{1}{2}mv^2$ where m is the particle mass.

$\cos\eta$ cosine of the pitch angle. The ratio of the particle velocity component parallel to the field line to the magnitude of the velocity.

σ sign of the parallel velocity component. $\sigma = +1$ refers to forward directed particles, $\sigma = -1$ refers to backward directed particles.

μ magnetic moment. $\mu = \cos^2 \eta H/|\underline{B}|$.

λ global pitch parameter. $\lambda = B_0\mu/H$ circulating particles are in the region $0 \leq \lambda \leq 1-\epsilon$, trapped particles are in the region $1 - \epsilon \leq \lambda \leq 1 + \epsilon$.

ω_b poloidal bounce frequency. For a given particle ω_b is the reciprocal of the amount of time need to complete one poloidal orbit with $E_\phi = 0$ and $\nu_* = 0$.

ω_{b0} ω_b of the $\lambda = 0$ particles.

ω_2 poloidal frequency. Similar to ω_b except that the restriction $\nu_* = 0$ is dropped.

ψ toroidal flux.

$\overline{\psi}$ bounce (poloidally) averaged toroidal flux.

$\frac{\Delta\psi}{\Delta r}$ "radial velocity". The average rate of change of the flux coordinate during one poloidal orbit.

$\langle\frac{\Delta\psi}{\Delta r}\rangle$ statistically averaged radial velocity.

ν collision frequency. Defined as the deflection collision frequency in reference 16. The defining equation is given in subsection 4.2.1.

ν_* collisionality parameter. $\nu_* = \nu/\omega_{b0}(2\epsilon)^{\frac{3}{2}}$

$T_{13,e}$ explicit pinch transport coefficient. The implicit pinch transport coefficient, $T_{13,i}$, will not be computed.

$T_{31,e}$ explicit bootstrap transport coefficient.

2.2. Choice of Magnetic Field Model

For a numerical simulation of this type, there are two general types of magnetic fields which are used; the first is a "model" field, where the magnetic field is given by a relatively simple analytic expression, the second type is a "real" field, where the field can be considered to be the superposition of the fields from (possibly filamentary) conductors. The advantage of the analytic model field is that it is simple to evaluate the magnetic field at an arbitrary point. The disadvantages are that it may not be divergence free, there could be computational problems in evaluating the toroidal or poloidal flux. The advantage to using a realistic field is that the curl and divergence properties of the field will be exact, at least to machine precision. However, evaluating the field at an arbitrary point can be very costly numerically, and computation of the flux can be very complicated.

We have chosen a magnetic field model which combines the advantages of both approaches and minimizes the disadvantages. Our model consists of three elements: a $1/R$ toroidal field, a poloidal field from a dipole, and a constant vertical field. The vertical field is adjusted to provide a magnetic well (see Section 4.1). The advantages to this type of model are: the field is exactly curl free, and divergence free to machine precision; the field can be evaluated at an arbitrary point very easily; and the magnetic axis is known to be at the dipole radius.

The disadvantage is that computing ψ requires computation of the line integral of the vector potential along the toroidal projection ($\phi = 0$) of a field line. This can be a very costly process, but use of two-dimensional cubic B-spline interpolation (see Section 4.3) simplifies the process considerably. Instead of integrating the vector potential at each point, the integration is done for a rectangular grid of points. This has to be done only once, after which ψ can be computed from the grid values with very little cost. Use of a fast and accurate interpolation scheme to compute ψ makes it possible to compute $\overline{\psi}$ and the kinematic bootstrap current; each of these calculations involves thousands of ψ evaluations.

One further difficulty with the use of the realistic magnetic field model is apparent when comparing the numerical results with those predicted by theory. The theory assumes that ϵ does not vary with poloidal angle, i.e. the flux surfaces are circular. In general, a "real", toroidal system will not have circular flux surfaces. Such is the case with our model; ϵ varies by $\sim 1\%$ for a representative flux surface. This variation will have have an effect on the particle orbits which will be examined in Chapter 5. The value of ϵ used in the calculations is determined from the value of λ on the trapped-circulating boundary. This λ value is easily computed, applying the definition we have $\lambda = B/B_0$. The inverse aspect ratio becomes $1 - B/B_0$, this corresponds to ϵ at the inside of the torus.

2.3. Choice of Electric Field and Scattering Models

The ideal banana theory postulates a constant toroidal electric field. In the theory, the limit of infinitesimal E_ϕ is taken. In a numerical simulation, we must use a finite value of E_ϕ if we are to recover any electric field related particle motion. If we make the field too small, we will have two problems: the change in ψ due to the electric field will become the same size as the error in the interpolated value of ψ, and the statistical errors in the collisional calculations will be larger than the values of the quantities of interest (see below Section 2.5). If we make the field too large, backwards directed circulating particles will be swept into trapped space (see Section 2.4). An intermediate value of 0.05 V/m was chosen.

We considered two different scattering models, pitch angle scattering at constant energy and energy scattering at constant μ (see Section 4.2 for details). The purpose of the scattering in this

problem is to introduce an element of randomness which will modify the particle orbits. The scattering is what distinguishes the ideal banana theory ($\nu_* \to 0$) from the finite ν_* theory. While both models were used for qualitative verification of the predicted results, for the quantitative, Monte Carlo transport coefficient calculation the pitch angle scattering model was chosen. In this way we were able to exploit the energy dependence of the transport integrals (see Section 2.5 and Chapter 3).

2.4. Calculation of the Radial Velocity

The radial velocity $\frac{\Delta \psi}{\Delta \tau}$ will be an important quantity in the computation of both the explicit pinch coefficient and the Fokker–Planck coefficient $\langle \frac{\Delta \mu \Delta \psi}{\Delta \tau} \rangle$. To obtain the explicit pinch coefficient $T_{13,e}$, $\frac{\Delta \psi}{\Delta \tau}$ must be integrated over phase space; the phase space distribution of particles used in the calculation will be discussed in the next section. Computing the Fokker–Planck coefficient requires that $\frac{\Delta \psi}{\Delta \tau}$ be multiplied by the change in the magnetic moment and statistically averaged.

Computing $\frac{\Delta \psi}{\Delta \tau}$ from a particle orbit is a relatively straightforward process. The particle is followed for a time $\Delta \tau$, and then the difference between final and initial flux values, $\Delta \psi$, is computed. There are two possible problems with this simple calculation. First, the particle drift surface will in general not coincide with the flux surface. Thus there will be a periodic variation (with respect to θ) in $\Delta \psi$ which should be averaged out of the $\frac{\Delta \psi}{\Delta \tau}$ calculation. Second, as will be discussed in Section 2.5, $\frac{\Delta \psi}{\Delta \tau}$ is extremely sensitive to electric field induced drifts in λ.

Both of these difficulties can be overcome by following the particle for some number of poloidal orbits. Because the particle returns to the same θ value, no correction (to first order) for the periodic variation of $\Delta \psi$ is necessary. The reason that one poloidal orbital period is chosen for $\Delta \tau$ is to minimize the drift motion in λ space. One further advantage to this choice of $\Delta \tau$ is that the poloidal bounce frequency is just $\frac{1}{\Delta \tau}$. This is precisely the weighting factor needed calculation of the transport coefficients.

2.5. Initial Particle Distribution

In this section, the distribution from which the particles are launched will be discussed. Given a starting flux surface, these three parameters uniquely determine the particle's location in phase space: the cosine of the pitch angle, the poloidal angle and the energy.

The global pitch parameter, λ, can be computed from the values of ψ, $\cos \eta$ and θ. σ is just the sign of $\cos \eta$. In Chapter 3, we will show that the energy dependence of the quantities of interest, e.g. $\frac{\Delta \psi}{\Delta \tau}$, is the same for both trapped and circulating particles. So while ω_b, $\frac{\Delta \psi}{\Delta \tau}$ and the transport coefficients will all depend on the value of the particle energy, we can still compare the results from a single energy to the ideal theory because the ratio of the circulating particle

explicit pinch coefficient to the trapped particle explicit pinch coefficient should be independent of the particle energy. Use of only a single energy will reduce the amount of computation needed to do the Monte Carlo calculations to a "reasonable" level. The energy value used in both the ideal and finite ν_* calculations is $H = 2.0$ keV; the ideal calculations were repeated for $H = 1.0$ keV and $H = 4.0$ keV to check the validity of the "single energy" distribution result. It is found that the ratio of the circulating to trapped particle explicit pinch coefficients is constant to within 10%.

The values of $\cos\eta$ used are widely separated for the trapped and well circulating particles. The spacing of the $\cos\eta$ values is reduced for the boundary layer particles to permit resolution of the predicted boundary layer features.

There is a slight complication in this picture of the $\cos\eta$ distribution. In both the ideal banana theory and the finite ν_* theory, the limit $E_\phi \to 0$ is taken. This coupled with the use of the bounce averaged flux, implies that there should be no difference between the forward directed and backward directed particles. For the reasons discussed in the Section 2.3, a value of E_ϕ was chosen that is small compared to values in current tokamak experiments, but definitely not zero. This will cause the dynamics of the boundary layer to become extremely dependent on σ. The electric field will cause the $\sigma = +1$ particles to accelerate, the $\sigma = -1$ particles to decelerate. Because of the acceleration/deceleration, the energy of the particle increases/decreases. If we consider the $\nu_* = 0$ case, we have μ as a constant of the motion, thus a change in energy causes a drift in λ. As the $\sigma = +1$ particles accelerate, their energy increases, causing a decrease in λ, i.e. the particle tends to become well circulating. Similarly, a $\sigma = -1$ particle tends to drift toward trapped space.

There are two important results of this effect which influence the choice of the initial λ values of the particles. The effect of the drift in λ is that the forward particles have a bounce averaged value of λ which is smaller than the initial λ value, while the backward particles have a larger bounce averaged λ. The result is the forward particles have a smaller value of $\frac{\Delta\psi}{\Delta r}$ for example, than the backward particles at the same initial value of λ. In the ideal banana theory, the limit of $E_\phi \to 0$ is taken. Thus there are no drifts in λ, and the "splitting" of the $\sigma = \pm 1$ particles does not happen. In order to observe any electric field induced effects, we must use a finite value for E_ϕ. This will cause the splitting effect, so we have to follow both $\sigma = \pm 1$ particles to compute the transport coefficient; we can not simply multiply the forward particle contribution by two to get the complete transport coefficient. It is found that the splitting of forward and backward particles increases as E_ϕ is increased. This is expected because the change in λ is inversely proportional to the change in H caused by the electric field.

The second result of the non-zero electric field is an extreme case of the λ drift problem. For a given value of E_ϕ, the change in λ will be large enough that some $\sigma = -1$ particles will actually cross the trapped–circulating boundary. The width in λ of the band of particles which undergo this transition is proportional to E_ϕ. Because the transition is not included in either

the ideal banana or the finite collisionality theory, these particles should not be included in the integration over phase space. Instead, an extrapolation is made from the last $\sigma = -1$ particle that does not cross the boundary, to the $\sigma = +1$ particle at the boundary. This extrapolation is made for comparison to the results predicted by the ideal theory. The extrapolated region accounts for 35% of the circulating particle explicit pinch coefficient in the $\nu_* = 0$ case, this fraction decreases as ν_* increases.

The remaining parameter is θ, or stated another way, how is the value of $\frac{\Delta \psi}{\Delta r}$ to be poloidally averaged? One point to bear in mind is that the drift surface of the boundary layer particles is not just shifted by the action of E_ϕ, the drift surface is actually stretched towards the inside of the torus. In order to reduce the amount of computation needed, and to recover the $\frac{\Delta \psi}{\Delta r}$ produced by the stretching of the drift surface, it was suggested that particles be launched from the same bounce averaged drift surface. Thus only two values of θ would have to be considered; $\theta = \pi$ on the inside of the torus for the circulating particles, and $\theta = 0$ on the outside, for the trapped particle calculation. The poloidal averaging would already be accomplished by utilizing the bounce averaged drift surface.

Unfortunately, this is not feasible. The problem is that the particles are no longer well ordered with respect to λ. Launching from the same $\overline{\psi}$ surface implies that the local value of ψ will not be the same for particles with different values of $\cos \eta$. The variation in ψ yields a different major radius for the particles and the $1/R$ dependence of $|\underline{B}|$ produces a variation in λ. For example, consider two particles with the same $|\cos \eta|$, but opposite values of σ. If we launch them from the same $\overline{\psi}$ surface, the initial ψ value of the $\sigma = +1$ particle must be less than the initial flux value of the $\sigma = -1$ particle. This leads to a non-negligible difference in λ.

The problem becomes acute when we consider the location of the boundary. The trapped–circulating boundary is defined by the λ value of the $\theta = \pi$, $\cos \eta = 0$ particle. As this particle is barely circulating, only trapped particles should lie on the right side of the boundary. If particle are launched from the same ψ surface, this is the case; however, if the particles are launched from the same $\overline{\psi}$ surface, there will be circulating particles on the right (trapped) side of the boundary. It is observed that the variation in $\frac{\Delta \psi}{\Delta r}$ between particles with the same value of $\cos \eta$ but on the bounce averaged ψ surface and the local ψ surface, is small, approximately 10% for the boundary layer particles, less for the well circulating and trapped particles. So it was decided to launch the particles from the two values of θ as described above, but to launch from the same ψ surface, not the same $\overline{\psi}$ surface.

To summarize: particles are launched from the same ψ surface with the same energy. The particles have a uniform spacing in $\cos \eta$ in the well circulating and trapped regions, but have a smaller spacing near the trapped–circulating boundary. Both the $\sigma = \pm 1$ particles are launched

from the value of λ determined by $\cos\eta$ unless the $\sigma = -1$ is in the transition region near the boundary. The same initial distribution is used for both the finite and infinitesimal ν_* cases.

2.6. Statistical Averaging

In this section, the methods used to compute quantities like $\langle\frac{\Delta\psi}{\Delta r}\rangle$ and $\langle\frac{\Delta\mu\Delta\psi}{\Delta r}\rangle$ will be discussed. Also, the means of obtaining an estimate of the statistical error in the Monte Carlo calculations will be presented.

The scattering model consists of pitch angle scattering at constant energy; because the scattering process changes $\cos\eta$, it can be considered as scattering in λ. The change in λ inherent in the scattering process presents a difficulty: some of the boundary layer particles will scatter into trapped space and will not complete the one poloidal orbit necessary to compute $\frac{\Delta\psi}{\Delta r}$ and the other quantities of interest. This problem is ameliorated by following these particles for approximately twenty bounce periods. In this time, the boundary layer particles have time to scatter across the boundary several times, and one poloidal orbit can be completed. However, 5 to 10% of the boundary layer particles (the number depends on ν_* and E_ϕ) become deeply trapped. These are not included in the statistical averaging; the possible error in neglecting these particles is approximately 10%.

As an example, consider the calculation of $\langle\frac{\Delta\psi}{\Delta r}\rangle$. A large number of particles are launched from the same point in phase space, $\frac{\Delta\psi}{\Delta r}$ is computed for each particle unless it does not complete one poloidal orbit as described above. $\langle\frac{\Delta\psi}{\Delta r}\rangle$ is defined as the arithmetic mean of the values of $\frac{\Delta\psi}{\Delta r}$. The statistical error is computed from the variance[10]:

$$\sigma^2 = \frac{1}{n(n-1)}\sum_{i=1}^{n}(x_i - \bar{x})^2 \tag{2.6.1}$$

where n is the number of data points, x_i and $\bar{x}$ are the data and the mean of the data, respectively. The estimated error is the square root of the variance. Consideration of the estimated error determines the number of particles which must be launched from each location on the phase space grid; the error was also the limiting criterion on the value of E_ϕ chosen. In the calculation of the kinematic pinch transport coefficient, the actual value of $\frac{\Delta\psi}{\Delta r}$ will be proportional to E_ϕ. Because the scattering mechanism is independent of E_ϕ, the estimated statistical error will be approximately constant as E_ϕ is varied. To minimize the relative statistical error, or to keep n as small as possible for a given level of relative statistical error, E_ϕ should be increased. Thus the estimated error is a smaller fraction of the mean value, because the mean is increasing, while the error is not. If too small a value of E_ϕ is used, the number of points will have to be increased drastically to improve the relative error. It was found that a value of $E_\phi = 0.05$ V/m produced acceptable statistical

errors. For $\nu_* = 2.0 \times 10^{-4}$ the number of points needed to keep the relative error below 10% for the boundary layer particles was ~ 1500.

An additional complication occurs in the computation of the kinematic pinch transport coefficients, which does not occur in the Fokker–Planck coefficient calculation or the kinematic bootstrap current calculation. In the latter two calculations, the electric field is set to zero, in the case of the Fokker–Planck coefficients because they are due to scattering "cross processes", for the bootstrap current because the driving force is the density gradient. It turns out that if E_ϕ is set to zero during the Monte Carlo calculation of $\langle \frac{\Delta \psi}{\Delta \tau} \rangle$, a non-zero transport coefficient is found. This can readily be explained in terms of relationship between the Fokker–Planck coefficients and the drag coefficient. Recall that:

$$\langle \frac{\Delta \underline{v}}{\Delta \tau} \rangle = \langle \frac{\Delta \underline{v}}{\Delta \tau} \rangle_{drag} + \frac{\partial}{\partial \underline{v}} \cdot \langle \frac{\Delta \underline{v} \, \Delta \underline{v}}{\Delta \tau} \rangle \tag{2.6.2}$$

where $\Delta \underline{v}$ is a jump in phase space and the angle brackets refer to the statistical average. Without an electric field, one would expect that the two terms on the right hand side should exactly cancel (assuming a steady state distribution function). However, we have restricted the scattering operator to pitch angle scattering — no energy scattering is allowed. Without energy scattering, the terms on the right hand side will not cancel and we will obtain a non-zero $\langle \frac{\Delta \psi}{\Delta \tau} \rangle$. Because we are interested in the part of $\langle \frac{\Delta \psi}{\Delta \tau} \rangle$ which is driven by the electric field, for each location on the phase space grid two complete sets of data must be taken; one with and one without the electric field. The $E_\phi = 0$ data are then subtracted out to give $\langle \frac{\Delta \psi}{\Delta \tau} \rangle$.

The Lagrangian Formulation

In this chapter, a broad overview of the Lagrangian formulation of neoclassical transport theory will be presented. For a more complete discussion of the Lagrangian formulation see references 6, 7 and 8. Special emphasis will be placed on the two processes of interest, the pinch effect and the bootstrap current. The physical mechanisms for the two processes will be presented, along with expressions which will enable the transport coefficients and other quantities of interest to be computed. Comparison of these expressions with the numerical results will be made in Chapter 5.

The Lagrangian formulation of neoclassical theory is constructed from three actions: the magnetic moment, the parallel invariant and the bounce averaged poloidal flux. By averaging over the fast orbital time scales an equation of the Fokker–Planck type which involves the actions alone is obtained. This action space representation of the kinetic equation contains two types of processes, termed explicit and implicit. The explicit processes are processes which do not involve deviations from a local Maxwellian, for example the Ware pinch or the explicit scattering processes mentioned in Chapter 1. The implicit processes are due to perturbations of the distribution function.

The decomposition of the fluxes into explicit and implicit contributions is an important feature of the Lagrangian formulation. These contributions have separate Onsager symmetry theorems for their respective transport matrices. The conventional Eulerian theory does not make the distinction between implicit and explicit processes. In the Eulerian theory the pinch effect has been interpreted as the (explicit) Ware effect due to the trapped particles. Its conjugate process, the bootstrap current is a collisional (implicit) process due to the circulating particles. Why two such fundamentally different processes should obey an Onsager symmetry relationship has never been satisfactorily explained within the Eulerian framework.

It has been suggested[6−8] that the Onsager symmetry relationship would be broken by the inclusion of turbulence or scattering effects. In this Chapter both the theory in the ideal banana regime ($\nu_* \to 0$, ν finite) and the finite ν_* theory will be summarized.

In the Lagrangian formulation, the explicit pinch transport coefficient is a result of the Ware inward directed flux of trapped particles, reduced by a competing outward flow of particles from a narrow region in λ space near the trapped–circulating boundary. The conjugate process is the kinematic bootstrap current or banana current, which is essentially diamagnetic in nature. The cancellation of the trapped and circulating explicit pinch coefficients results in a small net pinch coefficient which is symmetric to the explicit current coefficient. The conjugate process of the implicit bootstrap current is a collisional pinch effect which is dominated by the contribution of the circulating particles in the boundary layer.

The addition of finite ν_* to the problem will produce major changes in the transport coefficients. Scattering will disrupt the correlations which give rise to the implicit processes. Also, scattering will "smear out" the boundary layer, which will reduce the cancellation of the Ware effect by the circulating particle explicit pinch. The result is that collisions will leave the explicit trapped particle pinch coefficient intact, but reduce the bootstrap current, the collisional pinch and the explicit circulating pinch coefficient. Thus the Onsager symmetry relationship of the explicit transport matrix is broken.

3.1. Particle Kinematics and the Explicit Pinch Coefficient

In this section, the expressions derived from the application of the ideal theory to the Lorentz model for the (poloidal) bounce frequency, the rate of change of the particle's flux coordinate and the explicit pinch transport coefficient will be presented. These expressions will not be derived (see references 6, 7 and 8 for the derivation), but they will be manipulated into a convenient form for comparison to the results of the numerical simulation, which will be given in Chapter 5. In addition, a simple physical mechanism of the explicit particle fluxes will be presented.

In calculating the pinch transport coefficients $T_{13,e}$, $\frac{\Delta\psi}{\Delta\tau}$ must be integrated over the velocity-like actions (denoted $\mathcal{I}_\perp$), μ and the parallel invariant. It is possible to make a change of variables from the actions $\mathcal{I}_\perp$ to the pitch parameter λ and the energy H. This leads to the relationship:[8]

$$d^2\mathcal{I}_\perp = \omega_b^{-1} H\, dH\, d\lambda \qquad (3.1.1)$$

where a multiplicative constant has been neglected. One of the goals of this section is to show that the energy dependence of ω_b and $\frac{\Delta\psi}{\Delta\tau}$ is the same for both trapped and circulating particles. This is to justify the use of a single energy in the numerical simulation, instead of a distribution of particle energies (see Section 2.5). If the energy dependence can be neglected the pinch transport coefficient can be computed by integrating $\frac{\Delta\psi}{\Delta\tau}$ weighted by ω_b^{-1} over λ.

First, expressions for ω_b for both trapped and circulating particles will be needed. These are:[8]

$$\omega_b^{trap} = \frac{1}{2}\sqrt{\frac{2H}{m}}\sqrt{1+\epsilon-\lambda}\frac{k}{K(\frac{1}{k})} \tag{3.1.2}$$

$$\omega_b^{circ} = \sqrt{\frac{2H}{m}}\sqrt{1+\epsilon-\lambda}\frac{1}{K(k)} \tag{3.1.3}$$

where K is the complete elliptic integral of the first kind, m is the mass of the particle and

$$k^2 = \frac{2\epsilon}{1+\epsilon-\lambda} \tag{3.1.4}$$

Again, common multiplicative factors have been neglected. Notice that the expressions for ω_b have the same energy dependence and that at the trapped–circulating boundary ($\lambda = 1-\epsilon$) ω_b goes to zero. The equation for ω_b^{trap} can be simplified using the definition of k.

$$\omega_b^{trap} = \frac{1}{2}\sqrt{\frac{2H}{m}}\frac{\sqrt{2\epsilon}}{K(\frac{1}{k})} \tag{3.1.5}$$

To simplify the expression of $\frac{\Delta\psi}{\Delta\tau}$ and the integration to obtain the transport coefficients, the function $S_{13,e}(\lambda)$ is introduced.

$$S_{13,e}(\lambda)^{trap} = \frac{1}{\pi}\sqrt{\frac{2}{\epsilon}}K(\frac{1}{k}) \tag{3.1.6}$$

$$S_{13,e}(\lambda)^{circ} = \frac{2}{\pi}\frac{K(k)}{(1+\epsilon-\lambda)^{\frac{1}{2}}} - \frac{\pi}{2}\frac{1+\epsilon-\lambda}{K^2(k)}\left[2\lambda\frac{\partial}{\partial\lambda}\frac{K(k)}{(1+\epsilon-\lambda)^{\frac{1}{2}}} + \frac{K(k)}{(1+\epsilon-\lambda)^{\frac{1}{2}}}\right] \tag{3.1.7}$$

Carrying out the differentiation with respect to λ we have:

$$S_{13,e}(\lambda)^{circ} = \frac{2}{\pi}\frac{K(k)}{(1+\epsilon-\lambda)^{\frac{1}{2}}} - \frac{\pi}{2}\frac{\sqrt{1+\epsilon-\lambda}}{K(k)}\left[1 + \frac{\lambda}{1-\epsilon-\lambda}\frac{E(k)}{K(k)}\right] \tag{3.1.8}$$

where E is the complete elliptic integral of the second kind. The expressions for $\frac{\Delta\psi}{\Delta\tau}$ are given in terms of $S_{13,e}(\lambda)$[8]

$$\frac{\Delta\psi}{\Delta\tau}^{trap} = 2\omega_b^{trap}\left(\frac{2H}{m}\right)^{-\frac{1}{2}}S_{13,e}(\lambda)^{trap} \tag{3.1.9}$$

$$\frac{\Delta\psi}{\Delta\tau}^{circ} = \omega_b^{circ}\left(\frac{2H}{m}\right)^{-\frac{1}{2}}S_{13,e}(\lambda)^{circ} \tag{3.1.10}$$

where a multiplicative constant has been neglected. Notice that the energy dependence of $\frac{\Delta\psi}{\Delta\tau}^{trap}$ is the same as $\frac{\Delta\psi}{\Delta\tau}^{circ}$. Multiplying out the ω_b term, and eliminating the common energy dependence, we have:

$$\frac{\Delta\psi}{\Delta\tau}^{trap} = 1 \tag{3.1.11}$$

$$\frac{\Delta\psi}{\Delta\tau}^{circ} = 1 - \left(\frac{\pi}{2}\right)^2 \frac{1+\epsilon-\lambda}{K^2(k)}\left[1 + \frac{\lambda}{1-\epsilon-\lambda}\frac{E(k)}{K(k)}\right] \tag{3.1.12}$$

There are several features of these expressions for $\frac{\Delta\psi}{\Delta\tau}$ which should be noted. First, the circulating particle expression is singular at $\lambda = 1 - \epsilon$, i.e. the trapped circulating boundary. In the boundary layer region, it is easy to see that $\frac{\Delta\psi}{\Delta\tau}$ for the circulating particles have the opposite sign from the trapped particles. Thus when the final integration is done to obtain the transport coefficient, the circulating particle coefficient will tend to cancel the trapped coefficient.

Another interesting point is that $\frac{\Delta\psi}{\Delta\tau}^{circ}$ and change sign as λ nears zero (the well circulating part of phase space). If we interpret $\frac{\Delta\psi}{\Delta\tau}^{trap}$ to be an inward directed flow of trapped particles, then we have the well circulating particles also moving inward, while the particles near the boundary move outward.

If we consider the discussion of the trapped particle pinch in reference 9, we see that the result quoted above for $\frac{\Delta\psi}{\Delta\tau}^{trap}$ is consistent with the Ware effect. The expression for the trapped particle velocity is:[9]

$$\frac{dr}{dt} = -\frac{E_\phi}{B_{pol}} \tag{3.1.13}$$

where r is the minor radius and B_{pol} is the magnitude of the poloidal magnetic field. For a given value of E_ϕ and a given starting value of r which fixes B_{pol}, $\frac{dr}{dt}$ should be constant for all trapped particles, without regard to λ. There is an implicit assumption made here about the nature of the magnetic field. It is assumed that B_{pol} is a constant along the particle orbit, such will not be the case in practice. The above expression should be considered to be correct in the limit of a zero banana width or equivalently, the limit of $\epsilon = 0$.

All that remains is to integrate $\frac{\Delta\psi}{\Delta\tau}$ over $d^2J_\perp$. Leaving out common multiplicative factors, T_{13}^{trap} and T_{13}^{circ} can be written as:[8]

$$T_{13,\epsilon}^{trap} = 2nT\int_0^\infty d\left(\frac{H}{T}\right)\sqrt{\frac{H}{T}}\exp\left(-\frac{H}{T}\right)\int_{1-\epsilon}^{1+\epsilon} S_{13,\epsilon}(\lambda)^{trap}\,d\lambda \tag{3.1.14}$$

$$T_{13,\epsilon}^{circ} = nT\sum_\sigma\int_0^\infty d\left(\frac{H}{T}\right)\sqrt{\frac{H}{T}}\exp\left(-\frac{H}{T}\right)\int_0^{1-\epsilon} S_{13,\epsilon}(\lambda)^{circ}\,d\lambda \tag{3.1.15}$$

where T is the plasma temperature, n is the plasma density and $\sum_\sigma$ is a sum over the forward and backward directed particles. This sum introduces a factor of 2 into the circulating integral[8], as the integrand is independent of the sign of the particle's parallel velocity component. Thus the effects of a finite E_ϕ on the particle orbits have been neglected. Again, the energy dependence of the integrand is the same for both circulating and trapped particles. The energy integration can be done, and the results[8] are:

$$T_{13,e}^{trap} = \frac{3}{4} n T I_{13,e}^{trap} \tag{3.1.16}$$

$$T_{13,e}^{circ} = \frac{3}{4} n T I_{13,e}^{circ} \tag{3.1.17}$$

·where:

$$I_{13,e}^{trap} = \frac{2}{3} \int_{1-\epsilon}^{1+\epsilon} S_{13,e}(\lambda)^{trap} \, d\lambda \tag{3.1.18}$$

$$I_{13,e}^{circ} = \frac{2}{3} \int_0^{1-\epsilon} S_{13,e}(\lambda)^{circ} \, d\lambda \tag{3.1.19}$$

All that remains to be done is to integrate $S_{13,e}(\lambda)$. These integrals can be performed in part using tables of elliptic integration formulae such as those found in reference 11. We first consider the trapped particle integral; changing the independent variable from λ to $k' = 1/k$, and substituting in for $S_{13,e}(\lambda)$:

$$\begin{aligned}
I_{13}^{trap} &= \frac{2}{3\pi} \sqrt{\frac{2}{\epsilon}} \int_1^0 k' K(k')(-4\epsilon) \, dk' \\
&= \frac{8\sqrt{2\epsilon}}{3\pi} \int_0^1 k' K(k') \, dk' \tag{3.1.20} \\
&= \frac{8\sqrt{2\epsilon}}{3\pi}
\end{aligned}$$

The circulating particle integral is a good deal more complicated. It will have to be broken up into smaller pieces which will be integrated separately. If we consider just the first term of equation 3.1.8:

$$P1 = \frac{2}{3} \int_0^{1-\epsilon} \frac{2}{\pi} \frac{K(k)}{\sqrt{1+\epsilon-\lambda}} \, d\lambda \tag{3.1.21}$$

Switching the variable of integration to k, we have:

$$P1 = \frac{4}{3\pi} \int_\beta^1 \frac{k}{\sqrt{2\epsilon}} K(k) \frac{4\epsilon}{k^3} \, dk$$

$$= \frac{8\sqrt{2\epsilon}}{3\pi} \int_\beta^1 \frac{K(k)}{k^2} \, dk$$

$$= \frac{8\sqrt{2\epsilon}}{3\pi} \left[-\frac{E(k)}{k} \right]_\beta^1 \tag{3.1.22}$$

$$= \frac{8\sqrt{2\epsilon}}{3\pi} \left(\frac{E(\beta)}{\beta} - 1 \right)$$

where $\beta^2 = \frac{2\epsilon}{1+\epsilon}$. If we convert the remaining piece of equation 3.1.8 so that the integration is over k instead of λ we have:

$$P2 = -\frac{\pi}{3} \int_\beta^1 \frac{\sqrt{2\epsilon}}{k} \frac{1}{K(k)} \left(1 + \frac{1 + \epsilon - \frac{2\epsilon}{k^2}}{-2\epsilon + \frac{2\epsilon}{k^2}} \frac{E(k)}{K(k)} \right) \frac{4\epsilon}{k^3} \, dk$$

$$= -\frac{2\pi\sqrt{2\epsilon}}{3} \int_\beta^1 \frac{1}{k^4 K(k)} \left(2\epsilon + \frac{k^2}{1 - k^2} (1 + \epsilon - \frac{2\epsilon}{k^2}) \frac{E(k)}{K(k)} \right) dk \tag{3.1.23}$$

Equation 3.1.23 will have to broken up into three parts to make evaluation of $P2$ simpler. Leaving aside the constant, we have

$$P2a = \int_\beta^1 \frac{2\epsilon}{k^4 K(k)} \, dk \tag{3.1.24}$$

$$P2b = \int_\beta^1 \frac{1 + \epsilon}{k^2 (1 - k^2)} \frac{E(k)}{K^2(k)} \, dk \tag{3.1.25}$$

$$P2c = \int_\beta^1 \frac{-2\epsilon}{k^4 (1 - k^2)} \frac{E(k)}{K^2(k)} \, dk \tag{3.1.26}$$

Leaving $P2a$ aside for the moment, the following formulae (not found in reference 11) will be of utility in integrating $P2b$ and $P2c$:

$$\int \frac{E(k)}{k^2 (1 - k^2) K^2(k)} \, dk = -\frac{1}{k K(k)} \tag{3.1.27}$$

$$\int \frac{2}{k^4 K(k)} \, dk + \int \frac{E(k)}{k^4 (1 - k^2) K^2(k)} \, dk = -\frac{1}{k^3 K(k)} \tag{3.1.28}$$

$P2b$ can be integrated using equation 3.1.27.

$$P2b = -(1 + \epsilon)\left[\frac{1}{kK(k)}\right]_\beta^1$$

$$= \frac{1+\epsilon}{\beta}\frac{1}{K(\beta)}$$

(3.1.29)

$P2c$ can be simplified using 3.1.28.

$$P2c = \int_\beta^1 \frac{4\epsilon}{k^4 K(k)}\,dk + 2\epsilon\left[\frac{1}{k^3 K(k)}\right]_\beta^1$$

$$= 4\epsilon\int_\beta^1 \frac{dk}{k^4 K(k)} - \frac{2\epsilon}{\beta^3}\frac{1}{K(\beta)}$$

(3.1.30)

Finally, we can express $I_{13,c}^{circ}$ in terms of the quantities $P1$, $P2a$, $P2b$ and $P2c$:

$$I_{13,c}^{circ} = \frac{8\sqrt{2\epsilon}}{3\pi}\left(\frac{E(\beta)}{\beta} - 1\right) - \frac{2\pi\sqrt{2\epsilon}}{3}\left(\frac{1 + \epsilon - \frac{2\epsilon}{\beta^2}}{\beta K(\beta)} + 6\epsilon\int_\beta^1 \frac{dk}{k^4 K(k)}\right)$$

(3.1.31)

where the last integral will have to be done using numerical quadrature in the absence of a suitable integration formula. Using the definition of β, the second term vanishes.

$$I_{13}^{circ} = \frac{8\sqrt{2\epsilon}}{3\pi}\left(\frac{E(\beta)}{\beta} - 1\right) - 4\pi\epsilon\sqrt{2\epsilon}\int_\beta^1 \frac{dk}{k^4 K(k)}$$

(3.1.32)

The equation 3.1.32 can thus be evaluated numerically (using the approximations for the complete elliptic integrals given in reference 12, see also Appendix A), and compared to the result for the trapped particles derived in equation 3.1.20. The result (for $\epsilon \approx \frac{1}{18}$) is that the outward circulating particle flux cancels 94% of the inward flux of trapped particles.

An explanation of the physical mechanism of the explicit fluxes is given in reference 8; what follows is a brief paraphrase. Consider an axisymmetric tokamak geometry. The toroidal field, B_ϕ, the poloidal current, and the electric field, $E_\phi > 0$, are all aligned in the positive $\hat{\phi}$ direction. $\sigma = +1$ corresponds to motion in the direction of the magnetic field which is mostly in the $\hat{\phi}$ direction. Because of the non-zero electric field and the gradients of the magnetic field, the guiding center of the particle will drift away from the original flux surface. The drift velocity, to first order in the Larmor radius expansion is given by:

$$\underline{v}_d = -u\underline{b} \times \nabla\left(\frac{u}{\Omega}\right)$$

(3.1.33)

where Ω is the (signed) gyrofrequency and μ and H are constant. The parallel velocity u can be written (for time independent fields) as:

$$u \approx \sigma\left(\frac{2}{m}(H - \mu B - q\Phi)\right)^{\frac{1}{2}}$$

(3.1.34)

-23-

where q is the particle charge and Φ is the electric potential, which can be expressed as:

$$\Phi = -R\phi E_\phi \qquad (3.1.35)$$

Taken the projection of $\underline{v}_d$ on the direction orthogonal to the flux surface gives,

$$\underline{v}_d \cdot \nabla\psi = uI\sigma\partial_s\left(\frac{u}{\Omega}\right) - uRB\partial_\phi\left(\frac{u}{\Omega}\right) \qquad (3.1.36)$$

where,

$$\sigma\partial_s = \underline{b}\cdot\nabla, \quad \partial_\phi = R\hat{\phi}\cdot\nabla, \quad I = RB_\phi \qquad (3.1.37)$$

and s is the direction along the field line. In the axisymmetric system, the Hamiltonian is independent of ϕ for trapped particles, since they can not accelerate indefinitely. A circulating particle can, in the limit of a collisionless plasma, accelerate indefinitely. In a collisional system this can never happen, except for the phenomenon of "runaway" particles. If the Hamiltonian is considered to be applicable to the representative circulating particle, which can not accelerate indefinitely, then the Hamiltonian is a constant, equal to H the particle energy. Therefore the Hamiltonian can be considered independent of ϕ for both circulating and trapped particles. Using this result, we can write:

$$\frac{\Delta\psi}{\Delta\tau} = uI\sigma\partial_s\left(\frac{u}{\Omega}\right) - RE_\phi \qquad (3.1.38)$$

where $ds = u\,dt$ Expressing this in differential form:

$$d\psi = I\sigma\,d\left(\frac{u}{\Omega}\right) - RE_\phi\,dt \qquad (3.1.39)$$

The first term on the right hand side is always positive. For $q > 0$, u will increase / decrease as the particle is accelerated / decelerated by the electric field for $\sigma = +1/-1$. If $q < 0$, u will decrease / increase as the particle is decelerated / accelerated by E_ϕ. The second term is always negative, because E_ϕ is by convention positive.

For a trapped particle, the first term in $d\psi$ contributes nothing, because u periodically passes through zero. Therefore in a time $\tau \approx \omega_b^{-1}$ the trapped particle drifts inwards

$$\psi(\tau) - \psi(0) = -\int_0^\tau RE_\phi\,dt \qquad (3.1.40)$$

This is the trapped particle pinch effect[9]. Briefly, the electric field accelerates or decelerates the particles, forcing them to spend more time in the region where there is an inward component of the $\underline{b} \times \nabla B$ drift.

For a circulating particle, in addition to this inward flow, there is a competing outward flow from the first term of equation 3.1.39. If the particle accelerates or decelerates enough during

the period of time τ, then this term can be the dominant term. The particles that undergo the largest change in velocity, relatively speaking, are the ones in the boundary layer. For the well circulating particles, the inward term may still be dominant, and this is why the expression for $\frac{\Delta \psi}{\Delta \tau}^{circ}$ (equation 3.1.12) changes sign. It can be shown[8] that the acceleration of the marginally circulating particles produces a large outward flow. This is most easily shown from the requirement that toroidal canonical angular momentum be conserved:

$$P_\phi = mR\sigma|u|\underline{b} \cdot \hat{\phi} - \frac{q}{c}\psi \tag{3.1.41}$$

For example; if we have a particle with $q > 0$, and $\sigma = +1$, then the acceleration due to E_ϕ means that $|u|$ increases. The requirement that P_ϕ be conserved means that the value of ψ must increase. If $q > 0$ and $\sigma = -1$, then $|u|$ decreases, but ψ must increase if P_ϕ is to be conserved. If $q < 0$ and $\sigma = +1$, the E_ϕ will decelerate the particle and $|u|$ decreases. This implies an increase in ψ. If $\sigma = -1$, then $|u|$ will increase because the electric field accelerate the particle and again ψ increases to conserve P_ϕ. These four cases are shown in Figure 3.1. For each of the cases, the solid circle represents the flux surface from which the particle is launched. The dashed line is the toroidal projection of the orbit that the particle would follow if $E_\phi = 0$. The spiral line terminating in an arrow denotes the particle orbit with a finite E_ϕ. (Note: these plots are not to scale, they have been exaggerated to show the boundary layer effect).

The effect of collisions on the boundary layer particles can be understood by further examination of equation 3.1.39. As we have seen, the first term on the right hand side makes no contribution towards $d\psi$ for the trapped particles, because u passes through zero periodically, i.e. there is no continuous acceleration or deceleration. Consider now the case of the marginally circulating particles with a low level of collisionality. On the inside of the torus, the $\cos\eta$ of these particles will be near zero, thus a scattering event could easily make a considerable change in magnitude of the parallel velocity, as well as changing σ. This change in the direction of the parallel velocity again means that there is no continuous acceleration or deceleration, thus we would expect that the $d\psi$ value for the marginal particles in the finite ν_* case should not exhibit the same behavior as in the ideal banana case.

A detailed calculation of $I_{13,e}$ as a function of the dimensionless collision frequency ν_* is given in reference 6. The trapped particle contribution is unaffected by scattering, and the circulating contribution can be written as:

$$I_{13,e}^{circ} = 1 - \frac{\pi^2}{\log\left(\frac{258}{\nu_*}\right)} \tag{3.1.42}$$

This expression has been normalized to the trapped particle contribution, i.e. at $\nu_* = 0$, $I_{13,e}^{circ} = 1$ and $I_{13,e}^{trap} = -1$. The collisionality parameter ν_* is defined by the expression:

$$\nu_* = \frac{\nu}{\omega_{b0}(2\epsilon)^{\frac{3}{2}}}$$

(3.1.43)

where ν is the collision frequency and ω_{b0} is the bounce frequency of the $\lambda = 0$ particles.
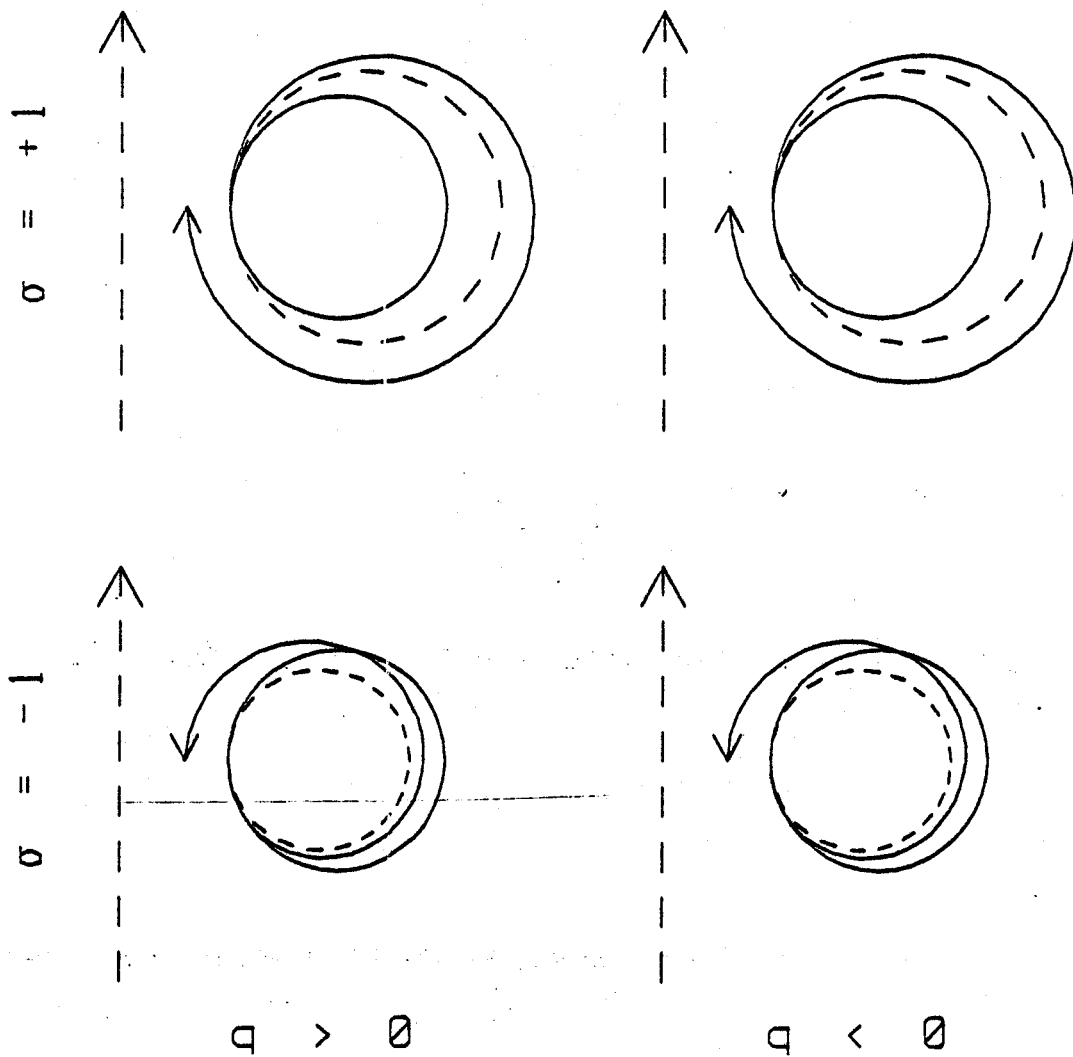
Figure 3.1: Boundary layer particle orbits

3.2. The Explicit Currents

In this section we will present the ideal theory expressions for the explicit current transport coefficients. Both the trapped and circulating currents are essentially diamagnetic in nature. The trapped particle contribution is sometimes called the banana current. Its origin is similar to the diamagnetic current arising from the gyration of particles in the presence of a density gradient. In this case, the banana motion of the trapped particles combined with the density gradient produces a net toroidal current. The circulating particles also produce a toroidal diamagnetic current. It may be large locally, but it changes sign as one moves from the inside to the outside of the torus. The poloidal averaging of this process produces a small net current. It will be shown that the trapped and circulating contributions are of order $\epsilon^{\frac{3}{2}}$. In the previous section, we have seen that the pinch coefficients are of order $\epsilon^{\frac{1}{2}}$, but they cancel to leading order, leaving a small order $\epsilon^{\frac{3}{2}}$ net result. Thus the explicit pinch and explicit current transport coefficients, in the limit $\nu_* \to 0$, obey an Onsager symmetry relationship[6-8].

The explicit current transport coefficient $T_{31,e}$ can be expressed in a manner analogous to the pinch coefficient in the preceding section[8]:

$$T_{31,e}^{trap} = 2nT \int_0^\infty d\left(\frac{H}{T}\right)\left(\frac{H}{T}\right)^{\frac{3}{2}} \exp\left(-\frac{H}{T}\right) \int_{1-\epsilon}^{1+\epsilon} S_{31,e}(\lambda)^{trap} \, d\lambda \qquad (3.2.1)$$

$$T_{31,e}^{circ} = nT \sum_\sigma \int_0^\infty d\left(\frac{H}{T}\right)\left(\frac{H}{T}\right)^{\frac{3}{2}} \exp\left(-\frac{H}{T}\right) \int_0^{1-\epsilon} S_{31,e}(\lambda)^{circ} \, d\lambda \qquad (3.2.2)$$

where

$$S_{31,e}(\lambda)^{trap} = \sqrt{2\epsilon}\frac{2}{\pi}\left(E(k^{-1}) - \frac{k^2-1}{k^2}K(k^{-1})\right) \qquad (3.2.3)$$

$$S_{31,e}(\lambda)^{circ} = \sqrt{1+\epsilon-\lambda}\left(\frac{2}{\pi}E(k) - \frac{\pi}{2K(k)}\right) \qquad (3.2.4)$$

k has been defined by equation 3.1.4. As in the previous section, note that the energy dependence of the transport coefficient is the same for both trapped and circulating particles. The energy integral can be done, and the result is:

$$T_{31,e}^{trap} = \frac{3}{4}nTI_{31}^{trap} \qquad (3.2.5)$$

$$T_{31,e}^{circ} = \frac{3}{4}nTI_{31}^{circ} \qquad (3.2.6)$$

where

$$I_{31,\epsilon}^{trap} = 2\pi \int_{1-\epsilon}^{1+\epsilon} S_{31,\epsilon}(\lambda)^{trap} \, d\lambda \qquad (3.2.7)$$

$$I_{31,\epsilon}^{circ} = 2\pi \int_{0}^{1-\epsilon} S_{31,\epsilon}(\lambda)^{circ} \, d\lambda \qquad (3.2.8)$$

All that remains to be done is to perform the $I_{31,\epsilon}$ integrals.

$$I_{31,\epsilon}^{trap} = 2\pi\sqrt{2\epsilon}\frac{2}{\pi} \int_{1-\epsilon}^{1+\epsilon} \left(E(k') - (1 - (k')^2)K(k')\right) d\lambda \qquad (3.2.9)$$

where $k' = 1/k$. Changing the integration variable to k', we have:

$$
\begin{aligned}
I_{31,\epsilon}^{trap} &= 16\epsilon\sqrt{2\epsilon} \int_{0}^{1} \left(E(k') - (1 - (k')^2)K(k')\right) k' \, dk' \\
&= \frac{16}{9}\epsilon\sqrt{2\epsilon}[(4(k')^2 - 2)E(k) - (1 - (k')^2)(3(k')^2 - 2)K(k')]_{0}^{1} \qquad (3.2.10) \\
&= \frac{32}{9}\epsilon\sqrt{2\epsilon}
\end{aligned}
$$

Turning to the circulating particle current:

$$
\begin{aligned}
I_{31,\epsilon}^{circ} &= 2\pi \int_{0}^{1-\epsilon} \sqrt{1 + \epsilon - \lambda}\left(\frac{2}{\pi}E(k) - \frac{\pi}{2K(k)}\right) d\lambda \\
&= 8\pi\epsilon\sqrt{2\epsilon}\left(\frac{2}{\pi}\int_{\beta}^{1} k^{-4}E(k)\,dk - \frac{\pi}{2}\int_{\beta}^{1} \frac{dk}{k^4 K(k)}\right) \\
&= 16\epsilon\sqrt{2\epsilon}\left[\frac{1}{9k^3}(2(k^2 - 2)E(k) + (1 - k^2)K(k))\right]_{\beta}^{1} - 4\pi^2\epsilon\sqrt{2\epsilon}\int_{\beta}^{1} \frac{dk}{k^4 K(k)} \\
&= \frac{16}{9}\epsilon\sqrt{2\epsilon}(-2 + \beta^{-3}((4 - 2\beta^2)E(\beta) - (1 - \beta^2)K(\beta))) - 4\pi^2\epsilon\sqrt{2\epsilon}\int_{\beta}^{1} \frac{dk}{k^4 K(k)}
\end{aligned}
\qquad (3.2.11)
$$

where $\beta^2 = \frac{2\epsilon}{1+\epsilon}$ and the last integral will have to be done numerically. Notice that the result will be of order $\epsilon^{\frac{3}{2}}$. If we evaluate these expressions for $I_{31,\epsilon}$ we see that the trapped current is the dominant contribution. The circulating contribution is difficult to evaluate; it is a small number resulting from the near cancellation of two large numbers. Because one of the large numbers is the result of a numerical integration, there will be some error in the result calculated for $I_{31,\epsilon}^{circ}$. For the value of ϵ used in our model, we find that the circulating particle contribution is approximately 30% of the trapped particle explicit current.

3.3. The Implicit Processes

The implicit transport coefficients are the result of collisional processes. The implicit flows arise from the cross processes[6] in the collision operator, that is they are the result of coupling the space-like action ψ with the two velocity-like actions μ and J. The trapped particles make no contribution to the implicit transport coefficients[7,8].

The physical mechanism behind the implicit pinch can be understood by considering two, initially well circulating, particles moving in opposite directions on the same bounce averaged flux surface ψ (see Figure 3.2). As the particles scatter towards trapped space, the $\sigma = -1$ particle scatters to an orbit which is shifted inward relative to ψ, while the $\sigma = +1$ particle scatters in the opposite direction. This is the origin of the correlation between velocity and radial scattering. A current, driven by the toroidal electric field, means that the plasma not have equal numbers of $\sigma = \pm 1$ particles. The imbalance of forward and backward particles will cause a radial flow of particles. This is the implicit pinch effect.

The mechanism behind the implicit bootstrap current is the reverse of the process described above. Take two marginally circulating particles, oppositely directed along the magnetic field, and scatter them back towards the well circulating state. The $\sigma = -1$ particles will scatter out towards $\overline{\psi}$, while the $\sigma = +1$ particles scatter in. If the plasma has a normal (i.e. $\nabla n < 0$) density gradient, there will be more $\sigma = -1$ particles than $\sigma = +1$ on the final average flux surface ψ. This is the implicit bootstrap current. It is the precise microscopic inverse to the implicit pinch effect[6], which accounts for the Onsager symmetry of the respective transport coefficients.

The quantity $\langle \frac{\Delta \mu \Delta \psi}{\Delta r} \rangle$ is related to D_{13} in reference 7. When the expressions for D_{13} from references 7 and 8 are evaluated, we have:

$$D_{13}^{circ} = -\nu \mu \omega_b^{circ} \left(1 - \frac{1}{1-k^2} \frac{E^2(k)}{K^2(k)} \right) \tag{3.3.1}$$

$$D_{13}^{trap} = 0 \tag{3.3.2}$$

where ν is the collision frequency and $k^2 = \frac{2\epsilon}{1+\epsilon-\lambda}$. One important thing to note is that the derivation of D_{13} is carried out in the limit $\nu \to 0$, much as the derivations of $I_{13,\epsilon}$ and $\frac{\Delta \psi}{\Delta r}$ were done in the limit $E_\phi \to 0$. The reason why the trapped particles do not make any contribution to D_{13} is easy to see; a scattering event will increase or decrease μ, which will lead to a larger or smaller banana respectively. This leads to a jump in the value of ψ. However, the bounce averaged flux, $\overline{\psi}$ will not show this jump. The ideal theory is in terms of $\overline{\psi}$, not ψ, so the trapped particle contribution to D_{13} is zero.
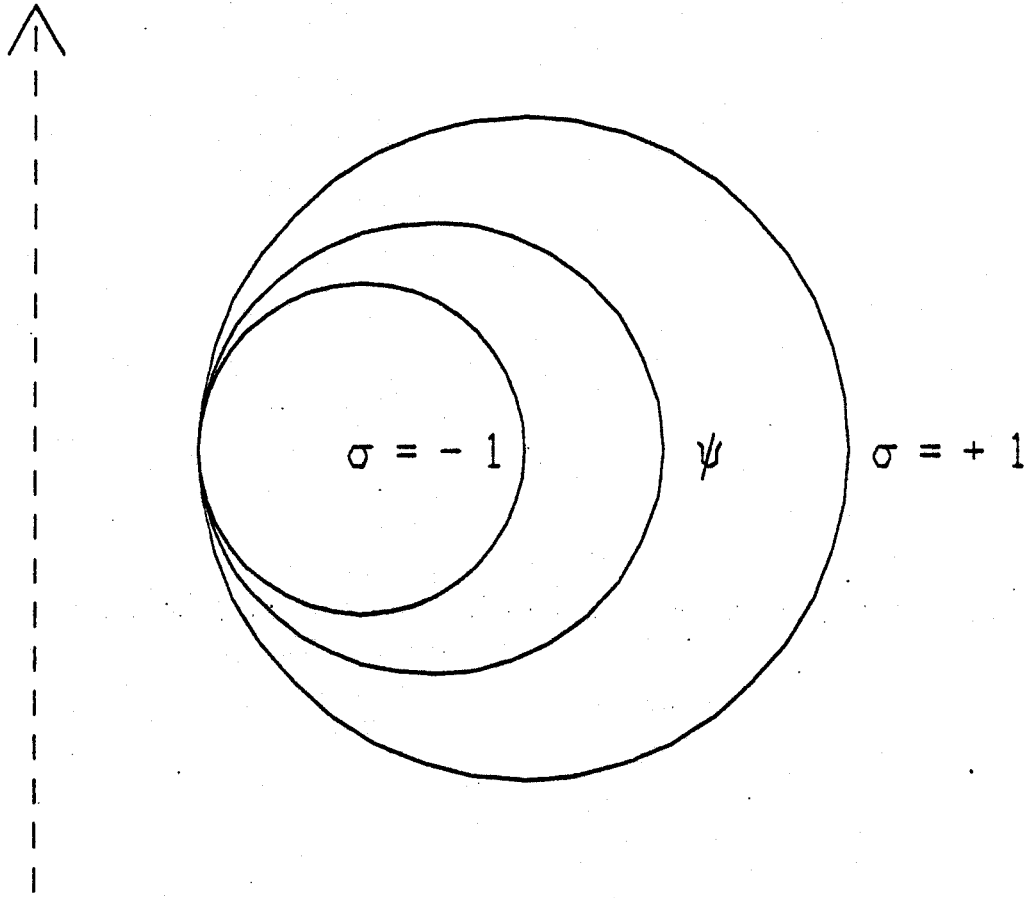
Figure 3.2: Representative orbits for circulating particles

3.4. Onsager Symmetry Breaking

In this section, the predictions of both the ideal banana theory and the finite ν_* theory, with respect to the Onsager symmetry of the pinch effect and bootstrap current will be summarized. In the ideal banana theory, both the explicit and implicit transport matrices are exhibit Onsager symmetry. The implicit pinch and bootstrap processes have been shown to be the microscopic inverses of each other (see Section 3.3 and reference 8). The explicit symmetry relationship is between the banana and Pfirsch-Schluter currents and the kinematic pinch effect. The explicit currents are diamagnetic in nature, and the resulting transport coefficient is of $O(\epsilon^{\frac{3}{2}})$. The kinematic pinch coefficient is the result of the cancellation of the inward trapped particle pinch (the Ware effect[9]) by an outward flux of circulating particles (see Section 3.1). Most of the circulating particle flux comes from a narrow region in λ-space near the trapped-circulating boundary. Both the trapped and circulating contributions are of $O(\epsilon^{\frac{1}{2}})$, so the net explicit pinch coefficient is of $O(\epsilon^{\frac{3}{2}})$.

The addition of scattering produces several effects. The implicit transport coefficients, while still maintaining their Onsager symmetry relationship, greatly decrease with increasing ν_*. This is due to the destruction of the "cross processes" (see Section 3.3), which couple the velocity-like and space-like actions. The trapped particle explicit pinch coefficient is unaffected by low levels of scattering, but the circulating particle contribution to the kinematic pinch will be reduced by collisions. This is because the marginally circulating particles will tend to scatter towards a well circulating state, thus "smearing out" the boundary layer. Reduction of the outward flow of circulating particles leaves the inward trapped particle pinch as the dominant effect. To summarize: the finite ν_* theory predicts that scattering will destroy the implicit pinch effect and bootstrap current and reduce the circulating particle contribution to the explicit pinch effect. The result (to $O(\epsilon^{\frac{1}{2}})$) is that the bootstrap current is largely destroyed and the pinch effect is dominated by the Ware effect.

Model Description and Numerical Methods

In this chapter, the details of the models used in the numerical simulation of particle orbits are presented, along with a discussion of the numerical methods used to integrate the particle equations of motion and to determine the toroidal magnetic flux. In Chapter 2, the reasons behind the choice of magnetic field, electric field and scattering models were presented. Here the actual numerical means of evaluating the magnetic field for example will be given.

In Section 4.1, the axisymmetric magnetic field model is presented, and some of its properties, such as the magnetic well, safety factor and flux surfaces are described. The next two sections describe the scattering and density models respectively. Section 4.4 contains a description of the method by which the toroidal magnetic flux ψ is calculated at an arbitrary location, and Section 4.5 discusses the problem of particle following, and a brief description of the computer code is given.

4.1. Magnetic Field Model

The model of the magnetic field is made up of three parts; a $1/R$ toroidal field, a constant vertical field, and a poloidal field from a current loop. In this section, the expressions for the vector potential, magnetic field, and the gradients of the magnetic field will be derived. Also, the properties of the model such as the safety factor (inverse rotational transform) and the depth of the magnetic well will be discussed. In the final subsection, a listing of the parameters used in the model will be given.

4.1.1. Magnetic Field Calculations

The magnetic field from each of the three components is calculated from the Biot-Savart Law. In addition to the magnetic field $\underline{B}$, $\nabla \underline{B}$ and the vector potential $\underline{A}$ will be needed for particle following and the flux calculation respectively. The Biot-Savart Law can be written as:[13]

$$\underline{A} = \frac{\mu_0}{4\pi} \int_{\tau'} \frac{\underline{J}}{x} d\tau' \qquad (4.1.1)$$

where x is the distance from the current element to the point $\underline{r}$ and τ' is the dummy volume element of integration.

The toroidal magnetic field can be considered to be generated by a current flowing in the $\hat{z}$ direction located at the origin. Analytic expressions for A_z and B_ϕ can be obtained by using equation 4.1.1 and differentiating.

To apply equation 4.1.1, an expression for the current density J_z is needed. If we consider the current to flow through an infinitely thin filament, the r and ϕ dependence of J_z are expressible as delta functions. Thus equation 4.1.1 can be written as:

$$A_z = \frac{\mu_0}{4\pi} \int_{-L}^{L} \frac{I}{\sqrt{(z')^2 + r^2}} dz' \qquad (4.1.2)$$

where L is one half of the length of the filament, and z' is the dummy variable of integration in the $\hat{z}$ direction. The denominator of the integrand is found from the geometric relation

$$x^2 = (z')^2 + r^2 \qquad (4.1.3)$$

Equation 4.1.2 can be re-written as:

$$A_z = \frac{\mu_0 I}{2\pi} \int_{0}^{L} \frac{dz'}{\sqrt{(z')^2 + r^2}} \qquad (4.1.4)$$

This can be integrated, and inserting the limits, the result is:

$$A_z = \frac{\mu_0 I}{2\pi} \left[\log(L + \sqrt{r^2 + L^2}) - \log(r) \right] \qquad (4.1.5)$$

If we consider the limit of $L^2 \gg r^2$ equation 4.1.5 can be simplified to:

$$A_z = \frac{\mu_0 I}{2\pi} \log \frac{2L}{r} \qquad (4.1.6)$$

The toroidal magnetic field can be calculated by taking the curl of equation 4.1.6:

$$B_\phi = -\frac{\partial A_z}{\partial r} \qquad (4.1.7)$$

$$B_\phi = \frac{\mu_0 I}{2\pi r} \qquad (4.1.8)$$

The only derivative of B_ϕ which is not identically zero is the derivative with respect to r. Differentiating equation 4.1.8 we have:

$$\frac{\partial B_\phi}{\partial r} = -\frac{\mu_0 I}{2\pi r^2} \tag{4.1.9}$$

The poloidal field will be generated by a circular current loop in the $z = 0$ plane. The complete calculation of A_ϕ, the poloidal field and $\nabla \underline{B}$ is presented in Appendix A; the results are:

$$A_\phi = \frac{\mu_0 I}{\pi} \frac{a}{((a+r)^2 + z^2)^{\frac{1}{2}}} \left(2\frac{K(m)}{m} - 2\frac{E(m)}{m} - K(m) \right) \tag{4.1.10}$$

$$B_r = \frac{\mu_0 I}{2\pi r} \frac{z}{\sqrt{(a+r)^2 + z^2}} \left(-K + \frac{2-m}{2(1-m)} E \right) \tag{4.1.11}$$

$$B_z = \frac{\mu_0 I}{2\pi} \frac{1}{\sqrt{(a+r)^2 + z^2}} \left(K - \frac{E}{1-m} \left(1 - \frac{m}{2r}(a+r) \right) \right) \tag{4.1.12}$$

$$\frac{\partial B_z}{\partial z} = -\frac{B_r}{r} - \frac{\partial B_r}{\partial r} \tag{4.1.13}$$

$$\frac{\partial B_r}{\partial z} = -\frac{B_r z}{(a+r)^2 + z^2} + \frac{\mu_0 I}{2\pi r} \frac{1}{\sqrt{(a+r)^2 + z^2}} \left(-K + \frac{2-m}{2(1-m)} E \right)$$
$$+ \frac{\mu_0 I}{2\pi r} \frac{z}{\sqrt{(a+r)^2 + z^2}} \frac{1}{4(1-m)} \frac{\partial m}{\partial z} \left(-K + \frac{1+m}{1-m} E \right) \tag{4.1.14}$$

$$\frac{\partial B_r}{\partial r} = -B_r \left(\frac{1}{r} + \frac{a+r}{(a+r)^2 + z^2} \right) + \frac{\mu_0 I}{2\pi r} \frac{z}{\sqrt{(a+r)^2 + z^2}} \frac{1}{4(1-m)} \frac{\partial m}{\partial r} \left(-K + \frac{1+m}{1-m} E \right) \tag{4.1.15}$$

$$\frac{\partial B_z}{\partial r} = -\frac{B_z(a+r)}{(a+r)^2 + z^2} + \frac{\mu_0 I}{2\pi} \frac{1}{\sqrt{(a+r)^2 + z^2}} \frac{1}{4r(1-m)} \left[\frac{\partial m}{\partial r} \left(K(r-a) \right. \right.$$
$$\left. \left. + E\left(a+r - \frac{2(r-a)}{1-m} \right) \right) - E \frac{2am}{r} \right] \tag{4.1.16}$$

where K and E are the complete elliptic integrals of the first and second kind, a is the dipole radius, I is the dipole current, and m is defined by:

$$m = \frac{4ar}{(a+r)^2 + z^2} \tag{4.1.17}$$

A vertical field will be used to shift the magnetic surfaces. A very simple model of a vertical field will be used: a homogeneous field in the $-\hat{z}$ direction. This will shift the outer surfaces inward and produce a magnetic well (see subsection 4.1.2). If we let B_v be the value of the vertical field ($B_v < 0$), the vector potential associated with B_v will be composed of $\hat{\phi}$ and $\hat{r}$ components. The constraint of axisymmetry leaves only A_ϕ, which can be expressed as:

$$A_\phi = \frac{1}{2}rB_v \qquad (4.1.18)$$

where the constant of integration has been eliminated by the desire for a finite value of A_ϕ at $r = 0$.

4.1.2. The Safety Factor and the Magnetic Well

Calculating the safety factor (or inversely, the rotational transform) is a trivial process in this axisymmetric geometry. Integrating the equations given in the previous subsection, the toroidal angle that the line traverses while completing one poloidal orbit, $\Delta\phi$, is computed. The safety factor q is the ratio of the number of toroidal orbits to the number of poloidal orbits. Thus:

$$q = \frac{\Delta\phi}{2\pi} \qquad (4.1.19)$$

Determining if there is a magnetic well or an anti-well is a little more complicated; first we must clarify what we mean by a magnetic well. According to Taylor[14] a magnetic well is present when there is a point (or a simple closed curve) such that the value of B^2 increases as you move in a "radial" direction (it should be noted that in general the contours of B^2 are not the flux surfaces). When this condition is satisfied, there is said to be an absolute magnetic well, or a min-B configuration. With the addition of Ioffe bars to a simple axisymmetric mirror, an absolute magnetic well is produced.

Because of the $1/R$ toroidal field in most toroidal geometries, an absolute magnetic well is not possible. However, an average magnetic well can be produced if on a given flux surface, the average value of B^2 is larger than on a flux surface closer to the magnetic axis[15].

There remains the question of what the proper average along the flux surface should be. Because of the axisymmetry of our geometry, the flux surface average is just an average along a field line for one poloidal period. Examination of the equations describing the field line (see subsection 4.4.2) yields the following flux surface average:

$$\langle Y \rangle = \frac{\oint \frac{dl}{B} Y}{\oint \frac{dl}{B}} \qquad (4.1.20)$$

where Y is the quantity to be averaged, and the $\oint$ refers to the one poloidal period. Using this definition to calculate the average of B^2 we find:

A vertical field will be used to shift the magnetic surfaces. A very simple model of a vertical field will be used: a homogeneous field in the $-\hat{z}$ direction. This will shift the outer surfaces inward and produce a magnetic well (see subsection 4.1.2). If we let B_v be the value of the vertical field ($B_v < 0$), the vector potential associated with B_v will be composed of $\hat{\phi}$ and $\hat{r}$ components. The constraint of axisymmetry leaves only A_ϕ, which can be expressed as:

$$A_\phi = \frac{1}{2} r B_v \tag{4.1.18}$$

where the constant of integration has been eliminated by the desire for a finite value of A_ϕ at $r = 0$.

4.1.2. The Safety Factor and the Magnetic Well

Calculating the safety factor (or inversely, the rotational transform) is a trivial process in this axisymmetric geometry. Integrating the equations given in the previous subsection, the toroidal angle that the line traverses while completing one poloidal orbit, $\Delta\phi$, is computed. The safety factor q is the ratio of the number of toroidal orbits to the number of poloidal orbits. Thus:

$$q = \frac{\Delta\phi}{2\pi} \tag{4.1.19}$$

Determining if there is a magnetic well or an anti-well is a little more complicated; first we must clarify what we mean by a magnetic well. According to Taylor[14] a magnetic well is present when there is a point (or a simple closed curve) such that the value of B^2 increases as you move in a "radial" direction (it should be noted that in general the contours of B^2 are not the flux surfaces). When this condition is satisfied, there is said to be an absolute magnetic well, or a min-B configuration. With the addition of Ioffe bars to a simple axisymmetric mirror, an absolute magnetic well is produced.

Because of the $1/R$ toroidal field in most toroidal geometries, an absolute magnetic well is not possible. However, an average magnetic well can be produced if on a given flux surface, the average value of B^2 is larger than on a flux surface closer to the magnetic axis[15].

There remains the question of what the proper average along the flux surface should be. Because of the axisymmetry of our geometry, the flux surface average is just an average along a field line for one poloidal period. Examination of the equations describing the field line (see subsection 4.4.2) yields the following flux surface average:

$$\langle Y \rangle = \frac{\oint \frac{dl}{B} Y}{\oint \frac{dl}{B}} \tag{4.1.20}$$

where Y is the quantity to be averaged, and the $\oint$ refers to the one poloidal period. Using this definition to calculate the average of B^2 we find:

$$\langle B^2 \rangle = \frac{\oint B dl}{\oint \frac{dl}{B}}$$

<div align="right">(4.1.21)</div>

4.1.3. Model Parameters

Only a few parameters are needed to completely specify the magnetic field used in this thesis. The toroidal field can be specified by two quantities; the current in the filament and the length of the filament. The poloidal field model can also be described by two parameters; the current in the dipole and the radius of the dipole, which is the magnetic axis of the system. For the vertical field there is only one parameter; the field strength.

In Figures 4.1 and 4.2, the safety factors, magnetic wells and flux surfaces are compared for the cases of $B_v = 0$ and $B_v = -0.008$ Tesla. The major radius is 10.0 meters and the toroidal current is 0.2 MA. The current which produces the toroidal field is 200 MA, which gives $B_\phi = 2.0$ T at the major radius. The length of the current filament is 10 km; the length only enters into the A calculation, the large value of the length is to avoid any "end effects".

The reason why a vertical field is necessary is apparent from Figures 4.1 and 4.2. Without the vertical field, the flux surfaces are shifted out relative to the magnetic axis by the toroidal effects. Hence there is an anti-well. With the addition of the small vertical field, the outer flux surfaces are shifted inward, producing a well. There is still an anti-well in the center; this is unavoidable because a vertical field strong enough to create a well here would destroy the outer flux surfaces. The central anti-well should not be a problem, as our transport studies will be confined to the area where there is a magnetic well.
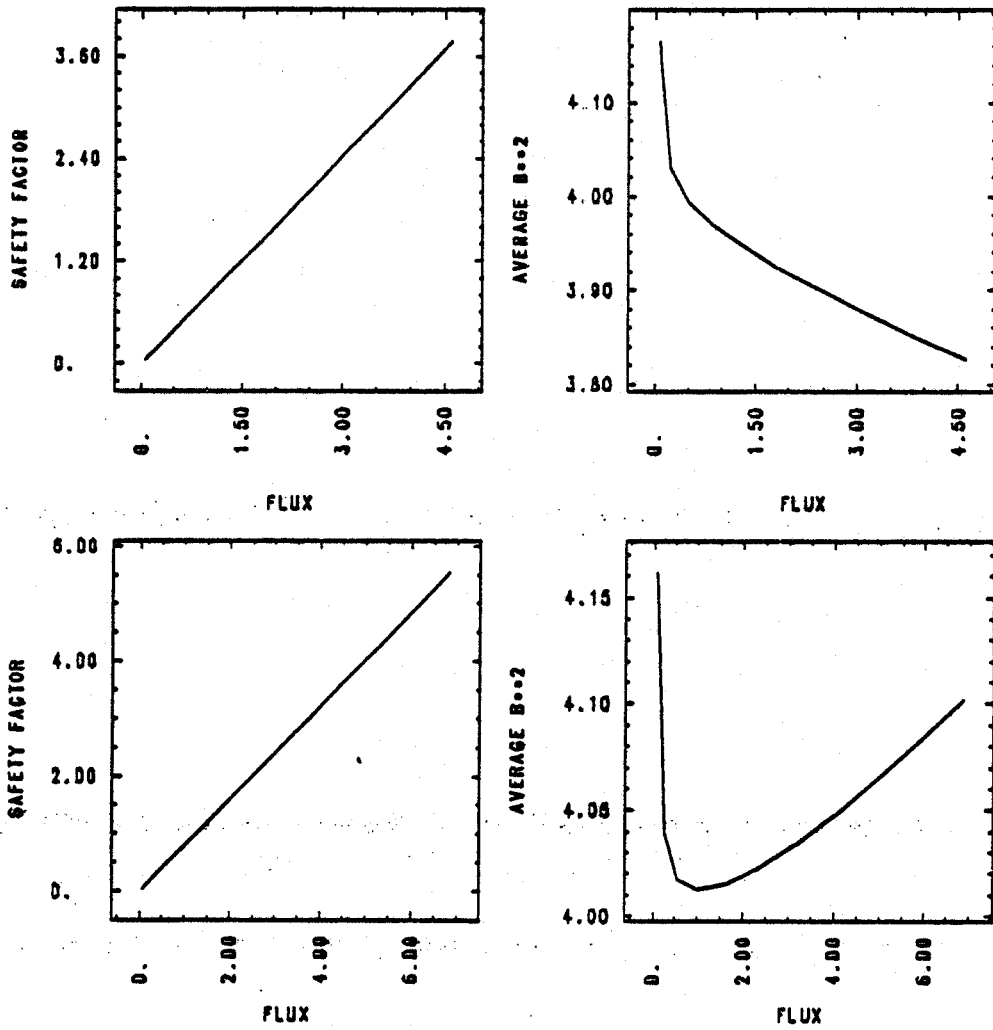
Figure 4.1: safety factor and magnetic well

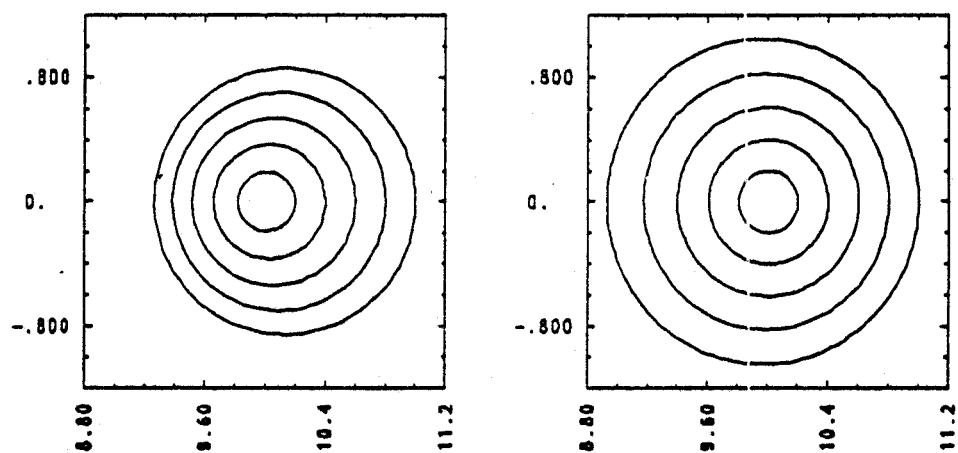top: $B_v = 0.0$

bottom: $B_v = -0.008$ T

Figure 4.2: ϕ projection of flux surfaces

left: $B_v = 0.0$

right: $B_v = -0.008$ T

4.2. Scattering Models

In this section, a brief description of the methods used to model collisions will be given. We have considered two kinds of models for the scattering process, pitch angle scattering (at constant energy), and energy scattering at constant magnetic moment.

4.2.1. Pitch Angle Scattering

Pitch angle scattering is modeled by a Lorentz collision operator:

$$\frac{\partial f}{\partial t} = \frac{\nu}{2}\frac{\partial}{\partial \cos\eta}(1 - \cos^2\eta)\frac{\partial f}{\partial \cos\eta} \tag{4.2.1}$$

where f is the particle phase space density, ν is the collision frequency, and η is the pitch angle. In reference 16, a Monte Carlo equivalent operator based on the binomial distribution is derived.

$$\cos\eta = \cos\eta_0(1 - \nu\tau) + x\sqrt{(1 - \cos^2\eta_0)\nu\tau} \tag{4.2.2}$$

where η is the pitch angle after scattering, η_0 is the pitch angle before scattering, and τ is the time step. x is randomly chosen to be ± 1. The advantage to using this collision operator is that $|\cos\eta|$ will never exceed 1. If τ is chosen to be smaller than the integration time step (so the scattering operator is applied several times for one time step), the net result will approach a Gaussian distribution. Instead of following this procedure, we chose x to be a normally distributed random number ($\sigma^2 = 1$), which is obtained using the Box-Muller transformation[17]. Thus the scattering operator resembles those described in references 18 and 19. The advantage is that this is much faster, however it will be possible for $|\cos\eta|$ to exceed 1. Fortunately, for small ν, the problem with $|\cos\eta|$ only occurs for particles with $|\cos\eta| \approx 1$, i.e. the well circulating particles. These particles make little contribution to the transport coefficients; so in practice, if the value of x yields a nonphysical result for $\cos\eta$ for these particles, a new x is chosen.

This scattering operator was tested by following a particle for several hundred thousand time steps, using a large value of ν to simulate the actual collision frequency calculated from the Braginskii collision frequency. It is expected that the distribution of the particle's $\cos\eta$ values should approach a uniform distribution, and this is indeed the case.

4.2.2. Energy Scattering

The energy scattering model is similar to the pitch angle scattering algorithm above. An energy step, ΔH, is used as the standard deviation of a normally distributed jump in energy. The energy jump is then added to the parallel energy of the particle, keeping μ constant. The new value of the parallel velocity, which is a dependent variable in the calculation is then computed from the new parallel energy. It should be noted that the parallel energy is signed, so that if the

energy jump should cause the parallel energy to change sign, the effect is to make the parallel velocity change sign.

This scattering model has been used only for comparison with the pitch angle scattering model. The results presented in the next chapter were obtained using the pitch angle scattering method; qualitatively, the same results were obtained using the energy scattering model.

4.3. Plasma Density Model

For some of the transport coefficient calculations, e.g. the kinematic bootstrap current, the particle density is needed. We have chosen a relatively simple model of the density:

$$ n = n_0 \left(1 - \frac{\psi}{\psi_a} \right)^p \tag{4.3.1} $$

where n_0 is the density at the magnetic axis and ψ_a is the value of the toroidal flux at some large minor radius. The parameters used were $n_0 = 1.0 \times 10^{20}$ m^{-3}, $\psi_a = 5.0$ Wb (the flux surface from which the particles were launched was $\psi = 2.0$ Wb) and $p = 1.0$.

4.4. Calculation of the Toroidal Flux Coordinate

In this section, the methods used to obtain ψ at a given location are discussed. In subsection 4.4.1, the integral representation of the toroidal flux will be given for the magnetic field model. The integration path will be the toroidal projection of a field line. The next subsection deals with field line following. calculation of ψ by following a field line is relatively inexpensive in cpu time; about 1.5 CRAY cpu seconds is required to compute ψ for a typical point. However, some of the transport calculations will require a flux value at every time step of the particle following code. This would be prohibitively expensive in computer time. Instead, a cubic B-spline interpolation method is used. The interpolation procedure will be outlined in the final subsection.

4.4.1. Evaluating the Toroidal Flux

In evaluating the transport coefficients, one of the important parameters is the magnetic flux. The flux serves as a measure of the particle's position relative to the magnetic axis. The particle motion will be mostly along the the field line, so it is the slow drift across the flux surfaces which we are measuring. To calculate the value of ψ at any point, we will make use of the magnetic field model given in Section 4.1.

If we are given a closed path in a toroidal plane ($\phi = 0$) which represents a "contour of constant flux", the value of ψ can be determined by doing the surface integral:

$$\psi = \int\int \underline{B} \cdot \hat{n} dA \qquad (4.4.1)$$

where dA is the differential area element and $\hat{n}$ is a unit vector describing the orientation of the surface element. Using the toroidal symmetry of our model, equation 4.4.1 simplifies to:

$$\psi = \int\int B_\phi dr dz \qquad (4.4.2)$$

Using Stokes theorem, equation 4.4.1 can be written in terms of the vector potential and a line integral.

$$\psi = \oint \underline{A} \cdot d\hat{s} \qquad (4.4.3)$$

where $d\hat{s}$ is the differential element along the path of integration. Again, using the description of our model, the only component of the vector potential which contributes to the integral is A_z, for which we have derived a simple algebraic formula in subsection 4.1.1. The path of integration is just the toroidal projection ($\phi = 0$) of a field line, as it completes one poloidal orbit.

4.4.2. Field Line Following

The "motion" of a field line is described by the set of equations:

$$\frac{dr}{B_r} = \frac{rd\phi}{B_\phi} = \frac{z}{B_z} = \frac{dl}{|B|} \qquad (4.4.4)$$

where dl is the differential length element along the field line. To determine the trajectory of a field line, the equations 4.4.4 must be integrated. A fourth order predictor–corrector algorithm was used to do the integration. This method was chosen because it gives fourth order accuracy with only two function evaluations per step, while other fourth order schemes, like the Runge–Kutta method, require four function evaluations. In this case (and in the case of particle following) the function evaluations require calculation of the magnetic fields, and thus require many operations.

A disadvantage of the predictor–corrector method, is that it requires data at three previous points before it can calculate the fourth point. This means that some other method must be used to do the first several integrations; here the Runge–Kutta method is used. Also, the predictor–corrector method is limited to a fixed step size.

The accuracy of the code was studied in two ways. First, the portion of the code which calculates the magnetic field was benchmarked against an analytic calculation of the field. The accuracy of the integrator was determined by following a field line for a long distance (several kilometers or $\sim$ 100 toroidal orbits) and then reversing the direction of "motion" and following the line back to the original starting point. The distance between the origin and the final stopping point is a measure of the accuracy of the integrator. It was found that halving the step size (doubling

the amount of work) improves the accuracy by a factor of thirty-two, which is as expected from a fourth order integration scheme.

4.4.3. Flux Calculation and Interpolation

The toroidal flux ψ is calculated using the expression:

$$\psi = \oint A_z \, dz \tag{4.4.5}$$

where the path of integration for the line integral is the toroidal projection ($\phi = 0$) of the field line. The integration is done as part of the line following procedure, using the trapezoidal rule. There is a problem with the last point in the integration because in practice the field line never completes a poloidal orbit exactly on the starting point; the last point will overlap on the first step. Thus there are two bounds to ψ from the last step and the next-to-last step. A simple linear interpolation, based on the distance on the toroidal projection plane ($\phi = 0$), is used to get a best estimate" of ψ. As a test of this procedure, two magnetic field models were used, the difference being in the length of the current filament which produces the toroidal field. B_ϕ is independent of the length of the filament, so ψ should also be constant, even though A_z will increase as the length increases. This is because ψ is determined from a closed integration path. It was found that the values of the two bounds of ψ changed, but the value of ψ remained constant, with an error of $\pm 1.0 \times 10^{-10}$

Calculation of the flux at a given point requires following a field line from that point for one poloidal orbit. As mentioned above, this can be an extremely costly way to determine ψ at each time step in the particle following code. Instead, the flux will be calculated for a rectangular grid, and the flux evaluations made as part of the particle following code will be done by using an interpolation scheme on this grid. The interpolation method used is two-dimensional, cubic B-splines[20−22]. To reduce the required cpu time even farther, a reduced storage matrix inversion routine, based on the LU decomposition algorithm, is used in place of a more general matrix inverter (see Appendix B).

A fairly complete discussion of cubic B-spline interpolation is given in references 20, 21 and 22. The two topics which will be addressed here are the boundary conditions and the accuracy of the interpolation. In order to completely specify the interpolation problem, boundary conditions are needed. In practice, the boundary condition is a function value, or the derivative of the function. Periodic boundary conditions can be specified by using the value on one side of the grid as the boundary value for the other side of the grid. In the case examined here, there is mirror" symmetry of the flux values along the $z = 0$ line, so the boundary condition on this side of the grid is that the first derivative of ψ with respect to z be zero. On the other three sides of

the grid, second derivative boundary conditions are used; the values of the second derivatives are approximated using second order central finite differences of ψ

In determining the accuracy of the spline coefficients, there are two factors to consider: the grid spacing and the step size of the line follower. The accuracy of the spline coefficients was checked by using a modified line following program, which computed the flux value from the coefficients at every step. The value of ψ along a field line should be constant, so if we subtract the initial value of ψ from the values computed at each step, we will be able to make an estimate of the error in the interpolation. It was found that halving the step size (doubling the work) increases the accuracy mostly near the center of the grid, and then only by about 50%. The improvement comes from the higher accuracy of the line follower with a smaller step size in regions of higher field curvature. Changing the grid spacing produces a more profound effect on the accuracy of the spline interpolation. On a square grid, reducing the grid spacing by a factor of two (the work increases by a factor of ~ 3.6 not 4 because of the boundary condition at $z = 0$) improves the accuracy by a factor of approximately twenty.

As a result of these studies of the accuracy of the spline interpolation, the flux calculation routine has been improved by scaling the step size with the minor radius. This gives the necessary accuracy near the center of the grid, but keeps the work down to a minimum in the lower curvature regions (note: although the flux values at the center of the grid will never be used by the particle following code, they are needed to accurately determine the interpolation coefficients).

The plots in Figure 4.3 were generated from the improved flux calculation routine. The horizontal axis is the length along a field line, the vertical axis is the difference between the initial ψ value and the ψ value calculated at that point. The plot on the left was done for a grid spacing of 2.5 cm, the grid used in the plot on the right has a spacing of 5 cm. The error decreases by about an order of magnitude for the smaller grid spacing.
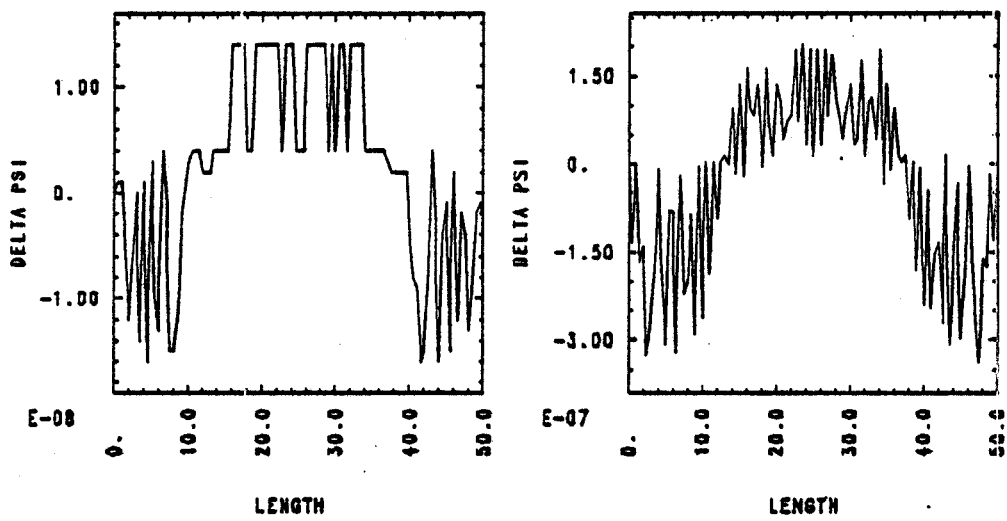
Figure 4.3: error in ψ vs. length

left: grid spacing of 2.5 cm

right: grid spacing of 5.0 cm

4.5. Particle Following

The particle following code is very similar to the field line following routine used in the flux grid calculation. A fourth order predictor–corrector algorithm is used to integrate the equations of motion. A given particle is followed for one poloidal orbit, and the difference between the final and initial values of ψ and μ, together with the poloidal period, $\Delta\tau$, are used to compute the fluxes and the Fokker–Planck coefficients.

4.5.1. The Guiding Center Equations

The equations of motion are those given in Northrop[23] with one small modification. If we do the guiding center expansion as in Northrop, we obtain:

$$\frac{du}{dt} = -\frac{\mu}{m}\underline{b}\cdot\nabla B + \underline{v}\cdot\nabla\underline{b}\cdot\underline{v} + \frac{q}{m}\underline{b}\cdot\underline{E} \tag{4.5.1}$$

$$\underline{v} = u\underline{b} + \frac{\underline{b}}{B}\times\left(-\underline{E} + \frac{\mu}{q}\nabla B + \frac{m}{q}u^2\underline{b}\cdot\nabla\underline{b}\right) \tag{4.5.2}$$

where $\underline{v}$ is the rate of change of the position vector $\underline{r}$, u is the parallel velocity, $\underline{b}$ is the unit vector parallel to the magnetic field $\underline{B}$, $B = |\underline{B}|$, $\underline{E}$ is the electric field, and q and m are the particle's charge and mass respectively. This system of equations is slightly modified to improve energy conservation. If we assume that $\underline{E} = 0$ and that μ is constant, the rate of change of the energy can be calculated.

$$H = \frac{1}{2}mu^2 + \mu B \tag{4.5.3}$$

$$\frac{dH}{dt} = mu\frac{du}{dt} + \mu\frac{dB}{dt} \tag{4.5.4}$$

where the second order term corresponding to the kinetic energy of the drift velocity has been neglected. If we assume that B is constant, substituting for $\frac{du}{dt}$ we have:

$$\frac{dH}{dt} = mu\left(-\frac{\mu}{m}\underline{b}\cdot\nabla B + \underline{v}\cdot\nabla\underline{b}\cdot\underline{v}\right) + \mu\underline{v}\cdot\nabla B \tag{4.5.5}$$

simplifying:

$$\frac{dH}{dt} = -\mu u\underline{b}\cdot\nabla B + mu\underline{v}\cdot\nabla\underline{b}\cdot\underline{v} + \mu u\underline{b}\cdot\nabla B + \mu\underline{v}_d\cdot\nabla B$$
$$= mu\underline{v}\cdot\nabla\underline{b}\cdot\underline{v} + \mu\underline{v}_d\cdot\nabla B \tag{4.5.6}$$

where $\underline{v}_d$ is the drift velocity ($\underline{v}_d = \underline{v} - u\underline{b}$). In general, these two terms do not cancel, and energy is not conserved by these equations. The "ripple" in energy is not large, but it can be reduced if the second term can be canceled out. If we assume that there is an additional piece to the $\frac{du}{dt}$ equation which cancels the second term, energy conservation yields:

$$\mu \underline{v}_d \cdot \nabla B = -mu \frac{du}{dt}\Big|_{add} \tag{4.5.7}$$

Substituting for $\underline{v}_d$, we have:

$$\frac{\mu \underline{b}}{qB} \times \left(\mu \nabla B + mu^2 \underline{b} \cdot \nabla \underline{b}\right) \cdot \nabla B = -mu \frac{du}{dt}\Big|_{add} \tag{4.5.8}$$

Because of the cross product, the first term on the left hand side gives zero, and we can solve for the correction to $\frac{du}{dt}$.

$$\frac{du}{dt}\Big|_{add} = -\frac{\mu \underline{b}}{qB} \times \left(u\underline{b} \cdot \nabla \underline{b}\right) \cdot \nabla B \tag{4.5.9}$$

Including this term in the system of guiding center equations:

$$\frac{du}{dt} = -\frac{\mu}{m} \underline{b} \cdot \nabla B + \underline{v} \cdot \nabla \underline{b} \cdot \underline{v} + \frac{q}{m} \underline{b} \cdot \underline{E} - \frac{\mu \underline{b}}{qB} \times \left(u\underline{b} \cdot \nabla \underline{b}\right) \cdot \nabla B \tag{4.5.10}$$

$$\underline{v} = u\underline{b} + \frac{\underline{b}}{B} \times \left(-\underline{E} + \frac{\mu}{q}\nabla B + \frac{m}{q}u^2 \underline{b} \cdot \nabla \underline{b}\right) \tag{4.5.11}$$

This "extra" term has a simple physical explanation. The first term of equation 4.5..10 is the change in $\frac{du}{dt}$ caused by the particle moving into a region of different magnetic field strength. This is from the *parallel* motion of the particle. The new term is similar, except that the motion is the result of the *drift* motion of the particle, specifically the curvature drift. The new term is one of the higher order terms left out in equation 4.5.10.

The importance of this additional term depends on how big the curvature drift velocity is. The important parameter here is the major radius. For our case, $R_0 = 10$ m, and this effect is small (less than 3% of the energy error), while in smaller systems this term can decrease the error by up to 40%. Figure 4.4 is a plot of the error in the energy vs. time for a 2.0 keV particle. The maximum error is about 1×10^{-4} eV. The frequency of the energy ripple is the poloidal orbital frequency. Note that this data is taken for $E_\phi = 0$; the change in energy caused by the electric field accelerating (or decelerating) the particle will be many times larger than this small ripple in the energy.

4.5.2. Description of the Code

The computer code TRACK integrates the guiding center equations for one poloidal orbit of the particle. The initial position and velocity must be specified. The initial position is specified by ψ and θ, the poloidal angle. Conversion to cylindrical coordinates (the coordinates used in the predictor–corrector integration scheme) is done using the secant method[24]. If the scattering option is specified, the scattering routine is executed after the corrector part of the integrator on each time step. Calculation of ψ at every step is done by evaluating the spline coefficients. To follow a given particle for one poloidal orbit takes on the order of 3 CRAY cpu seconds; approximately 30% of the execution time is spent in evaluating the magnetic field, which must be done twice each time step.

After one poloidal orbit has been completed, an interpolation routine (based on the Adams–Moulter polynomial implicit in the corrector step) is used to obtain the closure point of the poloidal orbit. From this final point, the changes in ψ, μ, energy and time are computed. From these quantities ω_b, ω_2, $\frac{\Delta\psi}{\Delta\tau}$ and the other quantities of interest can be calculated. The bounce averaged toroidal flux is also computed by the code. This is needed when computing the kinematic bootstrap coefficient.
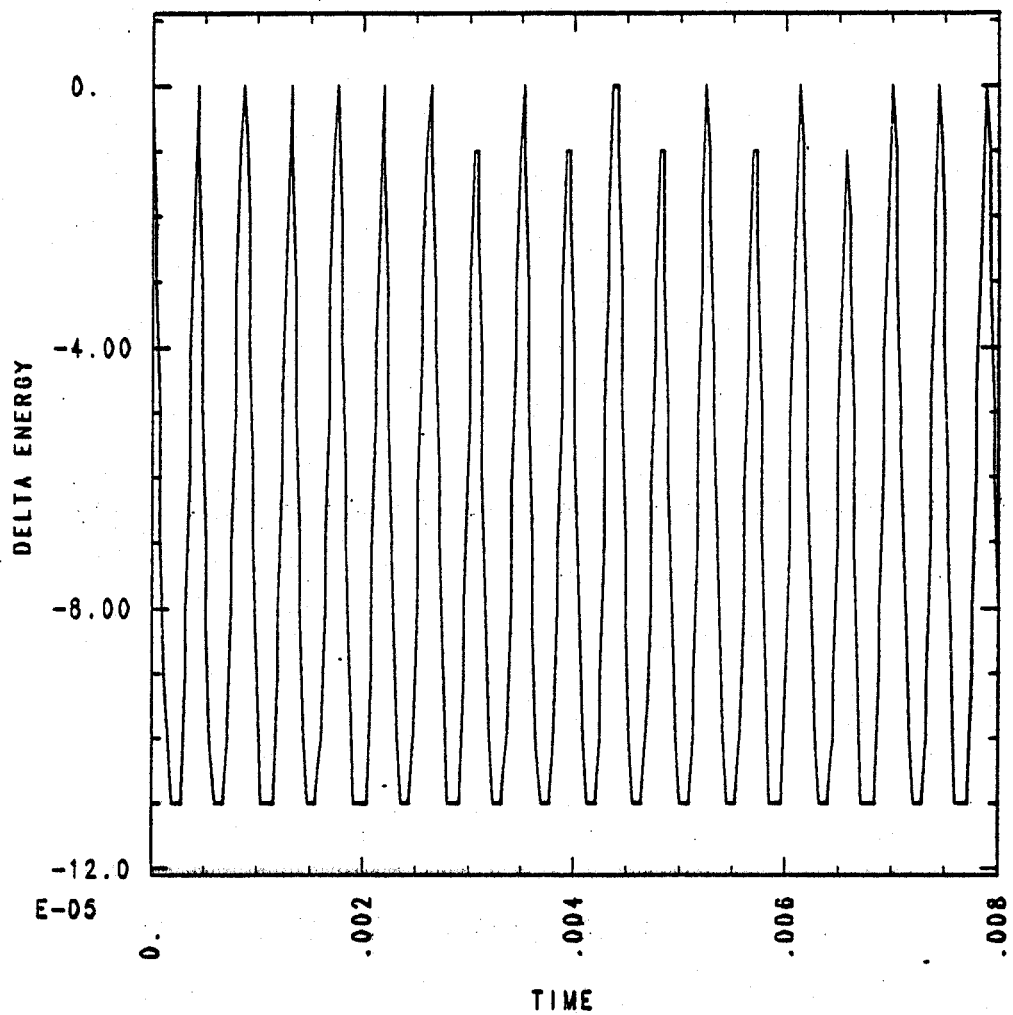
Figure 4.4: error in energy vs. time

Results and Comparison to Theory

In this chapter the results of the numerical evaluation of the transport coefficients are presented. Both the ideal banana regime and finite ν_* cases are examined and compared to the predictions of the Lagrangian formulation. In Section 5.1, the ideal and collisional behavior of $\frac{\Delta\psi}{\Delta r}$ and the explicit pinch coefficient is discussed along with the $\langle\frac{\Delta\mu\Delta\mu}{\Delta r}\rangle$ (explicit pitch angle scattering) Fokker–Planck coefficient. Section 5.2 contains the results for the explicit current; in Section 5.3, the (implicit) Fokker–Planck coefficient $\langle\frac{\Delta\mu\Delta\psi}{\Delta r}\rangle$ will be examined.

A note on the computer facilities used for these calculations: the basic computations, e.g. creation of the flux grid, field line following, particle following, were all done on the CDC 7600 and the two CRAY-1 computers at the National Magnetic Fusion Energy Computer Center at the Lawrence Livermore National Laboratory. The particle following data were then pre-processed into a condensed form, and transferred to the MIT Macsyma Consortium PDP-10 over the ARPAnet. The condensed data were then analyzed and plotted in an interactive LISP environment.

5.1. The Explicit Pinch Coefficient

In this section the behavior of the explicit pinch transport coefficients will be discussed. Using the procedures described in Chapter 4, the quantities $\frac{\Delta\psi}{\Delta r}$ and ω_b can be computed for each particle in the initial particle distribution. These data can then be used to numerically construct the function $S_{13,\epsilon}(\lambda)$, which was used in theoretical calculation of the explicit pinch transport coefficients. The quantities $\frac{\Delta\psi}{\Delta r}$ and ω_b can also be compared to the appropriately normalized theoretical expressions developed in Chapter 3.

First, consider ω_b. In Figures 5.1 and 5.2, ω_b is plotted as a function of the pitch parameter λ. The data points are denoted by squares, the solid curve is the results predicted by the ideal banana theory. These solid curves were computed from equations 3.1.3 and 3.1.5:

$$\omega_b^{circ} = C\frac{\sqrt{1+\epsilon-\lambda}}{K(m)} \qquad (5.1.1)$$

$$\omega_b^{trap} = C\sqrt{\frac{\epsilon}{2}}\frac{1}{K(m^{-1})} \qquad (5.1.2)$$

where

$$m = \frac{2\epsilon}{1+\epsilon-\lambda} \qquad (5.1.3)$$

and

$$C = \frac{1}{4R_0 q_0}\sqrt{\frac{2H}{m}} \qquad (5.1.4)$$

where R_0 is the major radius and q_0 is the value of the safety factor, obtained from Figure 4.1. Note that in the notation of Chapter 3, $m = k^2$.

Comparing the data with the predictions of the ideal theory presents a problem. Because of the toroidal geometry, ϵ is not a constant. The ϵ used in evaluating the preceding equations was derived from $\lambda = 1 - \epsilon$ at the boundary layer ($\theta = \pi$). A slightly different value of ϵ would have been obtained if we had used $\lambda = 1 + \epsilon$ for the most deeply trapped particles ($\theta = 0$). We chose the boundary layer value of ϵ because it the ideal theory predicts that ω_b should have an absolute minimum, and $\frac{\Delta\psi}{\Delta\tau}$ should be singular at the boundary, and in the data from the simulation, ω_b does have its minimum at the boundary, while $\frac{\Delta\psi}{\Delta\tau}$ reaches its maximum value there.

In Figures 5.1 and 5.2, the theoretical and actual values of ω_b are in good agreement, within 10% or so, except near the boundary layer. Near the boundary (see Figure 5.2), the agreement becomes very poor. In the ideal banana theory, it is assumed that the parallel velocity will always be greater than the drift velocity; the particles near the boundary should have little circulating motion, and thus ω_b should be approximately zero. This is not observed in the computation: the ∇B drift forces the particle in the $+\hat{z}$ direction to a lower field strength region. Conservation of μ requires the parallel energy to increase, and the particle does circulate with a non-zero ω_b.

The computed values of $\frac{\Delta\psi}{\Delta\tau}$ as a function of λ are given for the forward directed particles ($\sigma = +1$) in Figures 5.3 and 5.4. Figure 5.3 shows the entire range of λ, Figure 5.4 shows just the region of the boundary layer. The data in these plots has been normalized to the value of $\frac{\Delta\psi}{\Delta\tau}$ computed for the most deeply trapped particles. The solid lines are the predicted values from the ideal banana theory, the squares denote data from the computer simulation. Normalizing equations 3.1.11 and 3.1.12 to correspond to the sign convention of the data yields:

$$\frac{\Delta\psi}{\Delta\tau}^{trap} = -1 \qquad (5.1.5)$$

$$\frac{\Delta\psi}{\Delta\tau}^{circ} = 1 - \frac{\pi^2}{4}\frac{1+\epsilon-\lambda}{K^2(m)}\left[1 + \frac{\lambda}{1-\epsilon-\lambda}\frac{E(m)}{K(m)}\right] \qquad (5.1.6)$$

From these figures, it is apparent that at least on a qualitative basis, the predicted behavior of $\frac{\Delta\psi}{\Delta\tau}$ is observed. There are several interesting features of the $\frac{\Delta\psi}{\Delta\tau}$ spectrum which should be commented on. First, the trapped particles do not have a constant value of $\frac{\Delta\psi}{\Delta\tau}$. The reasons for this can be best examined by comparison to Ware's original work[6]. If instead of computing $\Delta\psi$ and dividing by the poloidal period, the change in minor radius is computed and the numerical analog to equation 3.1.13 can be written:

$$\frac{\Delta r}{\Delta\tau} = -\frac{E_\phi}{B_{pol}} \qquad (5.1.7)$$

where B_{pol} is the magnitude of the poloidal magnetic field. In the discussion of this equation in Section 3.1, it was pointed out that the magnitude of B_{pol} is assumed to be constant. This assumption is good, in the limit of small ϵ, or small banana width. In our model ϵ is approximately $\frac{1}{18}$, which is certainly small, but it is not zero. Thus we should expect good agreement with the expected behavior of $\frac{\Delta r}{\Delta\tau}$. Figure 5.5 gives the percent difference between $\frac{\Delta r}{\Delta\tau}$ and $-\frac{E_\phi}{B_{pol}}$ as a function of λ for the parallel directed trapped particles (the anti-parallel results are similar). The range of λ shown covers the entire trapped region; the left vertical axis corresponds to the trapped-circulating boundary. The agreement between the calculation and the prediction is extremely good for the deeply trapped particles, but the results diverge from the prediction as the trapped-circulating boundary is approached. Near the boundary, the difference is approximately 8%. The reason that the error is largest here is that the banana width is largest for these particles, so the assumption that B_{pol} is constant is not as good as it is for the deeply trapped particles.

Turning again to Figures 5.3 and 5.4, we see that the circulating particles are also in good qualitative agreement with the values predicted by equations 5.1.5 and 5.1.6. The well circulating particles have values of $\frac{\Delta\psi}{\Delta\tau}$ with the opposite sign of those near the boundary, as predicted in Chapter 3. Closer to the boundary, the data is in good agreement with predictions of the ideal theory except near the trapped-circulating boundary. The theory predicts a logarithmic singularity on the boundary, but a finite value is observed. In fact, the values of $\frac{\Delta\psi}{\Delta\tau}$ in the boundary layer show an increasing divergence from the predicted values as we approach the boundary. One source of this discrepancy is the value of E_ϕ. In the ideal theory, the limit of a zero electric field is taken. Using a finite electric field will cause drifts in energy and λ as discussed in Section 2.5. Thus a particle which starts off in the boundary layer will drift towards circulating or trapped space, depending on its value of σ. The forward directed particles will drift towards circulating space, thus $\frac{\Delta\psi}{\Delta\tau}$ will be lower than expected, while the $\sigma = -1$ particles drift toward the boundary, and have a larger than expected $\frac{\Delta\psi}{\Delta\tau}$. Figure 5.6 is a plot of normalized $\frac{\Delta\psi}{\Delta\tau}$ as a function of λ in the boundary layer, in all aspects identical to Figure 5.4 except that $E_\phi = 1.0 \times 10{-}3$ V/m instead of

0.05 V/m. As before just the $\sigma = +1$ particles are shown. comparing the two figures, we see that decreasing E_ϕ (thereby decreasing the drift in λ) increases the normalized value of $\frac{\Delta\psi}{\Delta\tau}$; for these two cases the improvement is by a factor of five.

Another cause of the discrepancy is the assumption made in the ideal theory that the parallel velocity is always larger than the drift velocity. Instead of the particle orbits in the boundary layer being only marginally circulating, they have a well defined circulating nature.

The explicit pinch transport coefficient may be calculated from the values of $\frac{\Delta\psi}{\Delta\tau}$ and ω_b. Leaving aside the question of normalization, we can write:

$$I_{13,e}^{trap} = \frac{1}{2} \int_{\lambda_{bl}}^{\lambda_{max}} \frac{1}{\omega_b} \frac{\Delta\psi}{\Delta\tau} \, d\lambda \qquad (5.1.8)$$

$$I_{13,e}^{circ} = \int_0^{\lambda_{bl}} \frac{1}{\omega_b} \frac{\Delta\psi}{\Delta\tau} \, d\lambda \qquad (5.1.9)$$

where the factor of $\frac{1}{2}$ in the trapped particle comes from the ideal theory representation of the transport coefficient (see equations 3.1.14 and 3.1.15), λ_{bl} is the value of λ at the boundary layer, and λ_{max} is the maximum value of λ allowed in phase space, it corresponds to the most deeply trapped particles. In the magnetic geometry assumed in the ideal theory, $\lambda_{bl} = 1 - \epsilon$ and $\lambda_{max} = 1 + \epsilon$; as mentioned above, the relationship $\lambda_{bl} = 1 - \epsilon$ is chosen as a means of defining the value of ϵ. The expressions derived in Chapter 3 can be modified to calculate the theoretical predictions of the transport coefficients, allowing for the variation in ϵ. Starting with equations 3.1.18 and 3.1.19, we have:

$$I_{13,e}^{trap} = \frac{2}{3} \int_{\lambda_{bl}}^{\lambda_{max}} S_{13,e}(\lambda)^{trap} \, d\lambda \qquad (5.1.10)$$

$$I_{13,e}^{circ} = \frac{2}{3} \int_0^{\lambda_{bl}} S_{13,e}(\lambda)^{circ} \, d\lambda \qquad (5.1.11)$$

where the functions $S_{13,e}(\lambda)$ are defined in equations 3.1.6 and 3.1.8. Substituting in for $S_{13,e}(\lambda)^{trap}$:

$$\begin{aligned} I_{13,e}^{trap} &= \frac{8\sqrt{2\epsilon}}{3\pi} \int_{\sqrt{\alpha}}^1 k' K(k') \, dk' \\ &= \frac{8\sqrt{2\epsilon}}{3\pi}(1 - E(\alpha) + (1 - \alpha)K(\alpha)) \end{aligned} \qquad (5.1.12)$$

where

$$(k')^2 = \frac{1 + \epsilon - \lambda}{2\epsilon} \qquad (5.1.13)$$

and

$$\alpha = \frac{1 + \epsilon - \lambda_{max}}{2\epsilon} \qquad (5.1.14)$$

The inclusion of the extra term which depends on α decreases $I_{13,\epsilon}^{trap}$ by approximately 1% over the value computed in Chapter 3. The circulating particle equation is just a modified form of equation 3.1.31:

$$I_{13,\epsilon}^{circ} = \frac{8\sqrt{2\epsilon}}{3\pi}\left(\frac{E(\beta)}{\sqrt{\beta}} - 1\right) - \frac{2\pi\sqrt{2\epsilon}}{3}\left(\frac{1 + \epsilon - \frac{2\epsilon}{\beta}}{\sqrt{\beta}K(\beta)} + 6\epsilon\int_{\sqrt{\beta}}^{1}\frac{dk}{k^4 K(k)}\right) \qquad (5.1.15)$$

where

$$k^2 = \frac{2\epsilon}{1 + \epsilon - \lambda} \qquad (5.1.16)$$

and

$$\beta = \frac{2\epsilon}{1 + \epsilon} \qquad (5.1.17)$$

i.e. β corresponds to k^2 at the lower λ limit of integration. Changing this lower limit will allow calculation of the contribution of just the boundary layer particles to the circulating pinch transport coefficient. Evaluating the two expressions for $I_{13,\epsilon}$ we find that the circulating pinch coefficient cancels 95% of the trapped pinch coefficient. 87% of the cancellation is due to the boundary layer particles, where the boundary layer has been rather arbitrarily defined to encompass all particles within $\Delta\lambda = 0.038$ of λ_{bl}. This value of $\Delta\lambda$ was chosen because both $\frac{\Delta\psi}{\Delta\tau}$ and ω_b start to exhibit the characteristics of boundary layer particles as opposed to well circulating particles at this point in λ-space.

When the transport coefficients are computed from the data, it is found that the circulating particle contribution cancels only 62% of the trapped particle coefficient. The boundary layer particles account for 53% of the cancellation. Comparison of these results to the predictions of the ideal theory given above, indicates that the problem lies mostly the boundary layer contribution. However, we have seen in the behavior of $\frac{\Delta\psi}{\Delta\tau}$ and ω_b that there are factors influencing the particle motion in the boundary layer, which are not included in the ideal banana theory. Such factors include: the toroidal electric field, which can cause drifts in λ and transitions of particles between the trapped and circulating states; toroidal geometry, which together with the electric field causes a dependence on σ; and the realistic field model, which produces the small, but non-zero drift motion (neglected in the ideal theory) that allows particles launched at λ_{bl} to have a non-zero ω_b.

A simple calculation can give some idea of the effect of the drift motion and finite electric field on the numerical results. The assumption that the drift motion is negligible is invalid within $\Delta\lambda \sim 1.0 \times 10^{-3}$ of λ_{bl}. The electric field causes a drift in the λ values of the boundary layer

particles of approximately $\Delta\lambda \sim 3.0 \times 10^{-3}$. If we vary $\Delta\lambda$ between 1.0×10^{-4} and 1.0×10^{-2}, we find that the ideal theory predicts that the contribution of these particles is between 0.45 and 0.77 respectively (the trapped particle pinch coefficient is -1.00). The numerical results for this region give a pinch coefficient of between 0.02 and 0.33 respectively. The difference of approximately 0.45 between the prediction of the ideal theory and the numerical result for the particles in the narrow region $\Delta\lambda = 1.0 \times 10^{-3}$, is to first order the difference between the computed circulating pinch coefficient and the predicted result.

Thus far only the non-collisional behavior of $\frac{\Delta\psi}{\Delta r}$ and the explicit pinch coefficients has been examined. The numerical simulation and transport coefficient calculation was done for several different scattering frequencies. The dimensionless collision frequency ν_* is defined by:

$$\nu_* = \frac{\nu}{\omega_{b0}(2\epsilon)^{\frac{1}{2}}} \tag{5.1.18}$$

where ν is the scattering frequency and ω_{b0} is the circulation frequency for the well circulating ($\lambda = 0$) particles. Substituting the actual values of ϵ and ω_{b0}:

$$\nu_* \simeq 4 \times 10^{-3} \, \nu \tag{5.1.19}$$

Computing the transport coefficients was done in the same manner as for the ideal case except that $\langle\frac{\Delta\psi}{\Delta r}\rangle$ was used in place of $\frac{\Delta\psi}{\Delta r}$ in equations 5.1.10 and 5.1.11. The results of the calculations is summarized in Table 5.1. The results have been normalized to the absolute value of the ideal trapped particle coefficient. The column labeled "b.l." is the transport coefficient from a small region near the boundary layer, the lower limit of which was defined above. The boundary layer contribution is included in the total circulating particle transport coefficient. For each non-zero value of ν_* an error estimate is included. This is based on the estimated statistical error discussed in Section 2.6.

As ν_* increases, the boundary layer contribution to the kinematic pinch coefficient decreases. The trapped particles are unaffected by these scattering levels, so the result is that as ν_* increases, the net inward flow of particles also increases. Comparison of the boundary layer and total circulating particle data shows that, within statistical error, all of decrease in the circulating particle transport coefficient is due to modification of the boundary layer particle dynamics by scattering. This can be seen in Figure 5.7, where the values of $\langle\frac{\Delta\psi}{\Delta r}\rangle$ for several values of ν_* are plotted against λ ($\frac{\Delta\psi}{\Delta r}$ vs. λ is included for comparison). Increasing ν_* drastically reduces $\langle\frac{\Delta\psi}{\Delta r}\rangle$ for those particles near the boundary.

Table 5.1			
normalized pinch transport coefficients			
ν_*	b.l.	circ	trap
0.0	0.528	0.622	−1.000
2.0×10^{-7}	0.520 ± 0.001	0.624 ± 0.002	-1.001 ± 0.001
4.0×10^{-7}	0.518 ± 0.001	0.612 ± 0.002	-1.000 ± 0.002
2.0×10^{-6}	0.507 ± 0.003	0.600 ± 0.004	-1.002 ± 0.004
4.0×10^{-6}	0.500 ± 0.004	0.594 ± 0.006	-1.000 ± 0.005
2.0×10^{-5}	0.479 ± 0.008	0.575 ± 0.013	-0.997 ± 0.012
4.0×10^{-5}	0.460 ± 0.010	0.551 ± 0.018	-0.998 ± 0.016
2.0×10^{-4}	0.400 ± 0.021	0.493 ± 0.038	-1.013 ± 0.035
4.0×10^{-4}	0.352 ± 0.028	0.452 ± 0.053	-1.023 ± 0.050
8.0×10^{-4}	0.339 ± 0.031	0.422 ± 0.060	-1.001 ± 0.066

The predicted values of $T_{13,e}^{circ}$ as a function of ν_* are computed from the expressions given in Section 3.1. Normalizing the prediction to the value of $T_{13,e}^{trap}$, we have:

$$T_{13,e}^{circ} = 1 - \frac{\pi^2}{\log\left(\frac{256}{\nu_*}\right)} \tag{5.1.20}$$

The circulating particle data from Table 5.1 are plotted as a function of ν_* in Figure 5.8. The solid line is the prediction of equation 5.1.20. The data from the numerical calculation show the predicted behavior as a function of ν_*, but the data are not in good quantitative agreement with equation 5.1.20. Qualitatively, the disagreement between the finite ν_* theory and the numerical computation can be explained in terms of the particle orbits in the boundary layer. In both the ideal banana theory and the finite ν_* theory the assumption that the parallel velocity is always greater than the drift velocity is made. The drift velocity is not completely neglected – it accounts for the finite width of the particle orbits – but it is not included in the time weighting of the orbits. This assumption breaks down for the boundary layer particles; instead of being marginally circulating, they have a well defined circulating nature as we have seen when comparing the $\nu_* = 0$ data to the ideal theory.

This circulating behavior of the boundary layer particles is also important for the finite ν_* cases. The effect of the drift motion on the particle orbits means that the boundary layer particles are more "robust" than the finite collisionality theory predicts, i.e. the orbits are less susceptible to the effects of scattering than predicted. Because the boundary layer particles make the dominant contribution to the circulating particle pinch coefficient, this implies that the circulating pinch coefficient should be larger than predicted. This is clearly shown in Figure 5.8. Scattering does not disrupt the boundary layer by the amount predicted by the finite collisionality theory.

Another way of looking at the problem is that scattering is less effective than predicted in the finite ν_* theory. Given a value of ν from the Monte Carlo calculations, we can simulate the "robustness" of the boundary layer particles by reducing the numerical factor which relates ν and ν_* in equation 5.1.19.

$$\nu'_* = 2.0 \times 10^{-5}\, \nu \tag{5.1.21}$$

In Table 5.2, the values of the explicit circulating particle pinch coefficient are given. The results from the numerical simulation are given in the column marked "data". The predicted value of the pinch coefficient is given in the column labeled "$T_{13,c}$" and the value obtained using ν'_* is in the column marked "$T'_{13,c}$."

Table 5.2					
circulating pinch coefficients					
ν	data	ν_*	$T_{13,c}$	ν'_*	$T'_{13,c}$
0.0	0.622	0.0	1.000	0.0	1.000
5.0×10^{-5}	0.624 ± 0.002	2.0×10^{-7}	0.529	1.0×10^{-9}	0.624
1.0×10^{-4}	0.612 ± 0.002	4.0×10^{-7}	0.513	2.0×10^{-9}	0.614
5.0×10^{-4}	0.600 ± 0.004	2.0×10^{-6}	0.471	1.0×10^{-8}	0.588
1.0×10^{-3}	0.594 ± 0.006	4.0×10^{-6}	0.451	2.0×10^{-8}	0.576
5.0×10^{-3}	0.575 ± 0.013	2.0×10^{-5}	0.397	1.0×10^{-7}	0.544
0.01	0.551 ± 0.018	4.0×10^{-5}	0.370	2.0×10^{-7}	0.529
0.05	0.493 ± 0.038	2.0×10^{-4}	0.298	1.0×10^{-6}	0.490
0.1	0.452 ± 0.053	4.0×10^{-4}	0.262	2.0×10^{-6}	0.471
0.2	0.422 ± 0.060	8.0×10^{-4}	0.221	4.0×10^{-6}	0.451

From the table, we see that if the reduced value, ν'_*, gives a good fit to the data. The dashed line in Figure 5.8 represents equation 5.1.20 with ν'_* used instead of ν_*.

As a check on the scattering model, the Fokker–Planck coefficient $\langle \frac{\Delta\mu\Delta\mu}{\Delta\tau} \rangle$ was computed for three values of ν_*. The normalized results (the normalization is a division by ν_*) are given in Figures 5.9 and 5.10. The solid line represents the prediction of the Lagrangian formulation[7], which can be expressed as:

$$\left\langle \frac{\Delta\mu\Delta\mu}{\Delta\tau} \right\rangle = c\lambda\omega_2 J \tag{5.1.22}$$

where c is some normalization constant determined from the data and J is the parallel invariant, which is given for the circulating particles by the expression[7]:

$$J \sim \sqrt{1 + \epsilon - \lambda}\, E(m) \tag{5.1.23}$$

where m has been previously defined. The data are in good agreement with the prediction over most of the circulating region of λ-space. At the boundary layer, there is a disagreement, due to the prediction of the ideal theory that $\omega_2 = 0$ at $\lambda = \lambda_{bl}$. If we consider Figure 5.10, there is a more serious anomaly present. In the finite ν_* theory, it is expected that ω_2 for the boundary layer particles should increase as ν_* increases, due to the scattering of the marginally circulating particles towards well circulating values of λ. This would give rise to an increase in $\langle \frac{\Delta\mu\Delta\mu}{\Delta\tau} \rangle$ in the boundary layer. In Figure 5.10, we see that the increase of ν_* does not produce a change in $\langle \frac{\Delta\mu\Delta\mu}{\Delta\tau} \rangle$, within the statistical error of the computation.

The values of ω_2 at $\lambda = \lambda_{bl}$ are plotted as a function of ν_* in Figure 5.11. From the data, it is apparent that there is no strong dependence of ω_2 on ν_*, contrary to the prediction of the finite collisionality theory. There is a simple physical model for the observed values of ω_2. If we consider the behavior of the boundary layer particles for the smaller values of ν_*, we see that ω_2 is dominated by those particles which scatter into trapped space. This is apparent because $\omega_2 < \omega_b$. It is difficult for a boundary layer particle to become trapped because of the low value of ν_*, but once the particle crosses the boundary, it will remain in trapped space until it scatters out, which is also difficult. Thus a small fraction of particles becomes trapped, but these remain in trapped space for a relatively long period of time. For higher values of ν_*, scattering across the boundary becomes easier. More particles will enter trapped space, but it will be easier for them to return to circulating space. So the fraction of particles which make the transition increases, but the average length of time spent in trapped space decreases. Because the two factors (fraction of particles which cross the boundary and length of time spent in trapped space) tend to offset each other as ν_* is changed, ω_2 is not strongly dependent on ν_*.

Figure 5.1: ω_b vs. λ
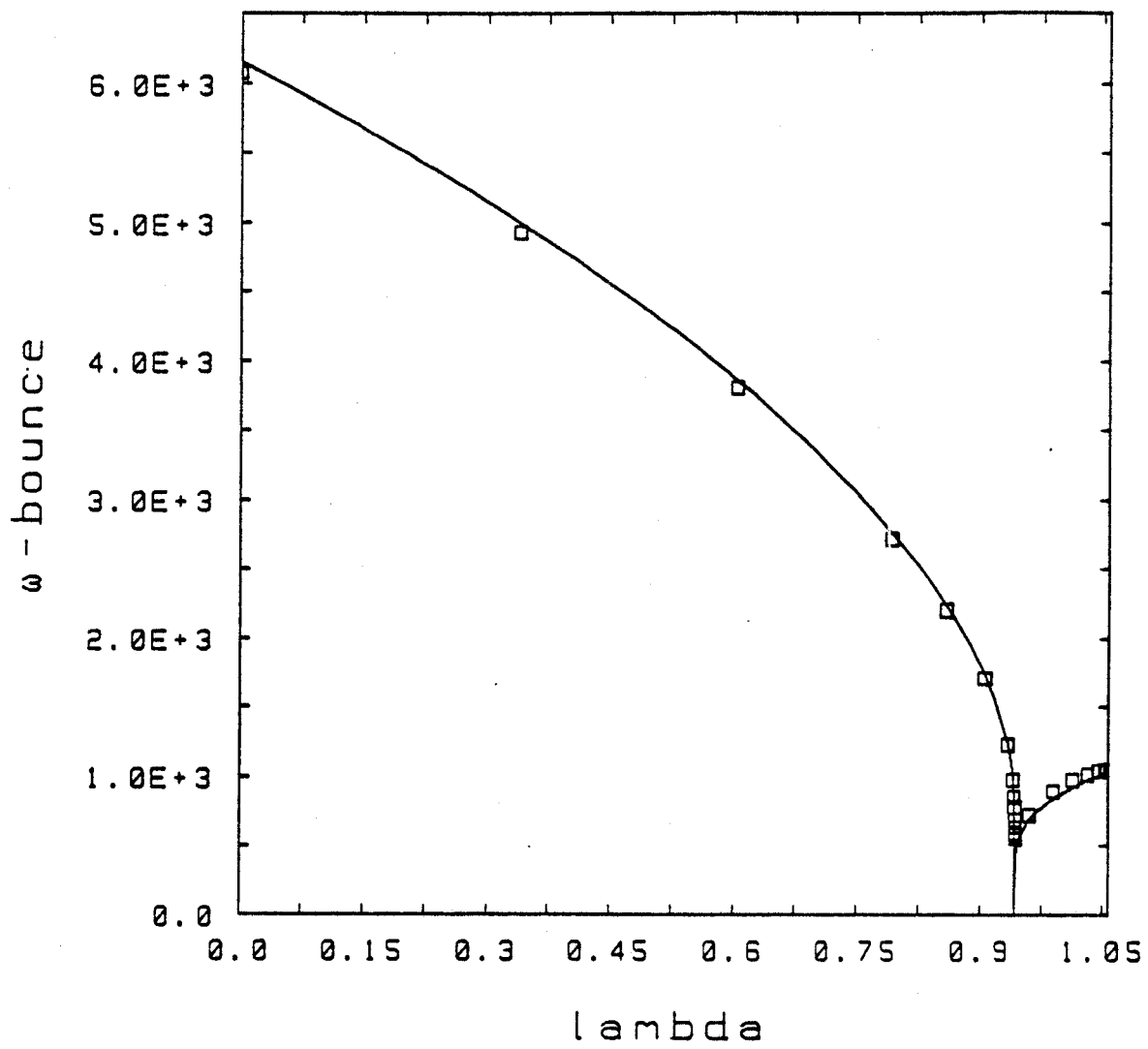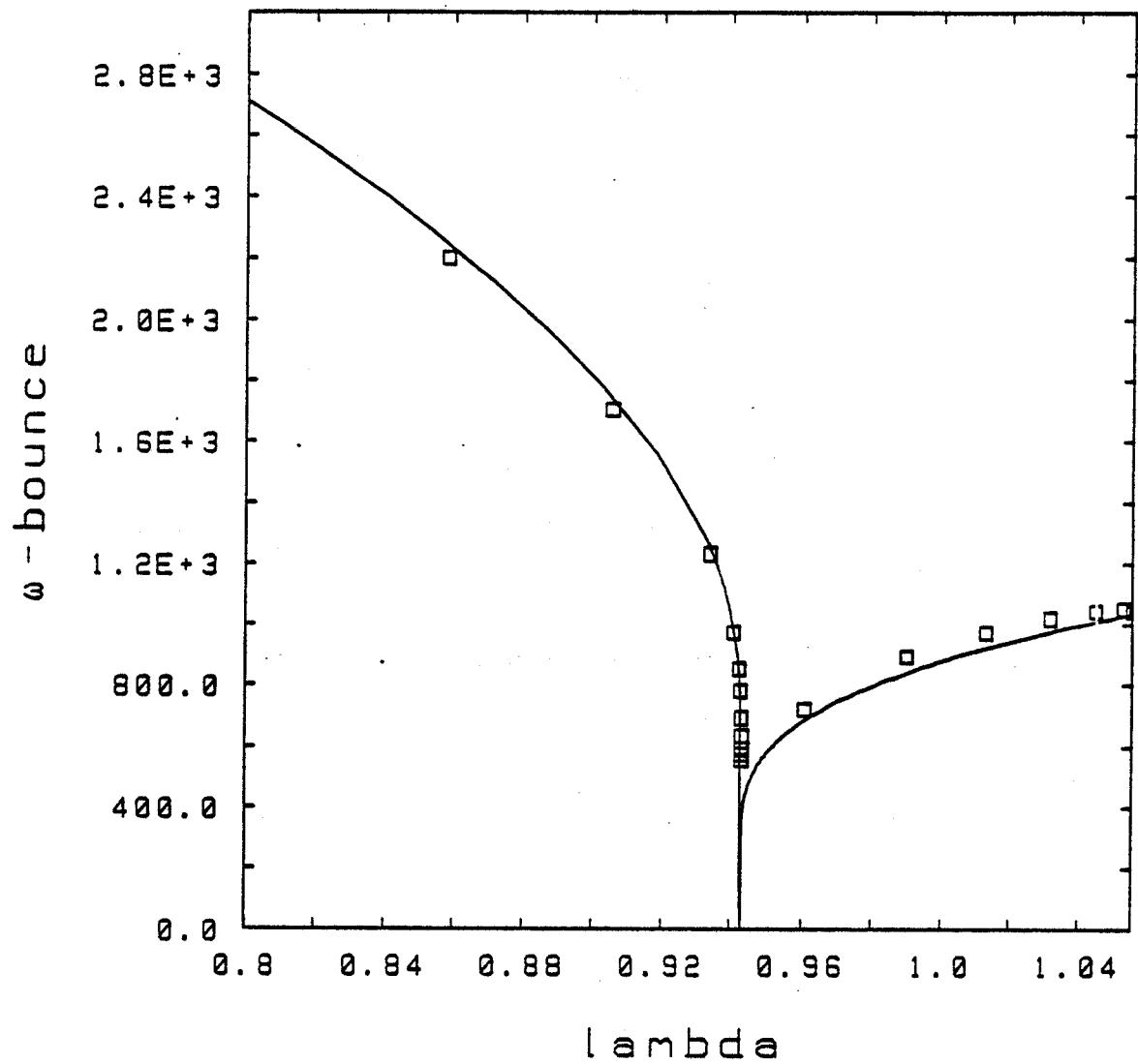
Figure 5.2: ω_b vs. λ
region near boundary
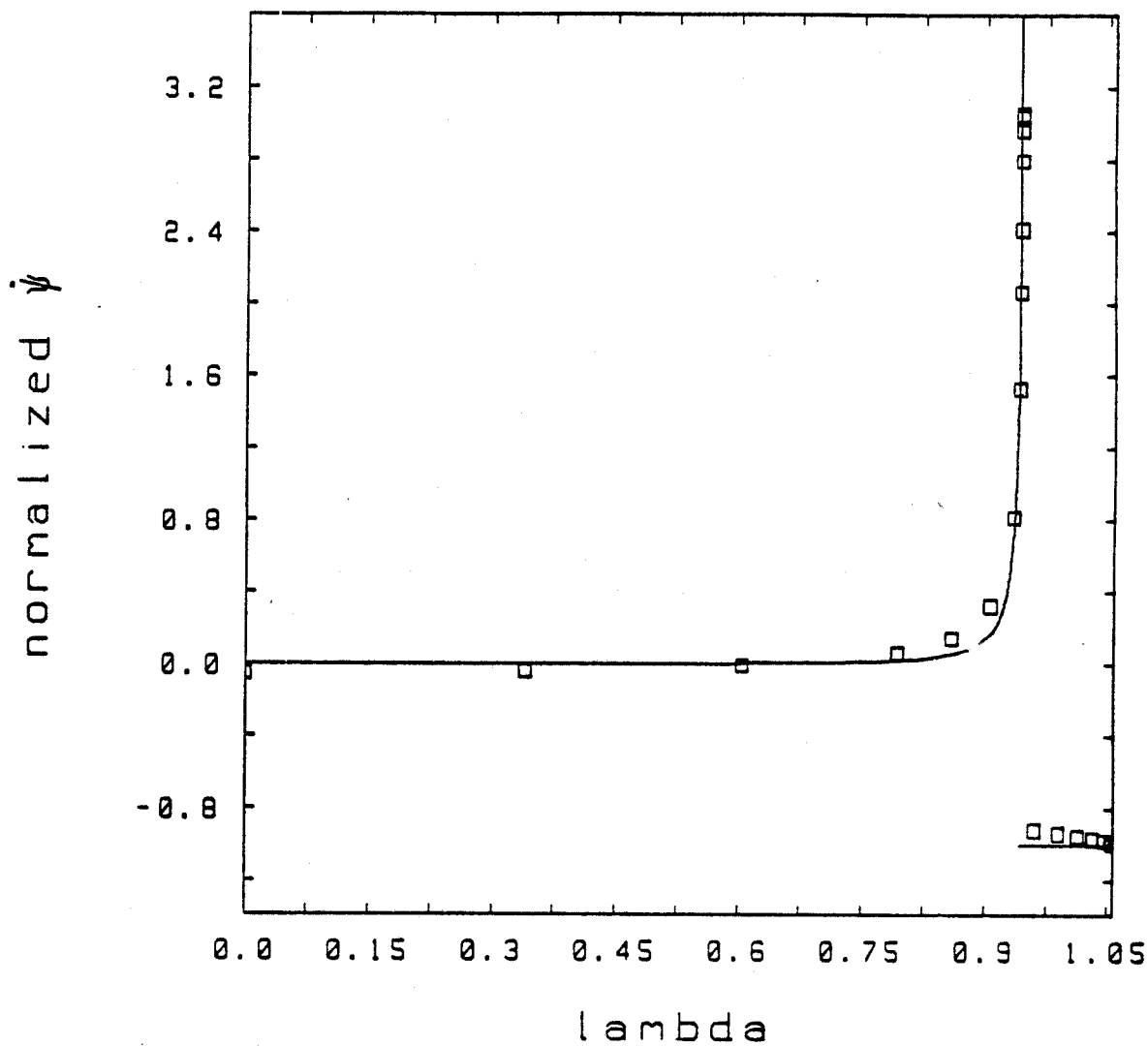
Figure 5.3: normalized $\frac{\Delta \psi}{\Delta \tau}$ vs. λ, $\sigma = +1$
$E_\phi = 0.05$ V/m
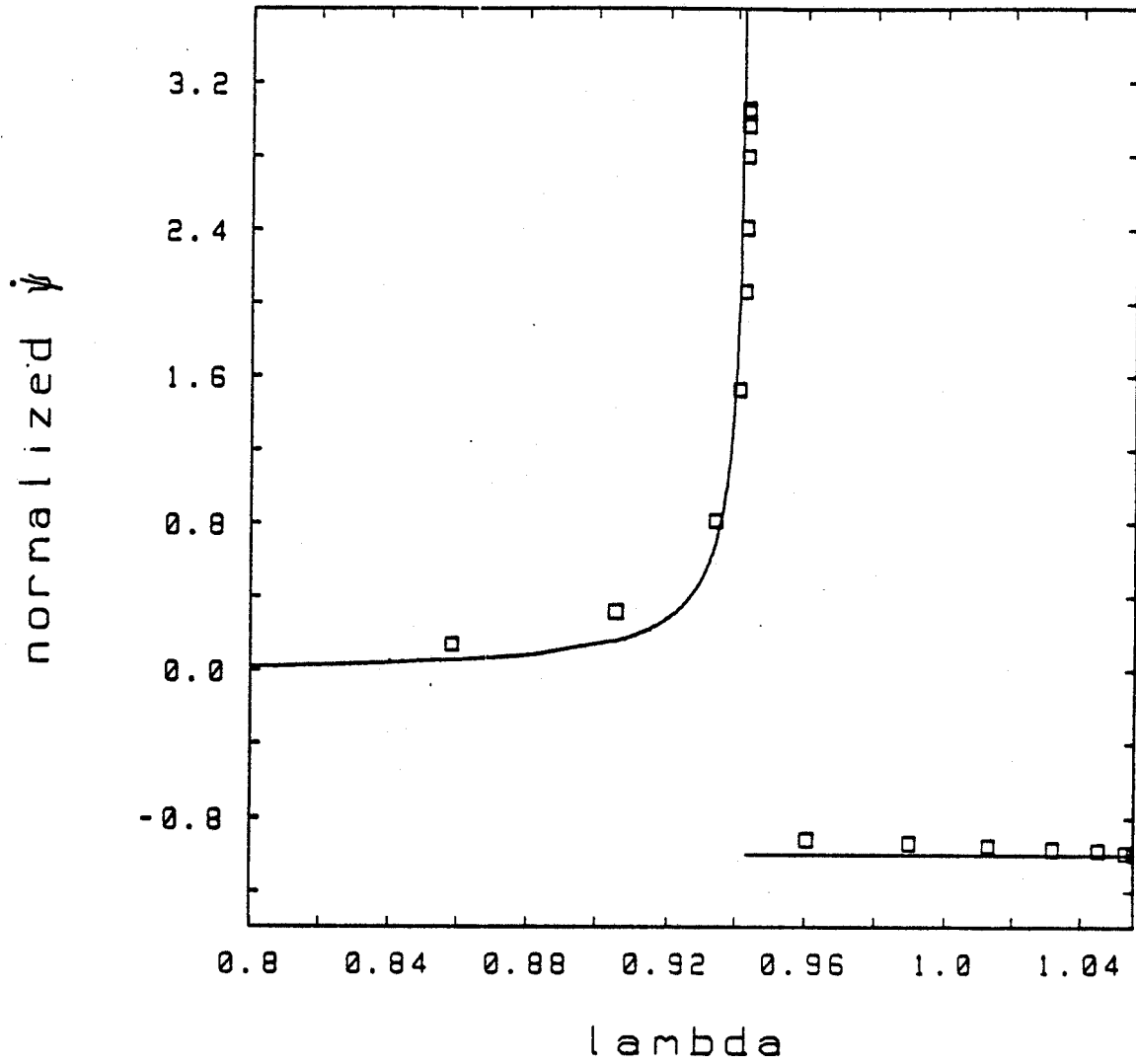
Figure 5.4: normalized $\frac{\Delta\psi}{\Delta r}$ vs. λ, $\sigma = +1$

region near boundary
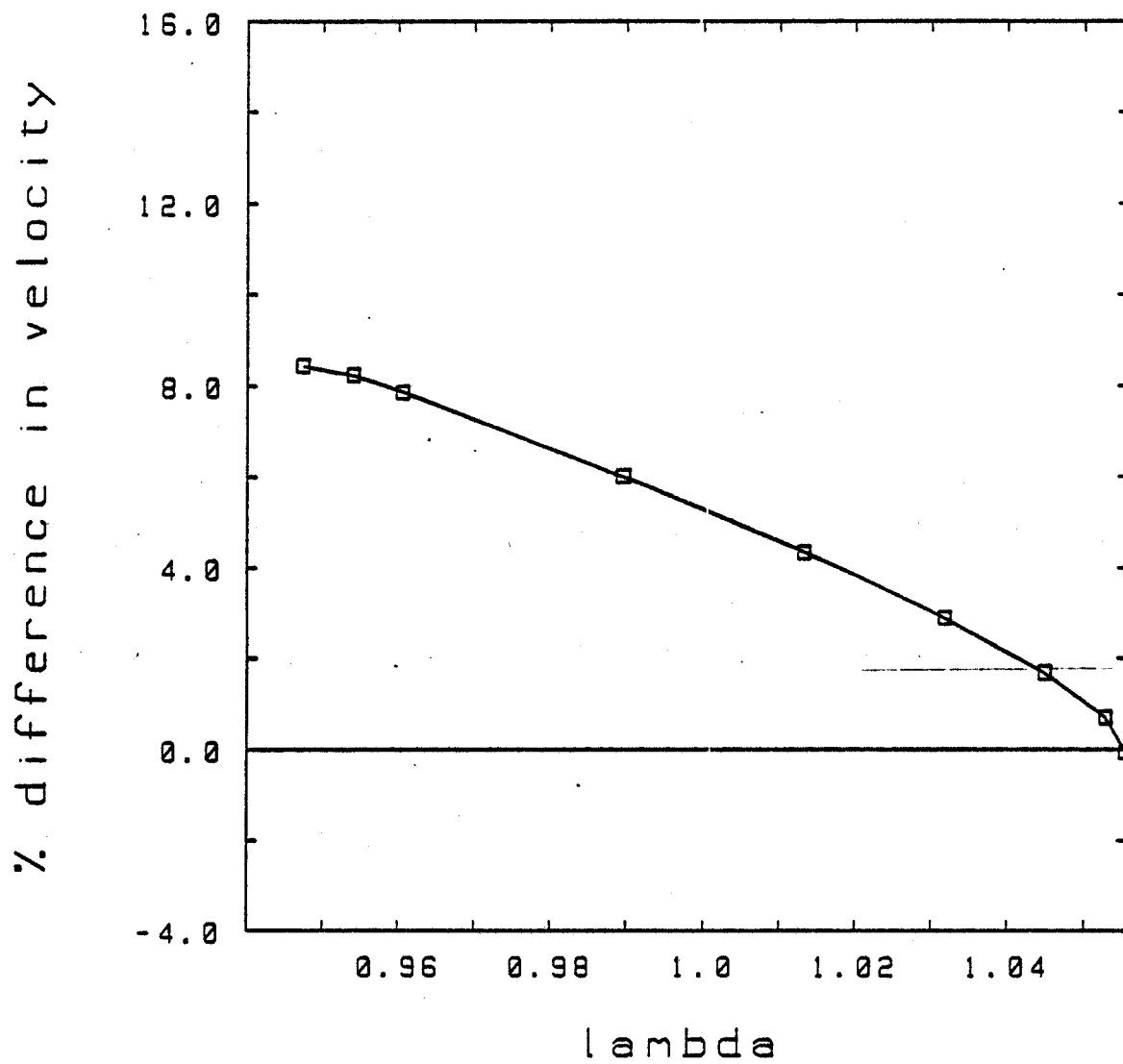
$E_\phi = 0.05$ V/m

Figure 5.5: trapped particle pinch velocity *vs.* λ
computed data points denoted by squares
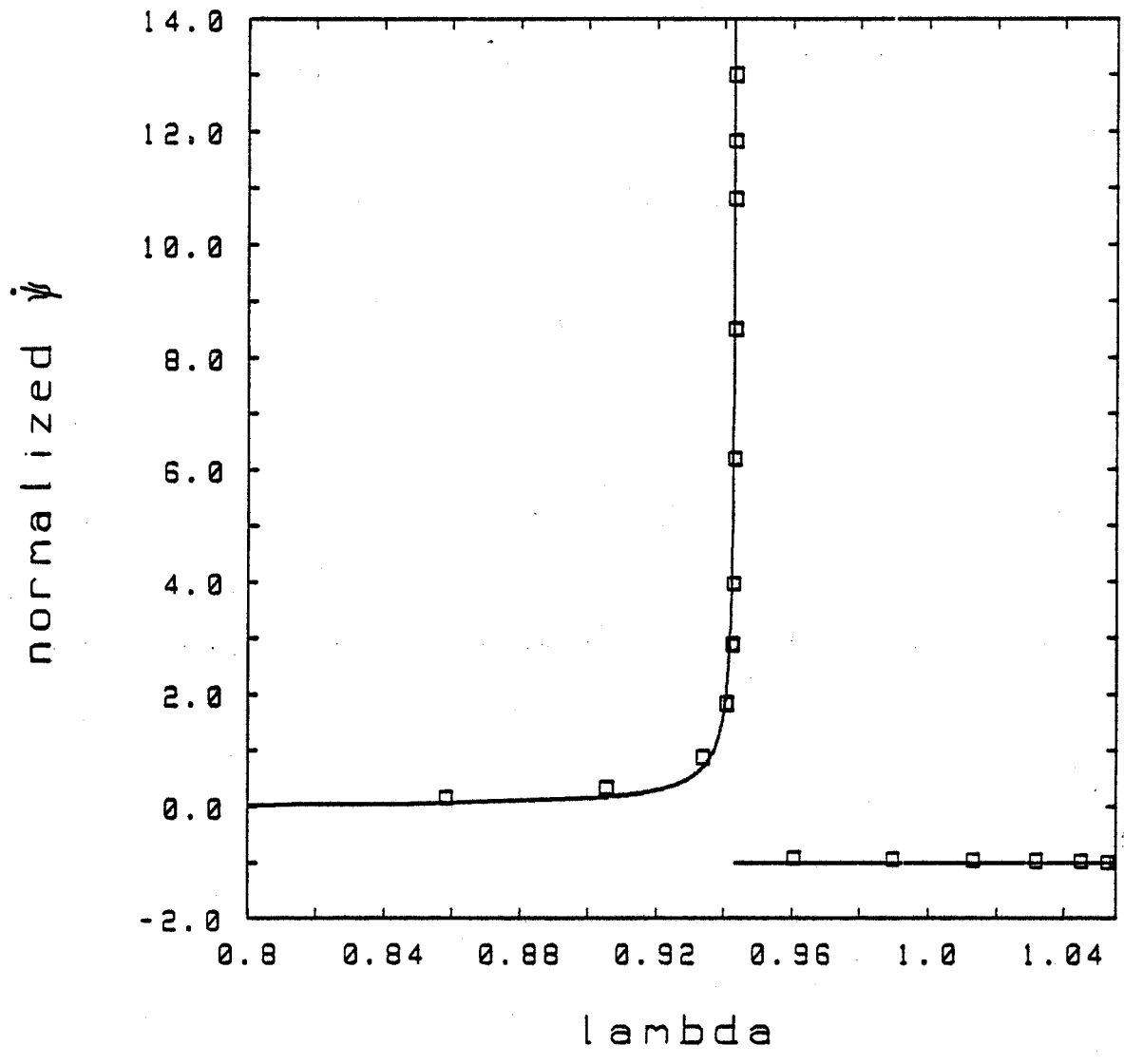
Figure 5.6: normalized $\frac{\Delta \psi}{\Delta \tau}$ vs. λ, $\sigma = +1$

$E_\phi = 1.0 \times 10^{-3}$ V/m

region near boundary
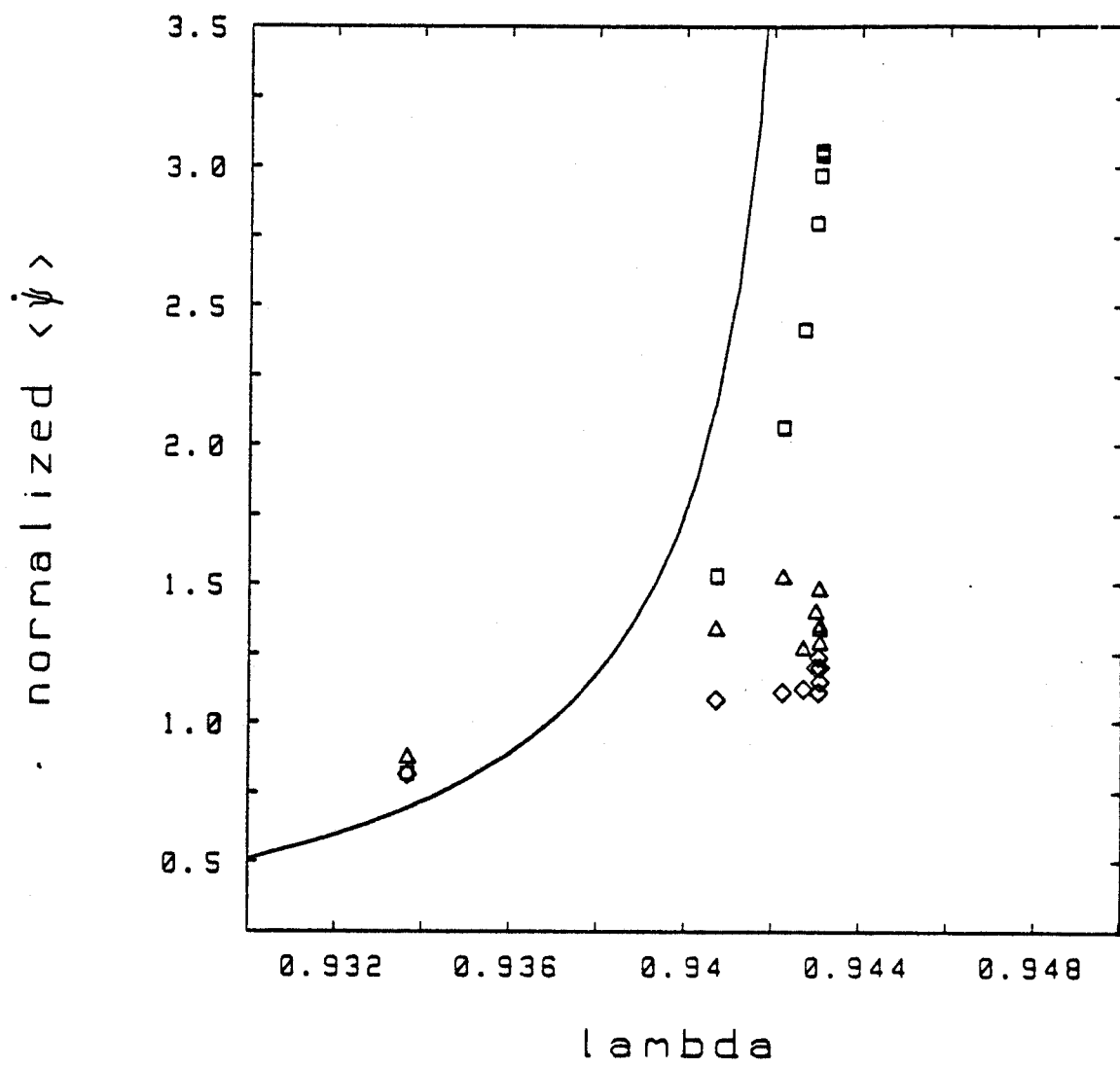
Figure 5.7: normalized $\langle \frac{\Delta \psi}{\Delta r} \rangle$ vs λ

region near boundary, $E_\phi = 0.05$ V/m

squares denote $\nu_* = 0.0$

triangles denote $\nu_* = 2.0 \times 10^{-4}$

rhombi denote $\nu_* = 4.0 \times 10^{-4}$
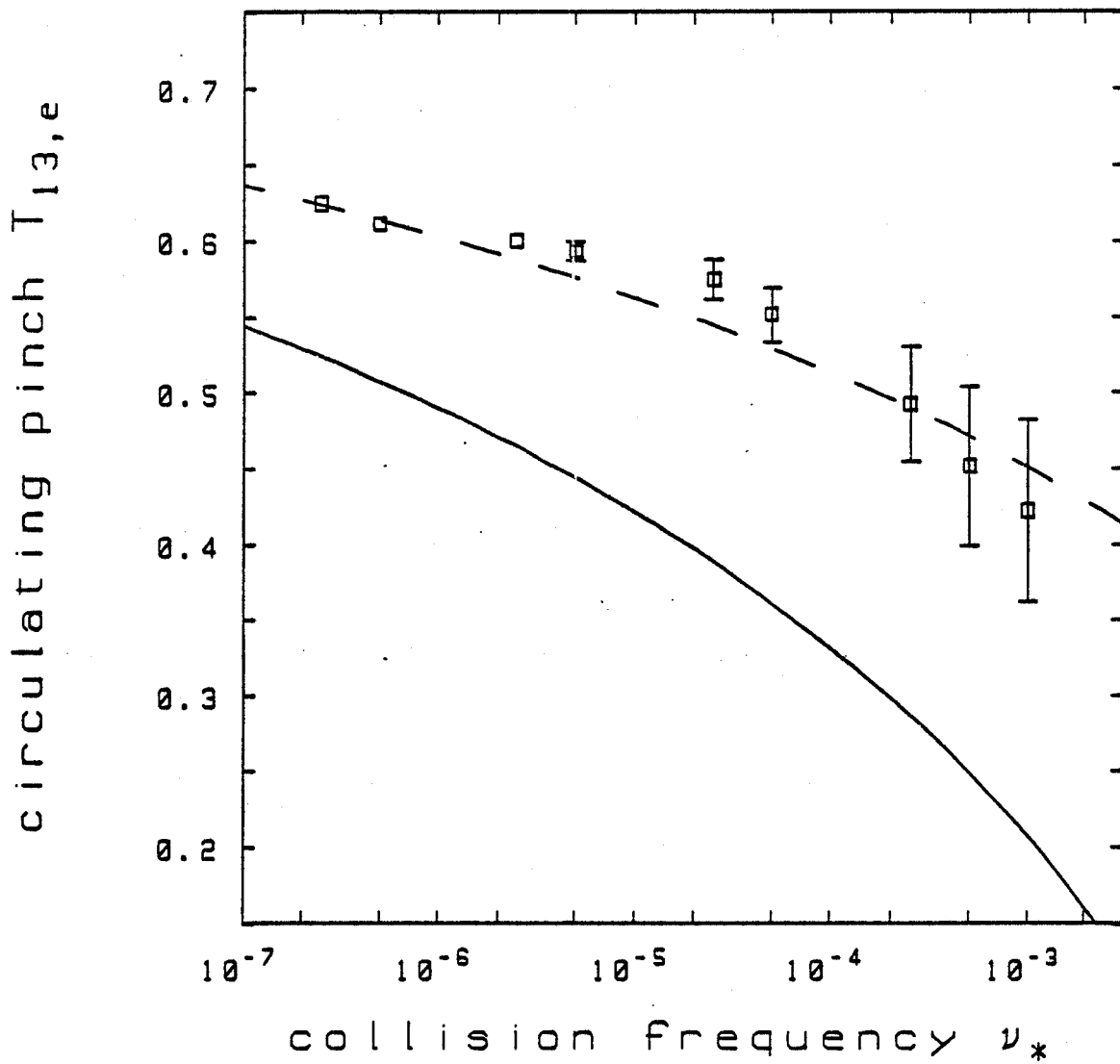
Figure 5.8: circulating pinch coefficient vs. ν_*
squares denote numerical data
solid line denotes prediction of finite ν_* theory
dashed line denotes ν'_* fit to data
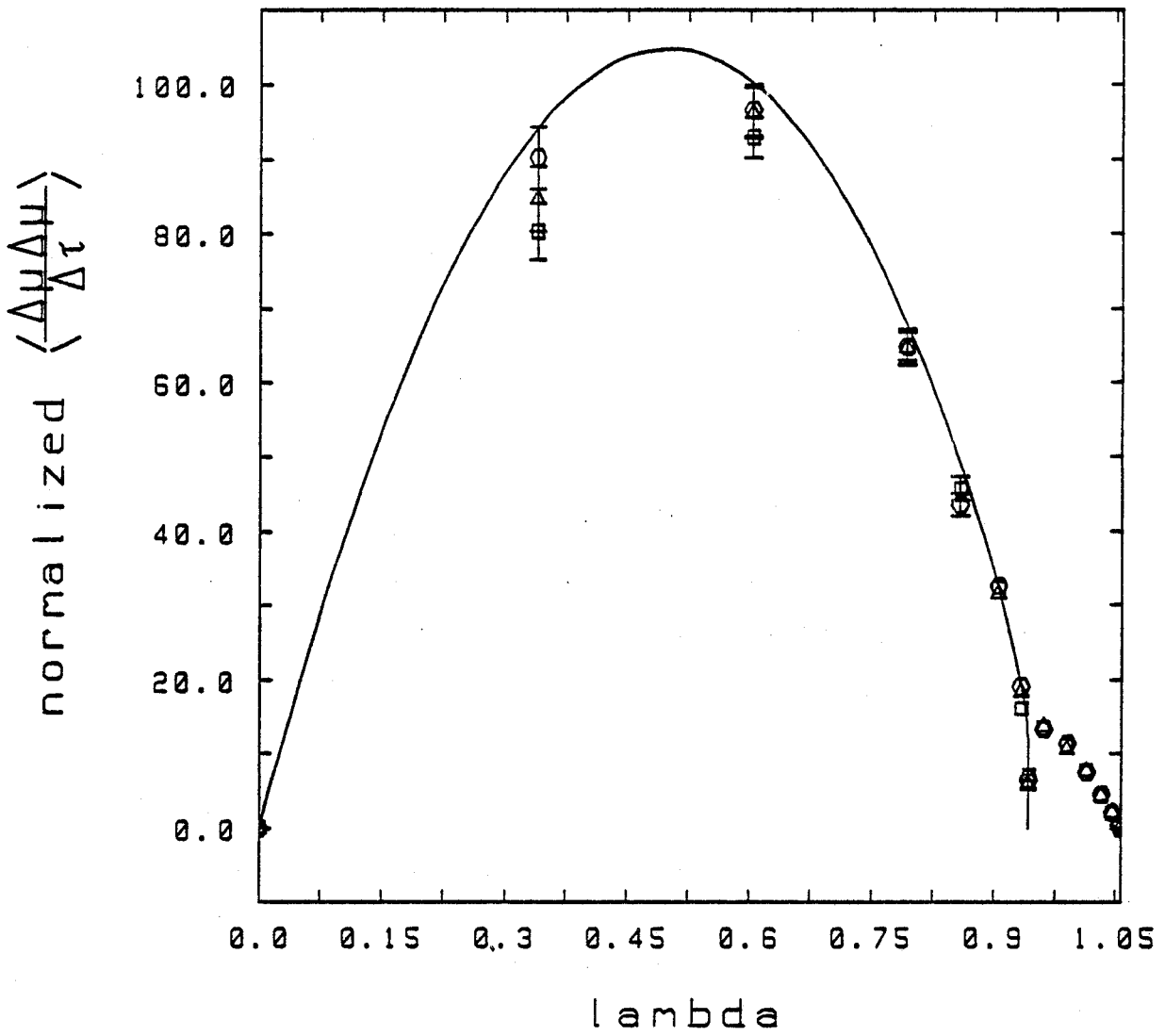
Figure 5.9: normalized $\langle \frac{\Delta\mu\Delta\mu}{\Delta\tau} \rangle$ vs. λ

squares denote $\nu_* = 8.0 \times 10^{-4}$

hexagons denote $\nu_* = 2.0 \times 10^{-5}$

triangles denote $\nu_* = 2.0 \times 10^{-6}$
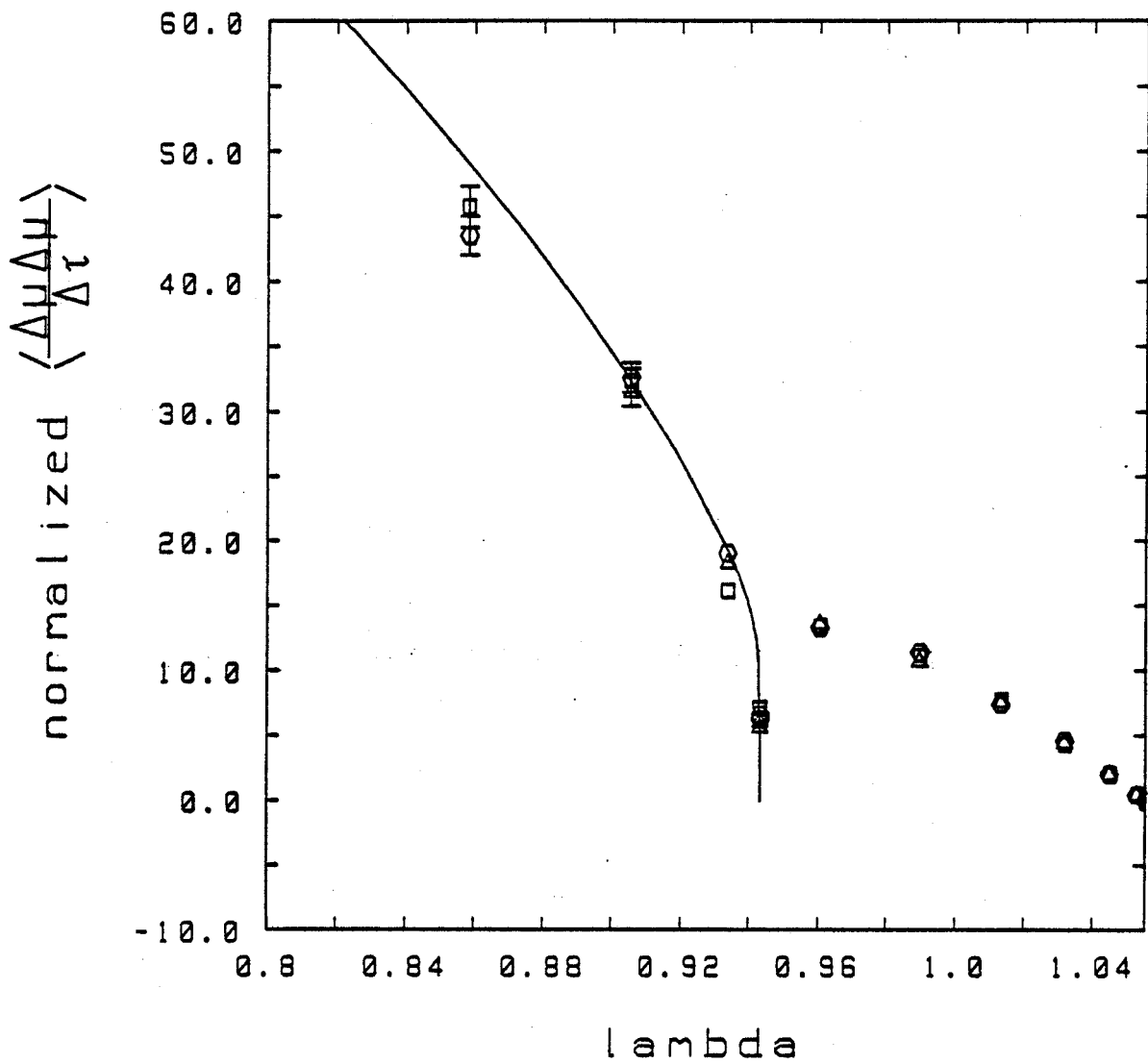
Figure 5.10 normalized $\langle \frac{\Delta \mu \Delta \mu}{\Delta \tau} \rangle$ vs. λ

region near boundary

squares denote $\nu_* = 8.0 \times 10^{-4}$

hexagons denote $\nu_* = 2.0 \times 10^{-5}$

triangles denote $\nu_* = 2.0 \times 10^{-6}$
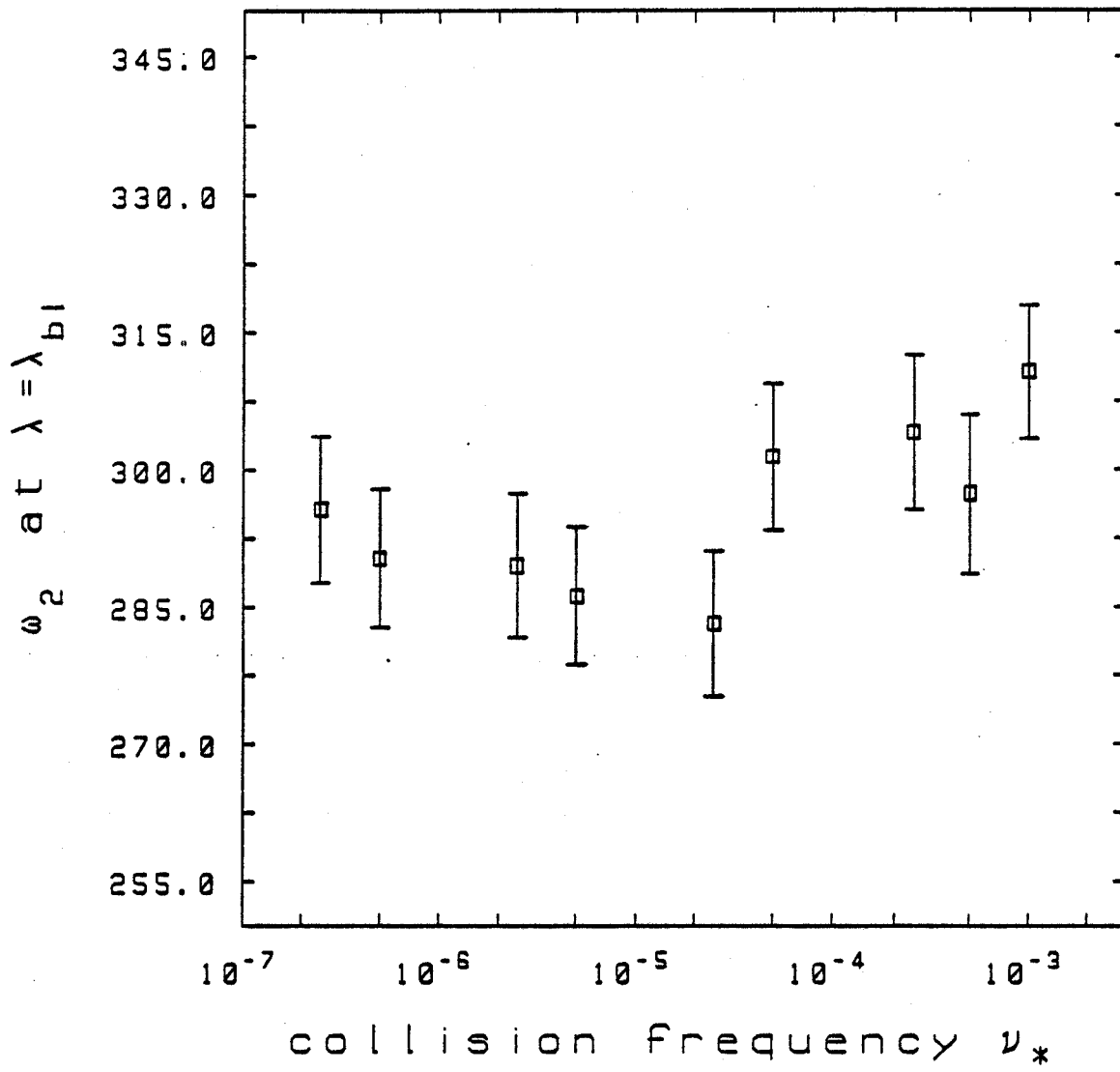
Figure 5.11 circulation frequency *vs.* ν_*
boundary layer particles

5.2. The Explicit Currents

In this section the results of the numerical calculation of the explicit currents will be presented. The explicit currents were calculated by integrating the expression:

$$S_{31,e}(\lambda) = q \oint v_\phi n(\psi)(\overline{\psi} - \psi)\, dt \qquad (5.2.1)$$

where q is the particle charge, $n(\psi)$ is the plasma density (see Section 4.3) and the integration path is the toroidal projection of the particle's trajectory. In Chapter 3, it was shown that the functions $S_{13,e}(\lambda)$ and $S_{31,e}(\lambda)$ are the product of the bounce period (ω_b^{-1}) and $\frac{\Delta\psi}{\Delta r}$ for example. Because we must integrate with respect to time in equation 5.2.1 (hence the bounce period is already included in the result), computation of the explicit current analog to $\frac{\Delta\psi}{\Delta r}$ is impossible. $S_{31,e}(\lambda)$ is a natural result of the computation. We have not mentioned the units that the quantity $S_{31,e}(\lambda)$ is expressed in because we will be comparing the data from the numerical simulation to scaled versions of the predicted functional forms $S_{31,e}(\lambda)^{circ}$ and $S_{31,e}(\lambda)^{trap}$ given in Section 3.2.

The explicit current data are plotted in Figures 5.12 and 5.13. The data are denoted by squares, the solid line represents equations 3.2.3 and 3.2.4. These equations were normalized to the value obtained at the point in trapped space nearest the boundary layer. The figures show that the agreement between the data and the expression for $S_{31,e}(\lambda)^{trap}$ is very good, the data are within 10% of the theoretical predictions. It should be noted that although $S_{31,e}(\lambda)$ depends on σ, this splitting is not attributable to E_ϕ ($E_\phi = 0$ for this calculation), it is due to the toroidal geometry and the choice of launching particle from surfaces of constant ψ, rather than $\overline{\psi}$.

When the circulating particle data are compared to the ideal banana theory, there is good agreement for the well circulating particles, but in the boundary layer, the data are consistently lower than the prediction. This can be readily explained in terms of what we have seen in the previous section concerning particle kinematics in the boundary layer. By analogy with the explicit pinch coefficient, $S_{31,e}(\lambda)$ can be viewed as the product of ω_b^{-1} and some function, κ, which corresponds to $\frac{\Delta\psi}{\Delta r}$. While it is not possible to directly examine the behavior of κ due to the method by which $S_{31,e}(\lambda)$ is calculated, let us assume for the moment that it is in exact agreement with what is predicted by the ideal banana theory. As noted in the previous section, ω_b is in fair agreement with the theoretical prediction except near the boundary. At the boundary, ω_b does not go to zero, but takes on a finite value. Thus the product of ω_b^{-1} and κ should be smaller than predicted. At the boundary, κ must tend toward zero, given that ω_b is predicted to be zero, and $S_{31,e}(\lambda)$ is finite. From the data, we see that ω_b is not zero, yet $S_{31,e}(\lambda)$ has a finite value on the boundary. This implies, that κ, if it could be computed, would also not be zero at the boundary. In short, the situation is very similar to that given in the previous section, where neither ω_b nor $\frac{\Delta\psi}{\Delta r}$ behaved as predicted near the boundary.

As in the previous section, $S_{31,e}(\lambda)$ can be integrated to find the explicit transport coefficient T_{31}. Using the same trapezoidal rule integration scheme, the circulating particle contribution to the explicit current is about 12% that of the trapped particles, with over 95% of the circulating contribution coming from the boundary layer particles. This is consistent with the theoretical calculation done in section 3.2. As we have shown that the agreement of the trapped particle banana current is within 10% of the predicted values from the ideal theory, and in Chapter 3, that the explicit current coefficient is smaller than either the circulating or trapped pinch coefficient by a factor of ϵ, but is the same size as the net pinch coefficient, we have verified the predictions of the behavior of the conjugate explicit processes made in Chapter 3. The major difference between the predictions and the data is in the response of the boundary layer; the contribution of the boundary layer particles to both T_{31} and T_{13} is much less than predicted. This result is not especially important for the explicit current coefficient, as the circulating particle contribution is small compared to the trapped particles, but it does make a major difference for the explicit pinch coefficient, as the cancellation of the trapped particle coefficient by the boundary layer contribution is not as large as predicted.

The transport coefficient can be evaluated in the presence of collisions. This was done for the $\nu_* = 8.0 \times 10^{-4}$ case discussed in the previous section. The problem is complicated by the fact that that $S_{31,e}(\lambda)$ is computed numerically and already has been weighted by ω_2^{-1}, the inverse of the actual poloidal period. To compare with the finite ν_* theory, it should have the ω_b^{-1} weighting. So the computed value of $S_{31,e}(\lambda)$ is multiplied by ω_2, to obtain the poloidal average of κ, then the statistical average of the quantity is done, before dividing by ω_b and integrating. It is found that the trapped particle banana current is unaffected by the low level scattering within the estimated statistical error. Also, the circulating particle explicit current has increased to almost 19% of the trapped particle current, with the boundary layer particles accounting for 94% of the total circulating current. Figure 5.14 shows the $\nu_* = 0$ and the $\nu_* = 8.0 \times 10^{-4}$ cases; as before the solid line denotes the prediction of the ideal banana theory ($\nu_* = 0$). Note that in some some cases the collisional value of $S_{31,e}(\lambda)$ is twice the ideal value, although it is still less than the predicted value.

The explanation of the enhancement of the boundary layer explicit current lies in the effect of the model collision operator on the boundary layer particle orbits. Examination of equation 5.2.1 reveals that there are three factors which contribute to $S_{31,e}(\lambda)$; the density, the toroidal velocity, and $(\bar{\psi} - \psi)$. The boundary layer particles will tend to become well circulating particles under the influence of the scattering operator, i.e. $\Delta\mu < 0$. This means that $|v_\phi|$ will increase. The actual change in the average density that the particle sees will be small, so the effect of the density gradient can be neglected. Given that the particle starts out with, say $\sigma = +1$, the particle may complete its poloidal orbit with either value of σ. Suppose that the particle scatters towards

well circulating space, keeping $\sigma = +1$. Thus v_ϕ will be larger than in the non-collisional case. However, $(\overline{\psi} - \psi)$ will also change. The particle starts out with $\psi > \overline{\psi}$, and as the particle moves to the outside of the torus ψ becomes less than $\overline{\psi}$. As it moves to the outside, $|v_\phi|$ will be come larger, so the outside of the torus is where most of the contribution to $S_{31,e}(\lambda)$ is made. With the scattering, the point at which ψ becomes less than $\overline{\psi}$ moves towards the outside. This effect tends to offset the increase in $|v_\phi|$, so the actual single particle value of $S_{31,e}(\lambda)$ can increase or decrease. Suppose that the particle now becomes backward directed as it scatters. Again the magnitude of the toroidal velocity increases, but it has become negative. $(\overline{\psi} - \psi)$ is initially negative as before. However, the backward directed particle will move *away* (i.e. outward) from the $\overline{\psi}$ surface. Thus $(\overline{\psi} - \psi)$ will remain negative, and given the negative v_ϕ, this leads to an unambiguous increase in $S_{31,e}(\lambda)$. Similarly, for the $\sigma = -1$ particles, if they remain backward directed, the value of $S_{31,e}(\lambda)$ can increase or decrease. If they become forward directed, v_ϕ becomes positive, and $(\overline{\psi} - \psi)$ which is initially positive, remains positive as the particle moves inward, away from the $\overline{\psi}$ surface.

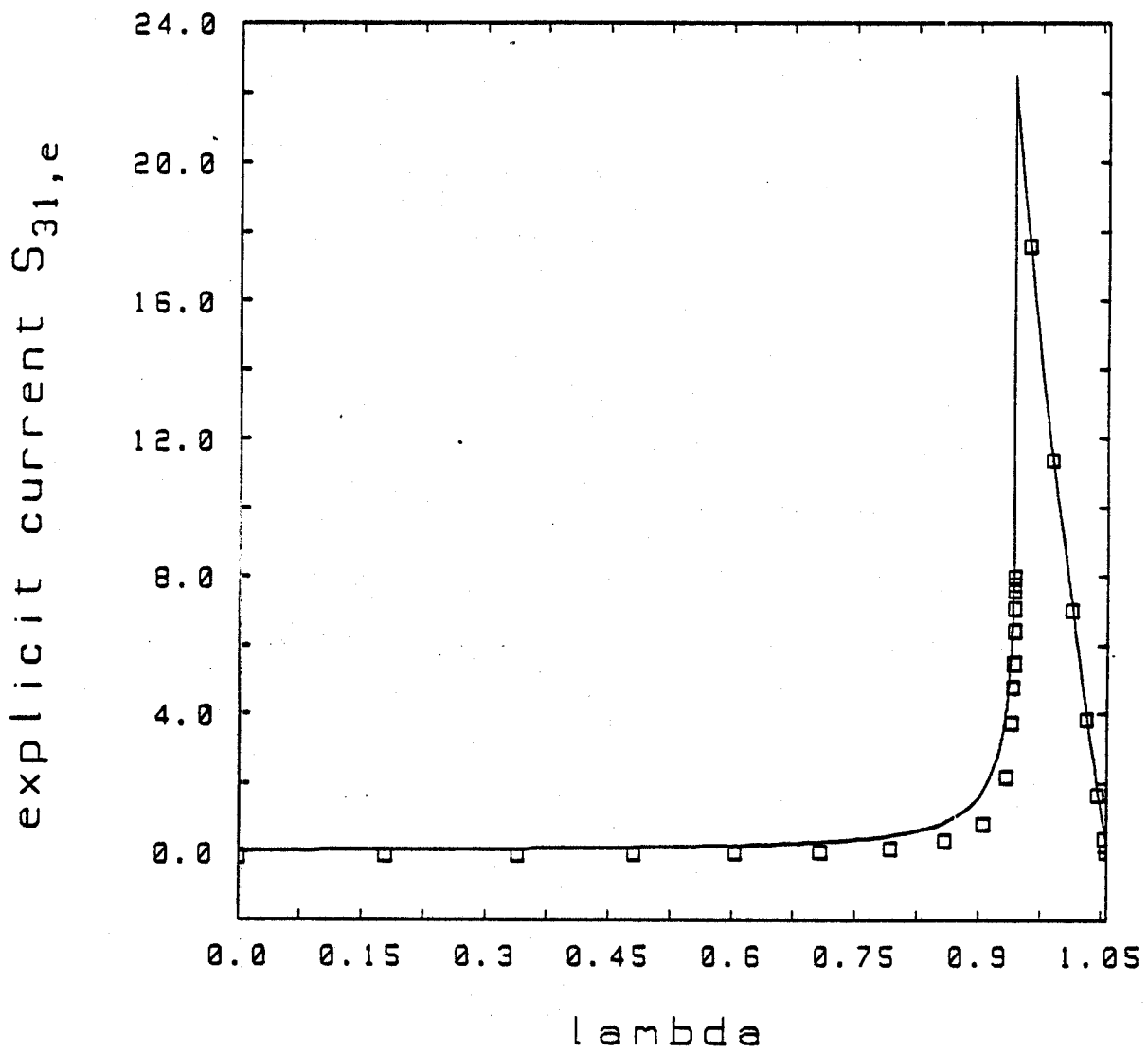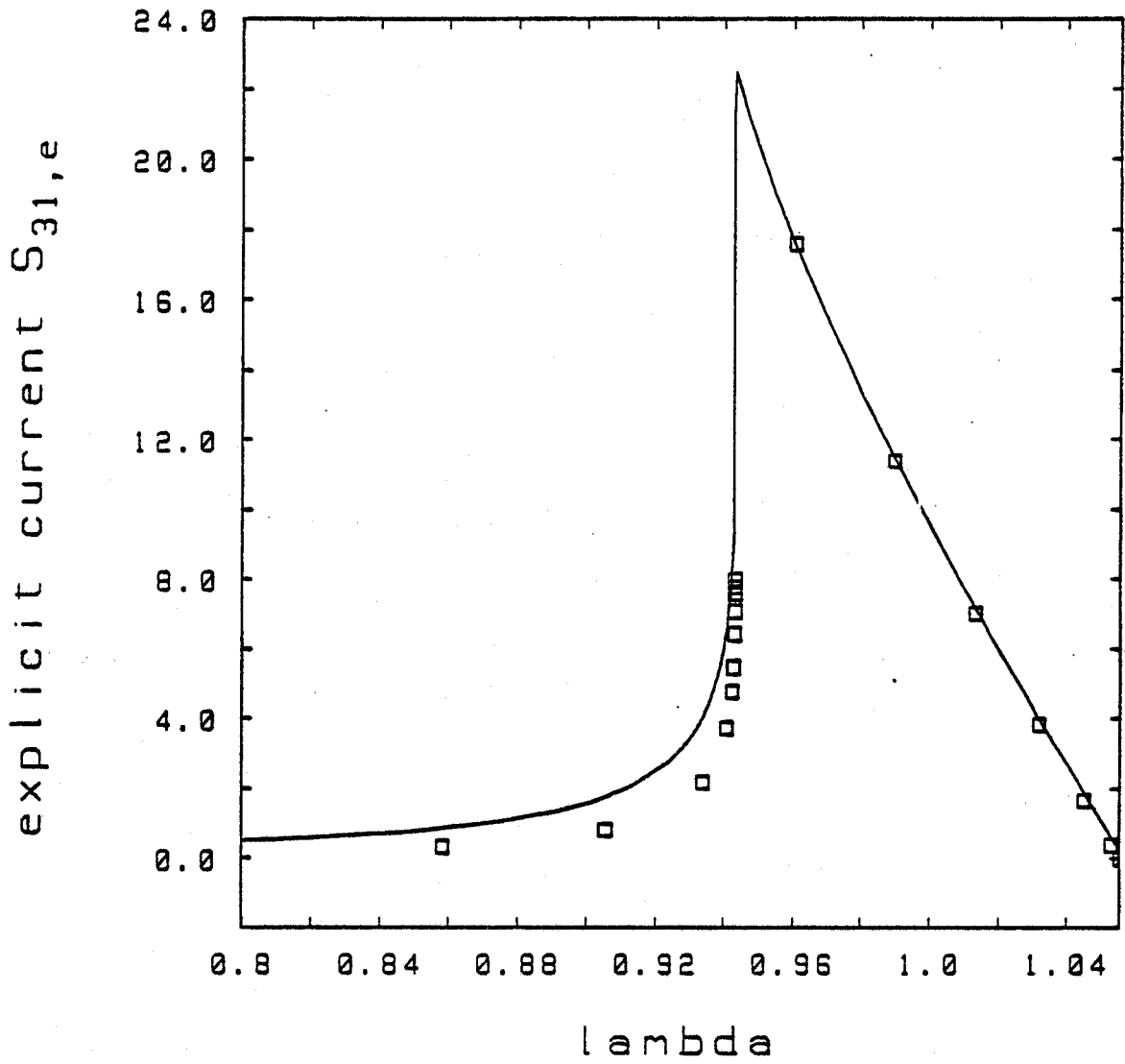Figure 5.12: $S_{31,e}(\lambda)$ vs. λ

Figure 5.13: $S_{31,e}(\lambda)$ vs. λ
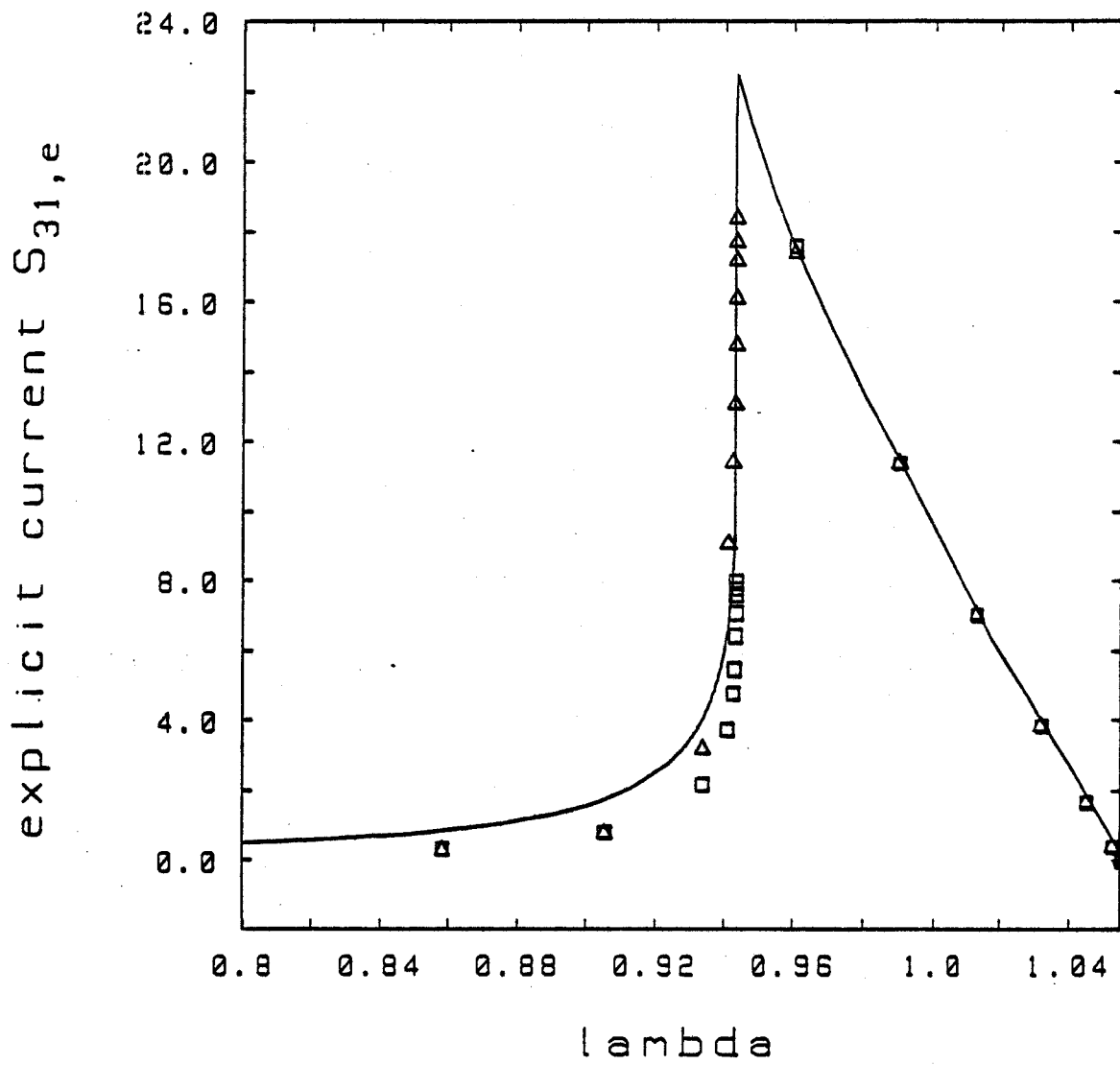region near boundary

Figure 5.14: $S_{31,e}(\lambda)$ vs. λ

region near boundary

squares denote $\nu_* = 0$, triangles denote $\nu_* = 8.0 \times 10^{-4}$

5.3. The Implicit Processes

In this section, we will examine the behavior of the Fokker–Planck coefficient $\langle \frac{\Delta\mu\Delta\psi}{\Delta r} \rangle$ as a function of the collisionality, ν_*. $\langle \frac{\Delta\mu\Delta\psi}{\Delta r} \rangle$ is easily computed given the method of computing $\frac{\Delta\psi}{\Delta r}$ presented in Chapter 4. The final value of μ is obtained from the numerical integration of the particle orbit. The initial value is known, so $\Delta\mu$ is easily computed and multiplied by $\frac{\Delta\psi}{\Delta r}$ to give $\frac{\Delta\mu\Delta\psi}{\Delta r}$. This process is repeated for many particles at each location on the phase space grid, then the results are averaged using the method described in Section 2.6 to give $\langle \frac{\Delta\mu\Delta\psi}{\Delta r} \rangle$.

The finite collisionality theory predicts that when the value of $\langle \frac{\Delta\mu\Delta\psi}{\Delta r} \rangle$ is divided by ν_*, the resultant *normalized* $\langle \frac{\Delta\mu\Delta\psi}{\Delta r} \rangle$ should decrease as ν_* increases. This result is illustrated in Figure 5.15, where the normalized $\langle \frac{\Delta\mu\Delta\psi}{\Delta r} \rangle$ is plotted as a function of the pitch parameter λ. The solid line represents the normalized prediction of the ideal theory from Section 3.3. As ν_* is increased, the peaking of the normalized $\langle \frac{\Delta\mu\Delta\psi}{\Delta r} \rangle$ in the boundary layer should become less prominent, as scattering disrupts the cross processes. The small (normalized) trapped particle contribution is unaffected by increasing ν_*. This can be seen in Figure 5.16, in which the $\nu_* = 2.0 \times 10^{-7}$ and $\nu_* = 8.0 \times 10^{-4}$ cases are plotted as functions of λ in boundary region. Table 5.3 contains a list of the normalized values of $\langle \frac{\Delta\mu\Delta\psi}{\Delta r} \rangle$ as a function of ν_* for the boundary layer particles.

Table 5.3	
normalized $\langle \frac{\Delta\mu\Delta\psi}{\Delta r} \rangle$ at boundary	
ν_*	$\langle \frac{\Delta\mu\Delta\psi}{\Delta r} \rangle$
2.0×10^{-7}	-175.0 ± 9.94
4.0×10^{-7}	-140.0 ± 8.59
2.0×10^{-6}	-113.0 ± 6.31
4.0×10^{-6}	-106.0 ± 5.72
2.0×10^{-5}	-72.7 ± 4.16
4.0×10^{-5}	-73.1 ± 3.62
2.0×10^{-4}	-51.8 ± 2.35
4.0×10^{-4}	-37.9 ± 1.93
8.0×10^{-4}	-25.8 ± 1.34

Note that the value of $\langle \frac{\Delta\mu\Delta\psi}{\Delta r} \rangle$ given in the table does not necessarily coincide with the maximum value from the figures. Also note that only the data from the forward directed particles is plotted; the $\sigma = -1$ data has the opposite sign, as will be explained below.

Many of the features of the $\langle \frac{\Delta\mu\Delta\psi}{\Delta r} \rangle$ data can be explained by examining the particle orbits. Consider the forward directed particles. Let us examine the behavior of $\langle \frac{\Delta\mu\Delta\psi}{\Delta r} \rangle$ for different values of λ. In the boundary layer, the initial value of μ will be nearly equal to its maximum allowed value of $|B|H$. Thus the scattering can only produce $\Delta\mu < 0$, but the particle can either remain

forward directed, or become backward directed. Recall that the circulating particles are launched from the inside of the torus, where the $\sigma = +1$ particles will have see the minimum value of ψ along the drift surface (the $\sigma = -1$ particles see the maximum value of ψ). Of all the circulating particles, those near the boundary will drift farthest away from the initial flux surface by the time they get to the outside of the torus, i.e. $\overline{\psi}$ is largest / smallest for the forward / backward directed boundary layer particles. Suppose the $\sigma = +1$ particle scatters, keeping $\sigma = +1$. As μ will be smaller, λ will decrease and the particle move towards well circulating space. This will happen at some value of ψ greater than the initial flux position. Because the well circulating particles tend to stay closer to their initial flux surfaces, the particle tends to remain near the value of ψ where the scattering event took place. When the poloidal orbit is completed, the result of the scattering event is an increase in the value of ψ at the initial point, $\theta = \pi$. Looking at it another way, if we were to find the initial value of ψ such that the particle were to arrive at the location where the scattering event takes place with the new value of μ, this flux value would be greater than the actual ψ from which the particles are launched. If the scattering event results in $\sigma = -1$, the result is pretty much the same. Because the backward directed orbits have a minimum in ψ at $\theta = 0$, the equivalent initial ψ of the new orbit will have to be greater than the initial flux value. The net result is that $\langle \frac{\Delta\mu\Delta\psi}{\Delta r} \rangle < 0$

Consider the well circulating particles; $\Delta\mu$ can be either positive or negative, and because these particles stay closer to their initial flux surfaces, $\Delta\psi$ will be smaller in magnitude. Thus the well circulating particles make little contribution to $\langle \frac{\Delta\mu\Delta\psi}{\Delta r} \rangle$. Using the arguments presented above, it is expected that $\langle \frac{\Delta\mu\Delta\psi}{\Delta r} \rangle < 0$ independent of the sign of $\Delta\mu$.

The trapped particles must also be considered. As with the well circulating particles $\Delta\mu$ can be either positive or negative. If $\Delta\mu > 0$, then the particle has become more deeply trapped. If we look at the initial value of ψ such that a the particle orbit with the new value of μ passes through the site of the scattering event, we see that $\Delta\psi < 0$. If $\Delta\mu < 0$, the banana orbit becomes wider. As before, if we look for the equivalent starting ψ value, we see that it is greater than the actual ψ used. The result for both cases is the same, $\langle \frac{\Delta\mu\Delta\psi}{\Delta r} \rangle < 0$.

Now consider the backward directed particles. In the boundary layer, as explained above, $\Delta\mu < 0$. When a scattering event takes place, the particle λ will decrease. Because ψ is maximal at $\theta = \pi$ for the backward directed particles, the equivalent starting ψ for the new orbit is smaller than the actual flux value. As in the $\sigma = +1$ case, this result is independent of the new value of σ. The net result is $\langle \frac{\Delta\mu\Delta\psi}{\Delta r} \rangle > 0$. This is the origin of the correlation of the particle σ and the jump in ψ alluded to in Chapter 3.

As above, $\langle \frac{\Delta\mu\Delta\psi}{\Delta r} \rangle$ is small for the well circulating particles, but it is positive. The same argument used above can be applied to the $\sigma = 1$ trapped particles; except that the particles are launched from the "inside" of the banana, and this will result in $\langle \frac{\Delta\mu\Delta\psi}{\Delta r} \rangle > 0$.

The prediction made for the behavior of the Fokker–Planck coefficient $D_{13}(\lambda)^{circ}$ in Section 3.3 is singular at the boundary, while $D_{13}(\lambda)^{trap}$ is zero everywhere. It was found that $D_{13}(\lambda)^{trap}$ is not zero, although small. This can be explained by the use of ψ instead of $\overline{\psi}$ in $\langle \frac{\Delta\mu\Delta\psi}{\Delta r} \rangle$. As explained above, it should be expected that the trapped particles make some small contribution to $\langle \frac{\Delta\mu\Delta\psi}{\Delta r} \rangle$ because of the nonzero $\Delta\psi$. Examination of the trapped particle orbits shows that $\Delta\overline{\psi} \sim 0$. $D_{13}(\lambda)$ is computed from $\Delta\overline{\psi}$, so this explains the discrepancy between theory and numerical simulation.

There are two causes for the divergence of the circulating particle $\langle \frac{\Delta\mu\Delta\psi}{\Delta r} \rangle$ from the predicted behavior of $D_{13}(\lambda)^{circ}$. First, as noted in Section 5.1, the boundary layer particles do not behave as predicted by the theory due to many factors, e.g. non-circular flux surfaces, small but non-zero drift motions. Secondly, $D_{13}(\lambda)$ is calculated in the limit of $\nu_* \to 0$. Numerically, we require a finite value of ν_* to compute $\langle \frac{\Delta\mu\Delta\psi}{\Delta r} \rangle$. As we see in Figure 5.16 and Table 5.3, as ν_* is increased, the normalized $D_{13}(\lambda)$ decreases rapidly. $D_{13}(\lambda)$ is proportional to ν_*, so the normalized $D_{13}(\lambda)$ should be constant. The normalized $\langle \frac{\Delta\mu\Delta\psi}{\Delta r} \rangle$ values decrease with increasing ν, which implies that the cross processes are being disrupted, as predicted by the finite collisionality theory. Because $\langle \frac{\Delta\mu\Delta\psi}{\Delta r} \rangle$ can not be computed in the limit $\nu_* \to 0$, any comparison between a computed $\langle \frac{\Delta\mu\Delta\psi}{\Delta r} \rangle$ and the predicted $D_{13}(\lambda)$ should not be expected to produce quantitative agreement.
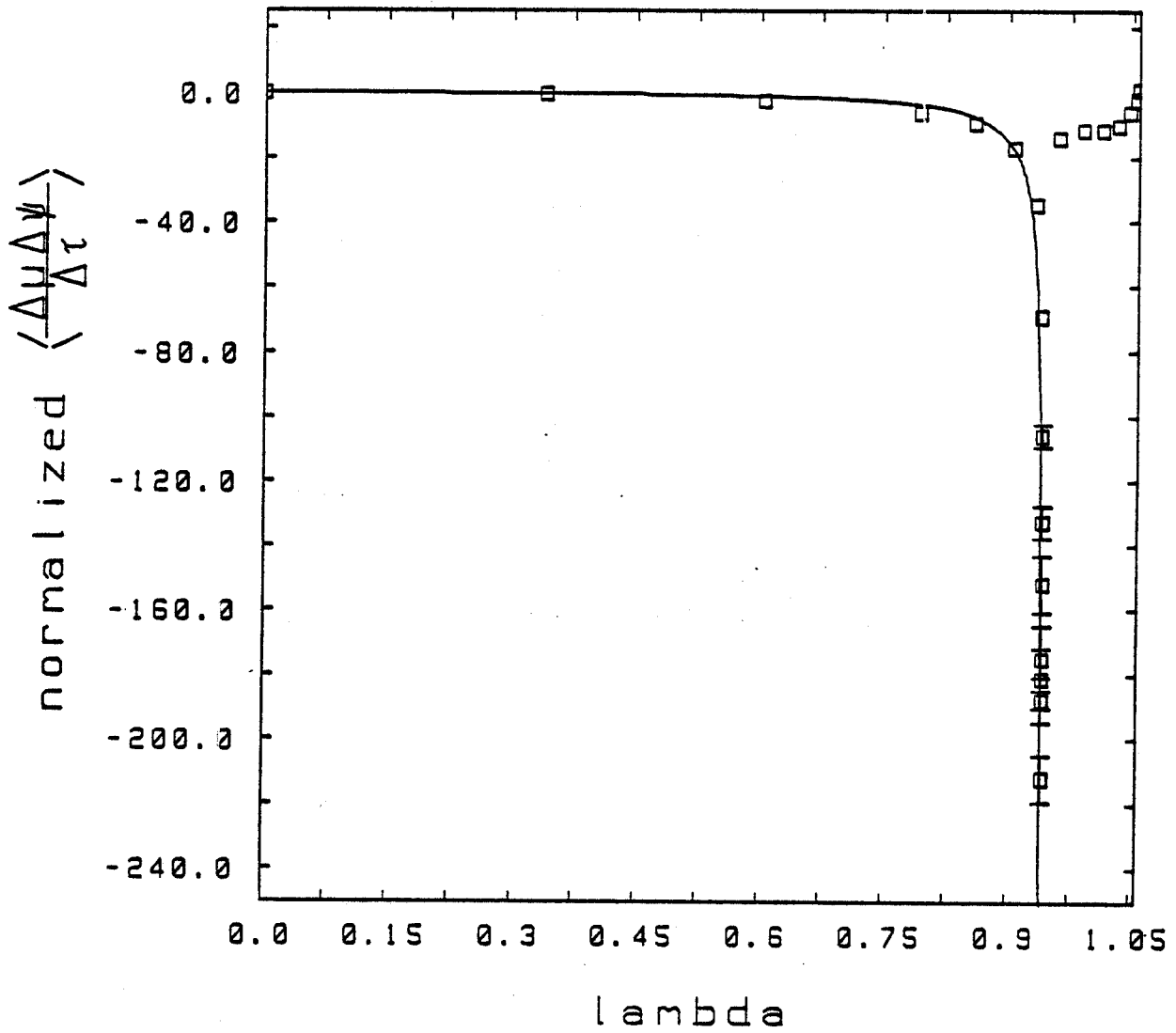
Figure 5.15: $\langle \frac{\Delta\mu\Delta\psi}{\Delta\tau} \rangle$ vs. λ
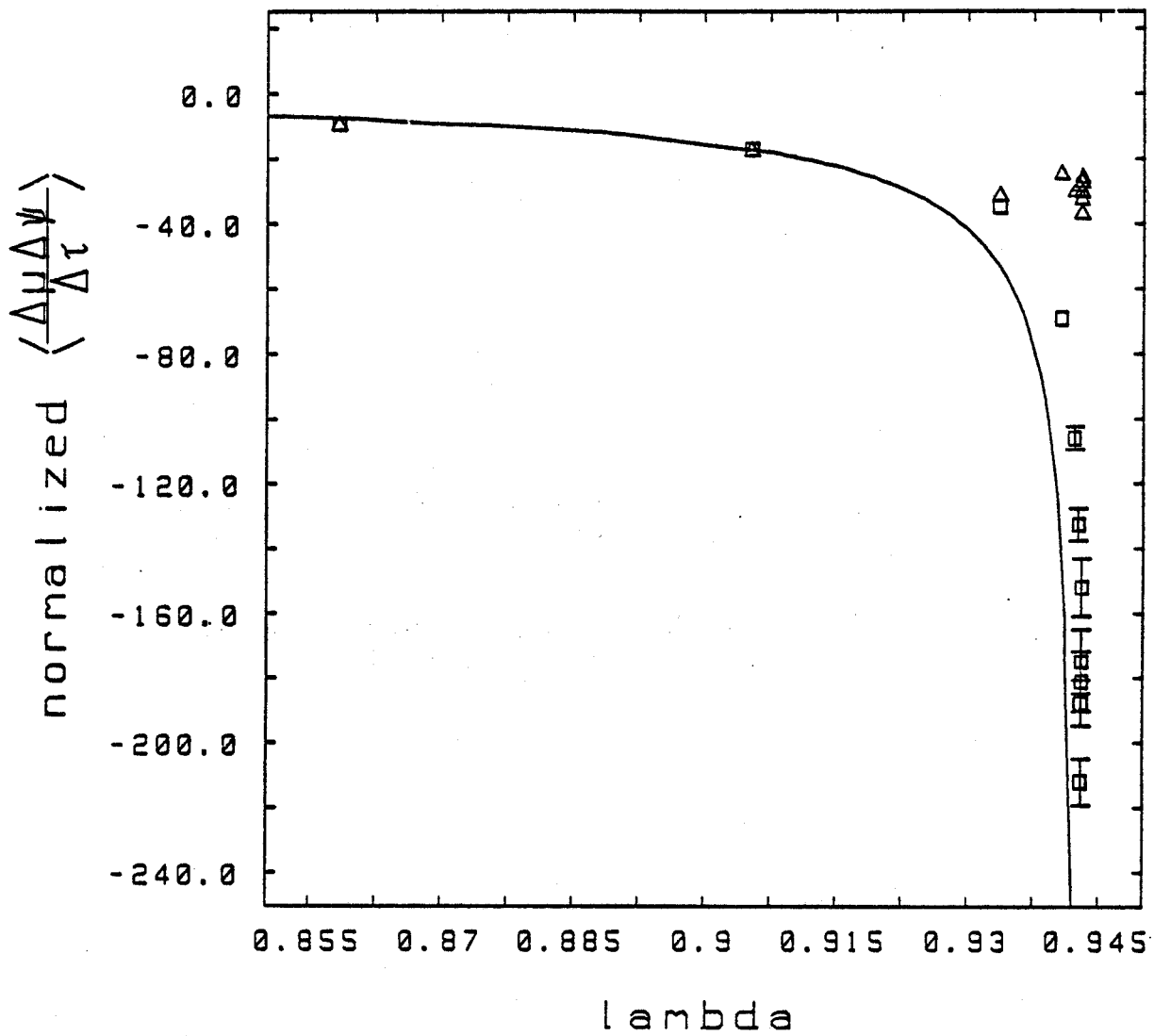
$\nu_* = 2.0 \times 10^{-7}$

Figure 5.16: $\langle \frac{\Delta\mu\Delta\psi}{\Delta\tau} \rangle$ vs. λ

region near boundary

squares denote $\nu_* = 2.0 \times 10^{-7}$, triangles denote $\nu_* = 8.0 \times 10^{-4}$

Summary and Conclusions

In this thesis, we have studied the conjugate processes of the pinch effect and the bootstrap current. The predictions made by the Lagrangian formulation of neoclassical transport theory have been compared to the results obtained by numerical integration of particle orbits for both the explicit and implicit processes. Here we present a summary of our results.

In the investigation of the explicit pinch, we have focused on the areas of particle dynamics, the non-collisional transport coefficient and the effects of collisionality on the transport coefficient. On the whole, it was found that the numerical results are in good agreement with the predictions of the ideal theory for such quantities as $\frac{\Delta \psi}{\Delta \tau}$ and ω_b. However, in the narrow region of λ space near the trapped–circulating boundary, the numerical results diverge from the predictions. This result is a consequence of the assumptions made in the Lagrangian formulation concerning the dynamics of the boundary layer particles. We have also shown that the toroidal electric field produces a "splitting" of the values of $\frac{\Delta \psi}{\Delta \tau}$ obtained for the $\sigma = \pm 1$ particles in the boundary layer. This splitting is caused by the drift in λ which is the result of the acceleration or deceleration of the particle under the action of E_ϕ.

When the $\frac{\Delta \psi}{\Delta \tau}$ and ω_b calculated from the numerical simulation are combined, we can integrate over the pitch parameter λ to obtain the explicit pinch transport coefficient. If the numerical result is normalized to the trapped particle pinch coefficient predicted by the theory (our results for $\frac{\Delta r}{\Delta \tau}$ agree with Ware's expression to within 8%), it was found that the circulating particles cancel 62% of the trapped particle contribution. The ideal theory predicts a cancellation of 94%. Further examination of the numerical results and theoretical predictions yields the result that the difference between calculation and theory is due almost entirely to the boundary layer particles.

In both the ideal theory and the finite ν_* theory, the assumption is made in the time weighting of the particle orbits that the drift motion can be neglected in comparison to the parallel motion of the particle. This assumption breaks down in the boundary layer, where the small but finite drift motions give the particles a well defined circulating motion. In addition, the limit that $E_\phi \to 0$ is

taken in both the ideal and finite ν_* theories. In the numerical simulation, finite value of E_ϕ must be used, which give rise to a drift in λ. This has the effect of reducing $\frac{\Delta \psi}{\Delta r}$ in the boundary region. It was found that the electric field used in the numerical computations gives rise to a drift in λ of about 3.0×10^{-3}. The assumption that the drift motion is negligible compared to the parallel velocity breaks down within $\Delta \lambda \sim 1.0 \times 10^{-3}$ of the boundary layer. The difference between the predicted contribution of the particles within $\Delta \lambda = 1.0 \times 10^{-3}$ of the boundary and the numerical results for the particles in this region is 45%, which accounts, to first order, for the entire difference between the predictions of the ideal banana theory and the numerical results.

The calculation of the pinch coefficient was repeated for several values of collision frequency. The trapped particle pinch coefficient was unchanged by the effect of these low levels of collisionality, as predicted by the finite ν_* theory. However, the boundary layer contribution to the circulating particle pinch coefficient was markedly reduced. This result was compared to the behavior of the circulating pinch coefficient, as a function of ν_*, predicted by the finite collisionality theory. The numerical results show the predicted qualitative behavior, but the quantitative agreement is poor. This is another consequence of the assumption that the parallel velocity dominates the circulating particle dynamics. Because of the drift motions, the boundary layer particles are more "robust", i.e. they are not as susceptible to the effects of scattering as predicted by the finite ν_* theory. This leads to a higher value of the circulating pinch transport coefficient than predicted by the finite ν_* theory.

In the area of the explicit currents, there was good agreement between the ideal banana theory and the results of the numerical simulation. In the non-collisional case, the trapped particle explicit current is in extremely good agreement with the theoretical prediction. The circulating particle current is also in good agreement, except in the boundary layer, where the numerical results are much smaller than predicted. This is another consequence of the "realistic" effects alluded to above. The addition of collisions again has no effect on the trapped particle current. Collisional effects actually increase the current from the boundary layer particles, but the net result is still less than the current predicted by the ideal banana theory for the non-collisional case.

We are not able to directly compare the explicit pinch and explicit bootstrap transport coefficients. This is because we have chosen to compute both transport coefficients for particles launched at a single energy value – this was done to reduce the amount of computer time required. As shown in Chapter 3, the energy dependence of the explicit pinch transport integral is different from the explicit bootstrap integral, which precludes direct comparison of the single energy results. Instead, we have normalized our results to the trapped particle contribution of the explicit pinch or explicit bootstrap for purposes of comparison to the Lagrangian formulation. This allows for an indirect comparison of the pinch and bootstrap explicit transport coefficients.

Our study of the implicit pinch and bootstrap processes has been restricted to examination

of the Fokker–Planck coefficient $\langle \frac{\Delta\mu\Delta\psi}{\Delta r} \rangle$. The implicit transport coefficients were not computed, which significantly reduced the amount of computer time needed. We can qualitatively discuss the implicit transport coefficients because $\langle \frac{\Delta\mu\Delta\psi}{\Delta r} \rangle$ normalized by ν_* is analogous to $\frac{\Delta\psi}{\Delta r}$ in the explicit pinch calculation.

We have shown that the $\langle \frac{\Delta\mu\Delta\psi}{\Delta r} \rangle$ derived from the numerical simulation, at a very low value of ν_*, is in good agreement with the expression given by the ideal banana theory, except near the trapped–circulating boundary. Here two effects prevent closer agreement between our results and the ideal theory. First, there are the "realistic" effects which enter into the problem through the dependence of the theoretical expressions on ω_b. The second problem is that we have had to use a finite collision frequency to obtain the normalized $\langle \frac{\Delta\mu\Delta\psi}{\Delta r} \rangle$. We find that the large peak near the boundary becomes less pronounced as ν_* is increased. Even a very small value of ν_* will have some effect on the boundary layer particles which will preclude good agreement with the predictions of the ideal banana theory.

The decrease in the boundary layer contribution of the normalized $\langle \frac{\Delta\mu\Delta\psi}{\Delta r} \rangle$ has important ramifications. In the ideal theory, the circulating particle explicit pinch nearly cancels the trapped particle explicit pinch, leaving a net explicit pinch coefficient of $O(\epsilon^{\frac{3}{2}})$. This is Onsager symmetric to the explicit current, which is of $O(\epsilon^{\frac{3}{2}})$. Thus in a "collisionless" plasma, the transport is dominated by the implicit processes. The implicit processes arise from the correlation of the scattering "cross-processes", such as $\langle \frac{\Delta\mu\Delta\psi}{\Delta r} \rangle$, with the direction of the particle velocity. We have shown how this correlation comes about, based on the effect of scattering on the particle orbits. The implicit processes are dominated by the contribution of the boundary layer particles. As ν_* increases, this boundary layer contribution becomes much smaller, and transport becomes dominated by the explicit processes. However, the increasing scattering level will also disrupt the boundary layer contribution to the explicit pinch coefficient, leaving the trapped particle contribution intact. The net result is a breaking of the Onsager symmetry; the implicit processes have been destroyed by the low level scattering, the explicit current remains of $O(\epsilon^{\frac{3}{2}})$, but the explicit pinch becomes dominated by the trapped particle contribution of $O(\epsilon^{\frac{1}{2}})$.

We have been able to show that the implicit processes are dominated by the boundary layer particles. We have seen that various effects not included in the ideal banana theory , e.g. finite E_ϕ and the drift motions of the boundary layer particles, lead to symmetry breaking for the explicit coefficients for the $\nu_* = 0$ case. Increasing ν_* does indeed disrupt the implicit processes and the circulating particle contribution to the explicit pinch as predicted by the finite collisionality theory. This is the mechanism by which the Lagrangian formulation explains the presence of the pinch effect and the absence of the bootstrap current. Qualitatively, we have been able to verify the predictions of the Lagrangian formulation for the Lorentz model.

Summary and Conclusions

In this thesis, we have studied the conjugate processes of the pinch effect and the bootstrap current. The predictions made by the Lagrangian formulation of neoclassical transport theory have been compared to the results obtained by numerical integration of particle orbits for both the explicit and implicit processes. Here we present a summary of our results.

In the investigation of the explicit pinch, we have focused on the areas of particle dynamics, the non-collisional transport coefficient and the effects of collisionality on the transport coefficient. On the whole, it was found that the numerical results are in good agreement with the predictions of the ideal theory for such quantities as $\frac{\Delta \psi}{\Delta \tau}$ and ω_b. However, in the narrow region of λ space near the trapped–circulating boundary, the numerical results diverge from the predictions. This result is a consequence of the assumptions made in the Lagrangian formulation concerning the dynamics of the boundary layer particles. We have also shown that the toroidal electric field produces a "splitting" of the values of $\frac{\Delta \psi}{\Delta \tau}$ obtained for the $\sigma = \pm 1$ particles in the boundary layer. This splitting is caused by the drift in λ which is the result of the acceleration or deceleration of the particle under the action of E_ϕ.

When the $\frac{\Delta \psi}{\Delta \tau}$ and ω_b calculated from the numerical simulation are combined, we can integrate over the pitch parameter λ to obtain the explicit pinch transport coefficient. If the numerical result is normalized to the trapped particle pinch coefficient predicted by the theory (our results for $\frac{\Delta \tau}{\Delta \tau}$ agree with Ware's expression to within 8%), it was found that the circulating particles cancel 62% of the trapped particle contribution. The ideal theory predicts a cancellation of 94%. Further examination of the numerical results and theoretical predictions yields the result that the difference between calculation and theory is due almost entirely to the boundary layer particles.

In both the ideal theory and the finite ν_* theory, the assumption is made in the time weighting of the particle orbits that the drift motion can be neglected in comparison to the parallel motion of the particle. This assumption breaks down in the boundary layer, where the small but finite drift motions give the particles a well defined circulating motion. In addition, the limit that $E_\phi \to 0$ is

taken in both the ideal and finite ν_* theories. In the numerical simulation, finite value of E_ϕ must be used, which give rise to a drift in λ. This has the effect of reducing $\frac{\Delta \psi}{\Delta r}$ in the boundary region. It was found that the electric field used in the numerical computations gives rise to a drift in λ of about 3.0×10^{-3}. The assumption that the drift motion is negligible compared to the parallel velocity breaks down within $\Delta \lambda \sim 1.0 \times 10^{-3}$ of the boundary layer. The difference between the predicted contribution of the particles within $\Delta \lambda = 1.0 \times 10^{-3}$ of the boundary and the numerical results for the particles in this region is 45%, which accounts, to first order, for the entire difference between the predictions of the ideal banana theory and the numerical results.

The calculation of the pinch coefficient was repeated for several values of collision frequency. The trapped particle pinch coefficient was unchanged by the effect of these low levels of collisionality, as predicted by the finite ν_* theory. However, the boundary layer contribution to the circulating particle pinch coefficient was markedly reduced. This result was compared to the behavior of the circulating pinch coefficient, as a function of ν_*, predicted by the finite collisionality theory. The numerical results show the predicted qualitative behavior, but the quantitative agreement is poor. This is another consequence of the assumption that the parallel velocity dominates the circulating particle dynamics. Because of the drift motions, the boundary layer particles are more "robust", i.e. they are not as susceptible to the effects of scattering as predicted by the finite ν_* theory. This leads to a higher value of the circulating pinch transport coefficient than predicted by the finite ν_* theory.

In the area of the explicit currents, there was good agreement between the ideal banana theory and the results of the numerical simulation. In the non-collisional case, the trapped particle explicit current is in extremely good agreement with the theoretical prediction. The circulating particle current is also in good agreement, except in the boundary layer, where the numerical results are much smaller than predicted. This is another consequence of the "realistic" effects alluded to above. The addition of collisions again has no effect on the trapped particle current. Collisional effects actually increase the current from the boundary layer particles, but the net result is still less than the current predicted by the ideal banana theory for the non-collisional case.

We are not able to directly compare the explicit pinch and explicit bootstrap transport coefficients. This is because we have chosen to compute both transport coefficients for particles launched at a single energy value – this was done to reduce the amount of computer time required. As shown in Chapter 3, the energy dependence of the explicit pinch transport integral is different from the explicit bootstrap integral, which precludes direct comparison of the single energy results. Instead, we have normalized our results to the trapped particle contribution of the explicit pinch or explicit bootstrap for purposes of comparison to the Lagrangian formulation. This allows for an indirect comparison of the pinch and bootstrap explicit transport coefficients.

Our study of the implicit pinch and bootstrap processes has been restricted to examination

of the Fokker–Planck coefficient $\langle \frac{\Delta\mu\Delta\psi}{\Delta r} \rangle$. The implicit transport coefficients were not computed, which significantly reduced the amount of computer time needed. We can qualitatively discuss the implicit transport coefficients because $\langle \frac{\Delta\mu\Delta\psi}{\Delta r} \rangle$ normalized by ν_* is analogous to $\frac{\Delta\psi}{\Delta r}$ in the explicit pinch calculation.

We have shown that the $\langle \frac{\Delta\mu\Delta\psi}{\Delta r} \rangle$ derived from the numerical simulation, at a very low value of ν_*, is in good agreement with the expression given by the ideal banana theory, except near the trapped–circulating boundary. Here two effects prevent closer agreement between our results and the ideal theory. First, there are the "realistic" effects which enter into the problem through the dependence of the theoretical expressions on ω_b. The second problem is that we have had to use a finite collision frequency to obtain the normalized $\langle \frac{\Delta\mu\Delta\psi}{\Delta r} \rangle$. We find that the large peak near the boundary becomes less pronounced as ν_* is increased. Even a very small value of ν_* will have some effect on the boundary layer particles which will preclude good agreement with the predictions of the ideal banana theory.

The decrease in the boundary layer contribution of the normalized $\langle \frac{\Delta\mu\Delta\psi}{\Delta r} \rangle$ has important ramifications. In the ideal theory, the circulating particle explicit pinch nearly cancels the trapped particle explicit pinch, leaving a net explicit pinch coefficient of $O(\epsilon^{\frac{3}{2}})$. This is Onsager symmetric to the explicit current, which is of $O(\epsilon^{\frac{3}{2}})$. Thus in a "collisionless" plasma, the transport is dominated by the implicit processes. The implicit processes arise from the correlation of the scattering "cross-processes", such as $\langle \frac{\Delta\mu\Delta\psi}{\Delta r} \rangle$, with the direction of the particle velocity. We have shown how this correlation comes about, based on the effect of scattering on the particle orbits. The implicit processes are dominated by the contribution of the boundary layer particles. As ν_* increases, this boundary layer contribution becomes much smaller, and transport becomes dominated by the explicit processes. However, the increasing scattering level will also disrupt the boundary layer contribution to the explicit pinch coefficient, leaving the trapped particle contribution intact. The net result is a breaking of the Onsager symmetry; the implicit processes have been destroyed by the low level scattering, the explicit current remains of $O(\epsilon^{\frac{3}{2}})$, but the explicit pinch becomes dominated by the trapped particle contribution of $O(\epsilon^{\frac{1}{2}})$.

We have been able to show that the implicit processes are dominated by the boundary layer particles. We have seen that various effects not included in the ideal banana theory , e.g. finite E_ϕ and the drift motions of the boundary layer particles, lead to symmetry breaking for the explicit coefficients for the $\nu_* = 0$ case. Increasing ν_* does indeed disrupt the implicit processes and the circulating particle contribution to the explicit pinch as predicted by the finite collisionality theory. This is the mechanism by which the Lagrangian formulation explains the presence of the pinch effect and the absence of the bootstrap current. Qualitatively, we have been able to verify the predictions of the Lagrangian formulation for the Lorentz model.

Dipole Field Calculations

In this Appendix, the analytic expressions used to evaluate the vector potential, magnetic field, and the gradients of the magnetic field for a simple dipole will be derived. The advantage of using a dipole for the poloidal field is twofold: first, A, B and ∇B can be written as simple algebraic expressions; second, the resultant magnetic field is curl free.

Beginning with the Biot–Savart Law[13], we see that the only non-zero component of the current is J_ϕ, so only A_ϕ need be calculated. The calculations will be done in cylindrical coordinates to take advantage of the axisymmetry. The equation becomes:

$$A_\phi = \frac{\mu_0}{4\pi} \int \cos \phi' \frac{J_\phi}{x} r' dr' dz' d\phi' \qquad (A.1)$$

the $\cos \phi'$ term in the numerator is required to get the projection of the current at ϕ' onto the $\hat{\phi}$ direction. For J_ϕ a delta function will be used.

$$J_\phi = I\delta(r' - a)\delta(z') \qquad (A.2)$$

where I is the toroidal current and a is the major radius. The distance x between the current loop and any point is:

$$x = \sqrt{a^2 + r^2 + z^2 - 2ar \cos \phi'} \qquad (A.3)$$

where axisymmetry has been used to remove the dependence on ϕ. When equation A.2 is inserted into equation A.1 the r' and z' integrals can be done by virtue of the delta functions.

$$A_\phi = \frac{\mu_0 I}{2\pi} \int_0^\pi \frac{a \cos \phi' d\phi'}{\sqrt{a^2 + r^2 + z^2 - 2ar \cos \phi'}} \qquad (A.4)$$

where the range of the ϕ' integration has been halved because of the even behavior of the cosine.

The ϕ' integration in equation A.4 can be done using elliptic integrals. First the half angle substitution is made:

$$\phi' = \pi - 2\alpha \tag{A.5}$$

$$d\phi' = -2d\alpha \tag{A.6}$$

$$\cos\phi' = 2\sin^2\alpha - 1 \tag{A.7}$$

Now equation A.4 can be re-written as:

$$A_\phi = \frac{\mu_0 aI}{\pi} \int_0^{\frac{\pi}{2}} \frac{(2\sin^2\alpha - 1)d\alpha}{\sqrt{(a+r)^2 + z^2 - 4ar\sin^2\alpha}} \tag{A.8}$$

Let

$$m = \frac{4ar}{(a+r)^2 + z^2} \tag{A.9}$$

A_ϕ can be expressed as:

$$A_\phi = \frac{\mu_0 I}{\pi} \frac{a}{\sqrt{(a+r)^2 + z^2}} \int_0^{\frac{\pi}{2}} \frac{(2\sin^2\alpha - 1)d\alpha}{(1 - m\sin^2\alpha)^{\frac{1}{2}}} \tag{A.10}$$

The α integral can be easily expressed in terms of the complete elliptic integrals $K(m)$ and $E(m)$.

$$K(m) = \int_0^{\frac{\pi}{2}} \frac{d\alpha}{\sqrt{1 - m\sin^2\alpha}} \tag{A.11}$$

$$E(m) = \int_0^{\frac{\pi}{2}} \sqrt{1 - m\sin^2\alpha} \ d\alpha \tag{A.12}$$

If we note that:

$$\frac{1}{\sqrt{1 - m\sin^2\alpha}} - \sqrt{1 - m\sin^2\alpha} = \frac{m\sin^2\alpha}{1 - m\sin^2\alpha} \tag{A.13}$$

Equation A.10 can finally be written as:

$$A_\phi = \frac{\mu_0 I}{\pi} \frac{a}{((a+r)^2 + z^2)^{\frac{1}{2}}} \left(2\frac{K(m)}{m} - 2\frac{E(m)}{m} - K(m) \right) \tag{A.14}$$

To get the magnetic field, the curl of A_ϕ is taken.

$$B_r = -\frac{\partial A_\phi}{\partial z} \tag{A.15}$$

$$B_z = \frac{1}{r}\frac{\partial}{\partial r}(rA_\phi) \qquad (A.16)$$

The following are a few identities which will be of use in these calculations.

$$\frac{dE}{dm} = \frac{1}{2m}\big(E(m) - K(m)\big) \qquad (A.17)$$

$$\frac{dK}{dm} = \frac{1}{2m}\Big(\frac{E(m)}{1-m} - K(m)\Big) \qquad (A.18)$$

$$\frac{\partial m}{\partial z} = -\frac{zm^2}{2ar} \qquad (A.19)$$

$$\frac{\partial m}{\partial r} = \frac{m}{r}\Big(1 - \frac{m(a+r)}{2a}\Big) \qquad (A.20)$$

First, consider B_r.

$$B_r = -\frac{\mu_0 I}{\pi}\frac{a}{\sqrt{(a+r)^2+z^2}}\bigg(\frac{-z}{(a+r)^2+z^2}\Big(\frac{2}{m}K - \frac{2}{m}E - K\Big)$$
$$+ \frac{\partial m}{\partial z}\Big(\frac{2}{m}\frac{dK}{dm} - \frac{2K}{m^2} - \frac{2}{m}\frac{dE}{dm} + \frac{2E}{m^2} - \frac{dK}{dm}\Big)\bigg) \qquad (A.21)$$

Substituting for the derivatives, and simplifying the result, we have:

$$B_r = \frac{\mu_0 I a}{\pi}\frac{z}{\sqrt{(a+r)^2+z^2}}\bigg(\frac{m}{4ar}\Big(\frac{2}{m}(K-E) - K\Big)$$
$$+ \frac{m}{2ar}\Big(\frac{1}{m}\big(\frac{E}{1-m} - K\big) - \frac{2K}{m} - \frac{(E-K)}{m} + \frac{2E}{m} - \frac{E}{2(1-m)} + \frac{K}{2}\Big)\bigg) \qquad (A.22)$$

Simplifying again, B_r can be put in the following form:

$$B_r = \frac{\mu_0 I}{2\pi r}\frac{z}{\sqrt{(a+r)^2+z^2}}\Big(-K + \frac{2-m}{2(1-m)}E\Big) \qquad (A.23)$$

The B_z calculation is a bit more difficult because of the extra factor of r. However, we can re-write equation (A.16) as follows:

$$B_z = \frac{A_\phi}{r} + \frac{\partial A_\phi}{\partial r} \qquad (A.24)$$

First, compute the derivative.

$$\frac{\partial A_\phi}{\partial r} = \frac{\mu_0 I}{\pi} \frac{a}{\sqrt{(a+r)^2 + z^2}} \left(\frac{-(a+r)}{(a+r)^2 + z^2} \left(\frac{2}{m}(K - E) - K \right) \right.$$
$$\left. + \frac{\partial m}{\partial r} \left(\frac{2}{m} \frac{dK}{dm} - \frac{2K}{m^2} - \frac{2}{m} \frac{dE}{dm} + \frac{2E}{m^2} - \frac{dK}{dm} \right) \right)$$

(A.25)

$$\frac{\partial A_\phi}{\partial r} = \frac{\mu_0 I}{\pi} \frac{a}{\sqrt{(a+r)^2 + z^2}} \left(\frac{-(a+r)}{(a+r)^2 + z^2} \left(\frac{2}{m}(K - E) - K \right) \right.$$
$$\left. + \frac{\partial m}{\partial r} \left(\frac{1}{m^2} \left(\frac{E}{1-m} - K \right) - \frac{2K}{m^2} - \frac{E-K}{m^2} + \frac{2E}{m^2} - \frac{1}{2m} \left(\frac{E}{1-m} - K \right) \right) \right)$$

(A.26)

For simplicity, first we will sum up all of the terms containing E from the $\frac{\partial A_\phi}{\partial r}$ as well as the $\frac{A_\phi}{r}$ term; then we will consider the K terms. The common factor which multiplies each expression will be temporarily neglected.

E terms
$$-\frac{2}{mr} + \frac{2}{m} \frac{a+r}{(a+r)^2 + z^2} + \frac{\partial m}{\partial r} \left(\frac{1}{m^2(1-m)} - \frac{1}{m^2} + \frac{2}{m^2} - \frac{1}{2m(1-m)} \right)$$
$$-\frac{2}{mr} + \frac{2(a+r)}{4ar} + \left(\frac{1}{r} - \frac{m(a+r)}{2ar} \right) \left(\frac{1}{m(1-m)} + \frac{1}{m} - \frac{1}{2(1-m)} \right)$$
$$-\frac{1}{mr} + \frac{2-m}{2rm(1-m)} - \frac{1}{2r(1-m)} - \frac{1}{2a(1-m)} + \frac{m(a+r)}{4ar(1-m)}$$
$$-\frac{1}{2a(1-m)} + \frac{m(a+r)}{4ar(1-m)}$$

(A.27)

K terms
$$\frac{2}{mr} - \frac{1}{r} + \frac{a+r}{(a+r)^2 + z^2} - \frac{a+r}{2ar} + \frac{\partial m}{\partial r} \left(\frac{1}{2m} - \frac{2}{m^2} \right)$$
$$\frac{2}{mr} - \frac{1}{r} + \frac{m(a+r)}{4ar} - \frac{a+r}{2ar} + \left(\frac{1}{r} - \frac{m(a+r)}{2ar} \right) \left(\frac{1}{2} - \frac{2}{m} \right)$$
$$\frac{2}{mr} - \frac{1}{r} + \frac{m(a+r)}{4ar} - \frac{a+r}{2ar} - \frac{2}{mr} + \frac{1}{2r} + \frac{a+r}{ar} - \frac{m(a+r)}{4ar}$$
$$\frac{1}{2a}$$

(A.28)

Combining the K and the E terms, we can write B_z as follows:

$$B_z = \frac{\mu_0 I}{2\pi} \frac{1}{\sqrt{(a+r)^2 + z^2}} \left(K - \frac{E}{1-m} \left(1 - \frac{m}{2r}(a+r) \right) \right)$$

(A.29)

Now the gradients of $\underline{B}$ will be calculated. This will involve taking the R and z derivatives of B_r and B_z. However, using the vector potential, the amount of work can be reduced; $\frac{\partial B_z}{\partial z}$ can be expressed in terms of other quantities. Using the definition of B_r, we can write:

$$\frac{\partial B_r}{\partial r} = -\frac{\partial^2 A_\phi}{\partial r \partial z} \tag{A.30}$$

Similarly for B_z we can write:

$$\frac{\partial B_z}{\partial z} = \frac{\partial}{\partial z}\left[\frac{1}{r}\frac{\partial}{\partial r}(rA_\phi)\right] = \frac{1}{r}\frac{\partial A_\phi}{\partial z} + \frac{\partial^2 A_\phi}{\partial z \partial r} \tag{A.31}$$

The expression for B_z can be simplified to:

$$\frac{\partial B_z}{\partial z} = -\frac{B_r}{r} - \frac{\partial B_r}{\partial r} \tag{A.32}$$

This guarantees that the magnetic field is divergence free. The remaining three derivatives must be computed. As above, computational effort will be kept to a minimum by expressing the results in terms of previously calculated quantities.

First, consider $\frac{\partial B_r}{\partial z}$. There will be three terms, each from the various places where z occurs in the expression for B_r.

$$\frac{\partial B_r}{\partial z} = \frac{B_r}{z} - \frac{B_r z}{(a+r)^2 + z^2} + \frac{\mu_0 I}{2\pi r}\frac{z}{\sqrt{(a+r)^2 + z^2}}\frac{\partial m}{\partial z}\left(-\frac{dK}{dm} + \frac{2-m}{2(1-m)}\frac{dE}{dm} + \frac{E}{2(1-m)^2}\right) \tag{A.33}$$

$$\frac{\partial B_r}{\partial z} = \frac{B_r}{z} - \frac{B_r z}{(a+r)^2 + z^2} + \frac{\mu_0 I}{2\pi r}\frac{z}{\sqrt{(a+r)^2 + z^2}}\frac{\partial m}{\partial z}\left(-\frac{1}{2m}\left(\frac{E}{1-m} - K\right)\right.$$
$$\left. + \frac{2-m}{4m(1-m)}(E-K) + \frac{E}{2(1-m)^2}\right) \tag{A.34}$$

Re-arranging terms, and writing out the B_r/z term, we have the result:

$$\frac{\partial B_r}{\partial z} = -\frac{B_r z}{(a+r)^2 + z^2} + \frac{\mu_0 I}{2\pi r}\frac{1}{\sqrt{(a+r)^2 + z^2}}\left(-K + \frac{2-m}{2(1-m)}E\right)$$
$$+ \frac{\mu_0 I}{2\pi r}\frac{z}{\sqrt{(a+r)^2 + z^2}}\frac{1}{4(1-m)}\frac{\partial m}{\partial z}\left(-K + \frac{1+m}{1-m}E\right) \tag{A.35}$$

The expression for the r derivative of B_r will be very similar to the z derivative. In particular, the only change to the last term will be the substitution of $\frac{\partial m}{\partial r}$ for $\frac{\partial m}{\partial z}$. The other terms will change slightly to reflect the r differentiation. The result is:

$$\frac{\partial B_r}{\partial r} = -B_r\left(\frac{1}{r} + \frac{a+r}{(a+r)^2 + z^2}\right) + \frac{\mu_0 I}{2\pi r}\frac{z}{\sqrt{(a+r)^2 + z^2}}\frac{1}{4(1-m)}\frac{\partial m}{\partial r}\left(-K + \frac{1+m}{1-m}E\right) \tag{A.36}$$

The remaining derivative is a bit more complicated. Before beginning the actual calculation note that:

$$\frac{\partial}{\partial r}\left(\frac{1}{1-m}-\frac{m(a+r)}{2r(1-m)}\right)=\frac{\partial m}{\partial r}\frac{r-a}{2r(1-m)^2}+\frac{am}{2r^2(1-m)} \tag{A.37}$$

$$\frac{\partial B_z}{\partial r}=-\frac{B_z(a+r)}{(a+r)^2+z^2}+\frac{\mu_0 I}{2\pi}\frac{1}{\sqrt{(a+r)^2+z^2}}\left(\frac{\partial m}{\partial r}\frac{dK}{dm}-\frac{\partial m}{\partial r}\frac{dE}{dm}\frac{1}{1-m}\left(1-\frac{m}{2r}(a+r)\right)\right.$$
$$\left.-E\frac{\partial}{\partial r}\left(\frac{1}{1-m}-\frac{m(a+r)}{2r(1-m)}\right)\right) \tag{A.38}$$

This can be expressed as:

$$\frac{\partial B_z}{\partial r}=-\frac{B_z(a+r)}{(a+r)^2+z^2}+\frac{\mu_0 I}{2\pi}\frac{1}{\sqrt{(a+r)^2+z^2}}\left[\frac{\partial m}{\partial r}\left(\frac{dK}{dm}\right.\right.$$
$$\left.\left.-\frac{dE}{dm}\frac{1}{1-m}\left(1-\frac{m}{2r}(a+r)\right)-\frac{E(r-a)}{2r(1-m)^2}\right)-\frac{amE}{2r^2(1-m)}\right] \tag{A.39}$$

If we substitute in for the derivatives of the elliptic integrals, and simplify the expression, the result is:

$$\frac{\partial B_z}{\partial r}=-\frac{B_z(a+r)}{(a+r)^2+z^2}+\frac{\mu_0 I}{2\pi}\frac{1}{\sqrt{(a+r)^2+z^2}}\frac{1}{4r(1-m)}\left[\frac{\partial m}{\partial r}\left(K(r-a)\right.\right.$$
$$\left.\left.+E\left(a+r-\frac{2(r-a)}{1-m}\right)\right)-E\frac{2am}{r}\right] \tag{A.40}$$

In practice, the quantity $\frac{\partial B_z}{\partial r}$ is not needed. Because the curl of $\underline{B}$ is identically zero everywhere except at $r=a$, $z=0$ (these expressions do not apply there anyway), it follows that

$$\frac{\partial B_z}{\partial r}=\frac{\partial B_r}{\partial z} \tag{A.41}$$

For brief discussions of the calculation of A_ϕ see references 25 and 26. The evaluation of the vector potential, magnetic field and the derivatives of $\underline{B}$ require the calculation of the complete elliptic integrals of the first and second kind. In reference 12, approximations to these functions are given in terms of polynomial and logarithmic terms in the complementary modulus. The following LISP functions illustrate the use of these approximations to compute the complete elliptic integrals. Horner's rule is used to put these expressions in an efficient form for evaluation. These two functions were used to evaluate the predictions of the ideal banana theory as expressed in Chapter

3. Equivalent FORTRAN expressions were used to compute the vector potential, magnetic field
and its gradients, from the expressions given in this Appendix.

```
(defun k-ellipt (m)
  (let ((m1 (-$ 1.0 m))
        (ak0 1.39629436112) (ak1 0.09666344259) (ak2 0.03590092383)
        (ak3 0.03742563713) (ak4 0.01451196212) (bk0 0.5)
        (bk1 0.12498593597) (bk2 0.06880248576) (bk3 0.03328355346)
        (bk4 0.00441787012))
    (-$ (+$ ak0 (*$ (+$ ak1 (*$ (+$ ak2 (*$ (+$ ak3 (*$ ak4 m1)) m1)) m1)) m1))
        (*$ (+$ bk0 (*$ (+$ bk1 (*$ (+$ bk2 (*$ (+$ bk3 (*$ bk4 m1)) m1)) m1)) m1))
            (log m1)))))


(defun e-ellipt (m)
  (let ((m1 (-$ 1.0 m))
        (ae1 0.44325141463) (ae2 0.06260601220) (ae3 0.04757383546)
        (ae4 0.01736506451) (be1 0.24998368310) (be2 0.09200180037)
        (be3 0.04069697526) (be4 0.00526449639))
    (-$ (+$ 1.0 (*$ (+$ ae1 (*$ (+$ ae2 (*$ (+$ ae3 (*$ ae4 m1)) m1)) m1)) m1))
        (*$ (log m1) (+$ be1 (*$ (+$ be2 (*$ (+$ be3 (*$ be4 m1)) m1)) m1)) m1)))))
```

Sparse Matrix Inversion Techniques

In the appendix, matrix inversion techniques for two types of sparse matrices will be discussed. The basic starting point for each type of matrix is the LU decomposition algorithm. The matrix is expressed as a product of a lower triangular matrix and an upper triangular matrix. The LU decomposition will be worked out in detail for one matrix, and the results will be given for the other one. Two applications will be presented; solving a simple matrix equation in $O(n)$ operations (n is the size of the square matrix) and computing the inverse of the matrix with a substantial reduction in the number of operations compared to a standard inversion routine, such as Gaussian elimination.

For the applications discussed in Chapter 4, each element of the $n \times n$ matrix is a scalar. This need not always be the case; each matrix element could itself be a square $m \times m$ matrix. Such systems often occur when solving coupled differential equations with finite difference methods. To preserve generality, and because the set of $m \times m$ matrices is a non-commutative ring, the algorithms will contain multiplication by the inverses of the elements, instead of division by the elements.

B.1. The Decomposition Algorithms

The two matrices that we will be considering are:

$$
A = \begin{pmatrix}
b_1 & c_1 & \alpha & & & & \\
a_2 & b_2 & c_2 & & & & \\
 & \cdot & \cdot & \cdot & & & \\
 & & \cdot & \cdot & \cdot & & \\
 & & & \cdot & \cdot & \cdot & \\
 & & & & a_{n-1} & b_{n-1} & c_{n-1} \\
 & & & & \beta & a_n & b_n
\end{pmatrix}
$$

$$B = \begin{pmatrix} b_1 & c_1 & & & & & \alpha \\ a_2 & b_2 & c_2 & & & & \\ & \cdot & \cdot & \cdot & & & \\ & & \cdot & \cdot & \cdot & & \\ & & & \cdot & \cdot & \cdot & \\ & & & & a_{n-1} & b_{n-1} & c_{n-1} \\ \beta & & & & & a_n & b_n \end{pmatrix}$$

Note that all elements not shown or implied by the dots are zero. These matrices are just tridiagonal matrices with two additional elements. If the two elements were zero, Thomas's Algorithm[27] could be used. The "extra" elements arise from the boundary conditions a spline or finite difference problem imposes. The corner elements in the second matrix come from periodic boundary conditions, while the extra elements in the first matrix come from fixing a function value (or derivative) at the boundary. While only these two tridiagonal matrices will be examined, this inversion method can be readily extended to pentadiagonal systems.[28]

The elements of the triangular matrices L and U are completely specified by the condition $LU = A$. In fact, this condition over-specifies the problem; we have the freedom to choose the values for the main diagonal of either L or U. The product LU is of the form:

$$\begin{pmatrix} m_1 & & & & & \\ l_2 & m_2 & & & & \\ & \cdot & \cdot & & & \\ & & \cdot & \cdot & & \\ & & & \cdot & \cdot & \\ & & & l_{n-1} & m_{n-1} & \\ & & & \bar{\beta} & l_n & m_n \end{pmatrix} \begin{pmatrix} 1 & u_1 & \tilde{\alpha} & & & \\ & 1 & u_2 & & & \\ & & \cdot & \cdot & & \\ & & & \cdot & \cdot & \\ & & & & \cdot & \cdot \\ & & & & 1 & u_{n-1} \\ & & & & & 1 \end{pmatrix}$$

where the main diagonal elements of U have been arbitrarily chosen to be 1 (note: following standard notation, "1" is the multiplicative identity of the ring on which these operations are performed; this is not necessarily the integer 1). If we consider the elements of A row by row, we generate the following formulae from the product LU:

row 1

$$b_1 = m_1$$
$$c_1 = m_1 u_1 \qquad\qquad (B.1.1)$$
$$\alpha = m_1 \tilde{\alpha}$$

row 2

$$l_2 = a_2$$
$$b_2 = m_2 + l_2 u_1$$
$$c_2 = m_2 u_2 + l_2 \tilde{\alpha}$$
(B.1.2)

row j: 2 < j < n

$$a_j = l_j$$
$$b_j = m_j + l_j u_{j-1}$$
$$c_j = m_j u_j$$
(B.1.3)

row n

$$\beta = \tilde{\beta}$$
$$a_n = l_n + \tilde{\beta} u_{n-2}$$
$$b_n = m_n + l_n u_{n-1}$$
(B.1.4)

if we solve these four equations for the unknown quantities which are the elements of the two triangular matrices, we have:

row 1

$$m_1 = b_1$$
$$u_1 = m_1^{-1} c_1$$
$$\tilde{\alpha} = m_1^{-1} \alpha$$
(B.1.5)

row 2

$$l_2 = a_2$$
$$m_2 = b_2 - l_2 u_1$$
$$u_2 = m_2^{-1}(c_2 - l_2 \tilde{\alpha})$$
(B.1.6)

row j: 2 < j < n

$$l_j = a_j$$
$$m_j = b_j - l_j u_{j-1}$$
$$u_j = m_j^{-1} c_j$$
(B.1.7)

row n

$$\tilde{\beta} = \beta$$
$$l_n = a_n + \tilde{\beta} u_{n-2}$$
$$m_n = m_n - l_n u_{n-1}$$
(B.1.8)

These relations allow the computation of each element of L and U in terms of the elements of A and previously computed elements of L and U. The total number of operations needed to obtain the complete LU decomposition is proportional to n, the size of the matrix.

For matrix B, the tridiagonal matrix with corner elements, the matrices L and U are of the form:

$$
\begin{pmatrix}
m_1 & & & & & & \\
a_2 & m_2 & & & & & \\
 & & \cdot & \cdot & & & \\
 & & & \cdot & \cdot & & \\
 & & \vdots & & \cdot & & \\
 & & & & & a_{n-1} & m_{n-1} \\
l_1 & l_2 & \cdot & \cdot & \cdot & l_{n-1} & m_n
\end{pmatrix}
\begin{pmatrix}
1 & u_1 & & & & & r_1 \\
 & 1 & u_2 & & & & r_2 \\
 & & \cdot & \cdot & & & \cdot \\
 & & & \cdot & \cdot & & \cdot \\
 & & & & \cdot & u_{n-2} & r_{n-2} \\
 & & & & & 1 & r_{n-1} \\
 & & & & & & 1
\end{pmatrix}
$$

where the a_j which appear in L are the same as those given in B. Solving for the unknown elements of L and U we have:

row 1

$$
\begin{aligned}
m_1 &= b_1 \\
u_1 &= m_1^{-1} c_1 \\
l_1 &= m_1^{-1} \beta \\
r_1 &= m_1^{-1} \alpha
\end{aligned}
\qquad (B.1.9)
$$

row 2

$$
\begin{aligned}
m_2 &= b_2 - a_2 u_1 \\
u_2 &= m_2^{-1} c_2 \\
l_2 &= -l_1 u_1 \\
r_2 &= -m_2^{-1} a_2 r_1
\end{aligned}
\qquad (B.1.10)
$$

row j: $2 < j < n-1$

$$
\begin{aligned}
m_j &= b_j - a_j u_{j-1} \\
u_j &= m_j^{-1} c_j \\
l_j &= -l_{j-1} u_{j-1} \\
r_j &= -m_j^{-1} a_j r_{j-1}
\end{aligned}
\qquad (B.1.11)
$$

rows $n-1$ and n

$$
\begin{aligned}
m_{n-1} &= b_{n-1} - a_{n-1} u_{n-2} \\
l_{n-1} &= a_n - l_{n-2} u_{n-2} \\
r_{n-1} &= m_{n-1}^{-1} (c_{n-1} - a_{n-1} r_{n-2}) \\
m_n &= b_n - \sum_{i=1}^{n-1} l_i u_i
\end{aligned}
\qquad (B.1.12)
$$

B.2. Solution of a Matrix Equation

One of the most common applications of matrix inversion techniques is the solution of a system of the equations which can be expressed in the form

$$
M x = d \qquad (B.2.1)
$$

where M is an $n \times n$ matrix, x is the solution vector, and d is a vector of known values. If M is of the form of matrix A or matrix B, this equation can be simply solved using the LU decomposition scheme discussed in the previous section. Substituting the product LU for M, we have:

$$LUx = d \qquad (B.2.2)$$

If we let y represent the product Ux, we have two very simple matrix equations to solve:

$$\begin{aligned} Ly &= d \\ Ux &= y \end{aligned} \qquad (B.2.3)$$

Given the matrices L and U, all that remains is to work out the relations for the vectors x and y. These are easy to establish, because in each case we are working with a triangular matrix. First, the expressions for matrix A will be derived.

for vector y:

$$\begin{aligned} y_1 &= m_1^{-1} d_1 \\ y_j &= m_j^{-1}(d_j - l_j y_{j-1}) \\ y_n &= m_n^{-1}(d_n - l_n y_{n-1} - \bar{\beta} y_{n-2}) \end{aligned} \qquad (B.2.4)$$

for vector x:

$$\begin{aligned} x_n &= y_n \\ x_j &= y_j - u_j x_{j+1} \\ x_1 &= y_1 - u_1 x_2 - \bar{\alpha} x_3 \end{aligned} \qquad (B.2.5)$$

Now, the expressions for the matrix B.

for vector y:

$$\begin{aligned} y_1 &= m_1^{-1} d_1 \\ y_j &= m_j^{-1}(d_j - a_j y_{j-1}) \\ y_n &= m_n^{-1}\left(d_n - \sum_{i=1}^{n-1} l_i y_i\right) \end{aligned} \qquad (B.2.6)$$

for vector x:

$$\begin{aligned} x_n &= y_n \\ x_{n-1} &= y_{n-1} - r_{n-1} x_n \\ x_j &= y_j - u_j x_{j+1} - r_j x_n \end{aligned} \qquad (B.2.7)$$

When implementing these equations, it is important to note that the vector y can be computed at the same time as the elements of L and U. Solving for x, which is a special case of the back-substitution algorithm common in Gaussian elimination routines, must be done in a separate loop after y has been calculated. The earlier decision to let the main diagonal of the U matrix be filled with unity is justified because it simplifies solving for x, also note that m_j and m_j^{-1} do *not* have to be saved after y_j is calculated.

This solution algorithm can be done in $O(nm^3)$ operations (m is the size of the elements, $m = 1$ for scalars) compared to $O(n^3m^3)$ operations if we were to blindly use a standard full matrix inversion routine.

B.3. Inverting a Matrix

In this section, the problem of inverting a matrix M and returning the inverse will be addressed. The method outlined here is the method used in solving the two dimensional spline interpolation problem in Chapter 4. For the one dimensional spline problem, it is possible to solve for the interpolation coefficients using the method described in the previous section.

As in the previous section, the starting point of this algorithm is the LU decomposition. algorithm. Using basic linear algebra, we have:

$$M^{-1} = (LU)^{-1} = U^{-1}L^{-1} \qquad (B.3.1)$$

The problem now is reduced to finding the inverses of L and U. There are well known[29] inversion routines for both upper and lower triangular matrices, which require $O(n^3)$ operations; however these may be modified for use on the sparse matrices L and U with substantial savings in operations.

In general, if we have some lower triangular matrix L', the inverse, L'^{-1}, will also be lower triangular (similarly, upper triangular matrices have upper triangular inverses). The recursion formula for computing the elements of the inverse are easily found by considering the equation:

$$L'Y = I \qquad (B.3.2)$$

where I is the identity matrix, and Y is L'^{-1}. To compute the elements of Y, the following algorithm is used:

for column j: first compute the diagonal element y_{jj}

$$y_{jj} = -l'_{jj}{}^{-1} \qquad (B.3.3)$$

if $j < n$: compute the other elements in the column:

$$y_{ij} = -l'_{ii}{}^{-1} \sum_{k=j}^{i-1} l'_{ik} y_{kj} \qquad (B.3.4)$$

where $i = j + 1, j + 2, \ldots, n$.

For upper triangular matrices, a similar recursion relation can be derived.

$$U'Z = I \qquad (B.3.5)$$

where I is the identity matrix, and Z is U'^{-1}.

for column j: first compute the diagonal element z_{jj}

$$z_{jj} = -u_{jj}'^{-1} \tag{B.3.6}$$

if $j > 1$: compute the other elements in the column

$$z_{ij} = -u_{ii}'^{-1} \sum_{k=i+1}^{j} u_{ik}' z_{kj} \tag{B.3.7}$$

where $i = j - 1, j - 2, \ldots, 1$.

For our purposes, neither L nor U is a full triangular matrix, so we can improve on the $O(n^3)$ operations needed to invert L' and U'. First we will consider the matrices resulting from the LU decomposition of A. To invert L:

for column j ($j = 1$ to $j = n$) compute the diagonal element y_{jj}:

$$y_{jj} = m_j^{-1} \tag{B.3.8}$$

if $j < n$, compute the off-diagonal elements y_{ij}, $i = j + 1$ to $i = n$:

if $i < n$:

$$y_{ij} = -m_i^{-1} l_i y_{i-1,j} \tag{B.3.9}$$

if $i = n$:

$$y_{nj} = -m_n^{-1}(\bar{\beta} y_{n-2,j} + l_n y_{i-1,j}) \tag{B.3.10}$$

where the appropriate quantities from the LU decomposition have been substituted in.

A count of the operations reveals that this algorithm scales as $O(n^2)$ instead of the $O(n^3)$ for the full triangular matrix. The procedure for inverting U is similar, except that we know that the diagonal elements z_{jj} will be unity.

for column j, $j = n$ to $j = 1$:

$$z_{jj} = 1 \tag{B.3.11}$$

for row i, if $i = j - 1$ to $i = 2$:

$$z_{ij} = -u_i z_{i+1,j} \tag{B.3.12}$$

if $i = 1$ and $j > 2$:

$$z_{1j} = -u_1 z_{2j} - \bar{\alpha} z_{3j} \tag{B.3.13}$$

if $i = 1$ and $j = 2$:

$$z_{1,2} = -u_1 z_{2,2} \tag{B.3.14}$$

If we now consider the matrices L and U which result from the decomposition of B, the tridiagonal matrix with corner elements, we can write down the recursion relations which describe the inverses.

for column j ($j = 1$ to $j = n$) compute the diagonal element y_{jj} as before.

$$y_{jj} = m_j^{-1} \tag{B.3.15}$$

if $j < n$, compute the off-diagonal elements y_{ij}, $i = j + 1$ to $i = n$.

    if $i < n$:

$$y_{ij} = -m_i^{-1} a_i y_{i-1,j} \tag{B.3.16}$$

    if $i = n$:

$$y_{nj} = -m_n^{-1} \sum_{k=j}^{n-1} l_k y_{kj} \tag{B.3.17}$$

for column j, $j = n$ to $j = 1$:

$$z_{jj} = 1 \tag{B.3.18}$$

for row i, $i = j - 1$ to $i = 1$:

    if $j < n$:

$$z_{ij} = -u_i z_{i+1,j} \tag{B.3.19}$$

    if $i = n - 1$ and $j = n$:

$$z_{n-1,n} = -r_{n-1} z_{n,n} \tag{B.3.20}$$

    if $i < n - 1$ and $j = n$:

$$z_{in} = -u_i z_{i+1,n} - r_i z_{nn} \tag{B.3.21}$$

Again we see that the number of operations needed to do the inversions scales as $O(n^2)$. The only remaining thing to do is to multiply the inverses together. A full matrix multiplication would take n^3 operations; because the two matrices being multiplied are upper and lower triangular respectively, the number of operations is $\frac{1}{3}n^3$. The other operations in this algorithm, computing the LU decomposition and inverting the two triangular matrices scale as $O(n)$ and $O(n^2)$ respectively, so for large n, the total number of operations is approximately $\frac{1}{3}n^3$. The number of operations need for a full matrix inversion is given in reference 29. If the LU decomposition is given, the full inversion routine will take n^3 operations; performing the decomposition itself will require $O(n^3)$ operations. Thus using this sparse matrix inversion algorithm results in a *minimum* savings in operations of $\frac{2}{3}n^3$ compared to a full matrix inversion routine.

References

1. A. A. Galeev and R. Z. Sagdeev, *Sov. Phys. JETP*, 26, 233 (1968). M. N. Rosenbluth, R. D. Hazeltine and F. L. Hinton, *Phys. Fluids*, 15, 116 (1972). F. L. Hinton and R. D. Hazeltine, *Rev. Mod. Phys.*, 48, 239 (1976)

2. R. R. Parker, K. Molvig and L. S. Scaturro, *Proceedings of Workshop on Fusion Fueling*, Princeton, N. J. (1977). K. Bol, *et al.*, *Plasma Phys. Contr. Nucl. Fusion Res.*, 1, 11 (1978). A. Gondhalekr, D. O. Overskei, R. R. Parker and J. West, *J. Magn. Magn. Mater.*, 11, 359 (1979)

3. M. H. Hughes and J. Hugill, *Plasma Phys. Contr. Nucl. Fusion Res.*, 1, 457 (1978)

4. J. T. Hogan, *Nucl. Fusion*, 21, 365 (1981)

5. D. J. Lees, Culham Laboratory Report, CLM-R-135, 1974

6. K. Molvig, L. M. Lidsky, K. Hizanidis and I. B. Bernstein, *Comments on Modern Physics: Part E*, 7, 113 (1982)

7. I. B. Bernstein and K. Molvig, *Phys. Fluids*, 26, 1488 (1983)

8. K. Hizanidis, *Lagrangian Formulation of Neoclassical Transport Theory*, Ph.D. thesis, Dept. of Nuclear Engineering, Massachusetts Institute of Technology, June 1982

9. A. A. Ware, *Phys. Rev. Lett.*, 25, 15, (1970)

10. B. Efron, G. Gong, *The American Statistician*, 37, 36, (1983)

11. P. F. Byrd and M. D. Friedman, *Handbook of Elliptic Integrals for Engineers and Scientists*, Springer-Verlag, 1971

12. C. Hastings, *Approximations for Digital Computers*, pp. 170–175 Princeton University Press, 1955

13. P. Lorrain, D. R. Corson, *Electromagnetic Fields and Waves*, 2nd edition, pp. 303–306, W. H. Freeman and Company, San Francisco, 1970

14. J. B. Taylor, *Phys. Fluids*, 6, 1529, (1963)

15. G. Bateman, *MHD Instabilities*, pp138–140, MIT Press, Cambridge, MA, 1978

16. A. H. Boozer and G. Kuo–Petravic, *Phys. Fluids*, 24, 851, (1981)

17. G. E. P. Box and M. E. Muller, *Ann. Math. Stat.*, 29, 610, (1958)

18. R. Shanny, J. M. Dawson, and J. M. Greene, *Phys. Fluids*, 10, 1281, (1967)

19. G. G. Lister, D. E. Post, and R. Goldston, in *3rd Varenna Symposium on Plasma Heating in Toroidal Devices*, p. 303, Editrice Compositori, Bologna, Italy, 1976

20. C. de Boor, *A Practical Guide to Splines*, Springer–Verlag, New York, 1978

21. R. E. Potok, *Particle Orbits and Diffusion in Torsatrons*, Sc.D. thesis, MIT Department of Nuclear Engineering, May, 1980

22. J. G. Aspinall, *Spline Techniques for Magnetic Fields*, Plasma Fusion Center Report PFC/RR-83-27, September, 1983

23. T. G. Northrop, *The Adiabatic Motion of Charged Particles*, John Wiley and Sons, New York, 1963

24. F. S. Acton, *Numerical Methods That Work*, Harper and Row, New York, 1970

25. W. R. Smythe, *Static and Dynamic Electricity*, 3rd edition, pp. 290–291, McGraw-Hill, New York, 1969

26. J. D. Jackson, *Classical Electrodynamics*, 2nd edition, pp. 177–180, John Wiley and Sons, New York, 1975

27. D.U. von Rosenberg, *Methods for the Numerical Solution of Partial Differential Equations*, Appendix B, American Elsevier Publishing, New York, (1969)

28. *First Wall Structural Response to a Major Plasma Disruption*, M. S. Tillack executive producer, directed by J. G. Aspinall, screenplay by P. B. Roemer, J. W. Johnson technical assistant, Massachusetts Institute of Technology, (MCMLXXXIII)

29. G. Dahlquist, A. Bjorck and T. Anderson, *Numerical Methods*, Section 5.3.6, Prentice–Hall, Englewood Cliffs, NJ, (1974)